TOWARDS THE DESIGN OF CAMPANIFORM SENSILLA INSPIRED STRAIN SENSORS: AN FEM-BASED STRUCTURAL ANALYSIS AND GEOMETRICAL OPTIMIZATION

by

Nickolas L.M. Mani
Bachelor of Mechanical Engineering, Noshirvani Technical University, 2004

THESIS SUBMITTED IN PARTIAL FULFILLMENT OF
THE REQUIREMENTS FOR THE DEGREE OF

MASTER OF APPLIED SCIENCE

In the
School of Engineering Science

SIMON FRASER UNIVERSITY

Fall 2010

APPROVAL

Name: **Nickolas L.M. Mani**

Degree: **Master of Applied Science**

Title of Thesis: **Towards the Design of Campaniform Sensilla Inspired Strain Sensors: an FEM-based Structural Analysis and Geometrical Optimization**

Examining Committee:

Chair: **Dr. Marinko V. Sarunic, P. Eng.**
Assistant Professor, School of Engineering Science

_____

Dr. Carlo Menon, P. Eng.
Senior Supervisor
Assistant Professor, School of Engineering Science

_____

Dr. John Jones, P. Eng.
Supervisor
Associate Professor, School of Engineering Science

_____

Dr. Ash M. Parameswaran, P. Eng.
Internal Examiner
Professor, School of Engineering Science

Date Defended/Approved: October 28 2010

Declaration of
Partial Copyright Licence

ABSTRACT

In this thesis, a structural analysis is performed to gain insights on the strain amplification characteristics of campaniform sensilla. In order to simplify the analysis, a single hole and four holes in arrays of two in orthotropic lamina are considered. Firstly, a finite element method (FEM) analysis is performed to discretely assess the influence that different geometrical parameters and material properties have on the mechanical amplification of the hole(s). Secondly, an artificial neural network is used to obtain an approximated multi-dimensional continuous function, which models the relationship between the geometrical parameters and the amplification of the hole(s). Thirdly, an optimization is performed to identify the geometrical parameters yielding the maximum mechanical amplification. Finally, results are validated with an additional FEM simulation performed by varying geometrical parameters in the neighborhood of the identified optimal parameters. The procedure based on FEM simulations proposed in this thesis is fully automated and could be used to solve a wide range of problems aimed at identifying optimal configurations of strain sensors inspired by campaniform sensilla.

Keywords: Strain sensor; Campaniform sensilla; Campaniform sensillum; Finite element method (FEM); Automated FEM (A-FEM); Artificial neural network (ANN); Optimization; Data modelling; Mode pursuing method (MPS).

DEDICATION

“Keep your dreams alive. Understand to achieve anything requires faith and belief in yourself, vision, hard work, determination, and dedication. Remember all things are possible for those who believe.” ~ Gail Devers

I dedicate this thesis to my Mom, Ruhangiz, and Dad, Naser, who have supported me, and have accommodated me with their warm and quiet house.

Thanks to my older sister, Mary Mani, who has been like a second mother to me.

Thanks to my gorgeous sister Dr. Anahita Mani and the baby girl she has recently delivered. She was my colleague at Simon Fraser University for the last year of my research.

Thanks to my older brother, Mehrdad Mani, whom I believe is a portrait of a best friend.

ACKNOWLEDGEMENTS

The author gratefully acknowledges the technical and logistic support of Dr. Anahita Mani, Bruce Leighton, Ehsan Shah-Hosseini and Mohammad Izadi. CMC Microsystems supported this work. The MPS code was provided by Dr. Garry Wang in Mechatronic Systems Engineering department of Simon Fraser University. I would like to honour Sahar Ghazi for her job on editing this thesis.

Lastly, I would like to thank Dr. Carlo Menon, senior supervisor, Dr. John Jones, supervisor, Dr. Ash M. Parameswaran, internal examiner, and Dr. Marinko V. Sarunic, the chair, of my defence committee.

TABLE OF CONTENTS

LIST OF FIGURES

LIST OF TABLES

GLOSSARY

$\boldsymbol{\varepsilon_{r_i}}$ Radial strain of the hole's radius, r_i.

$\boldsymbol{\varepsilon_R}$ Maximum radial strain among radii of a hole, in design concept 1, or four holes, in design concept 2, at each A-FEM iteration.

$\boldsymbol{\varepsilon_{Rm}}$ Maximum ε_R among all selected A-FEM iterations.

$\boldsymbol{\varepsilon_{R,opt}}$ Optimum value ε_R among whole design space based on the data model.

$\boldsymbol{f}$ Ellipse shape factor, which is the ratio of the minor radius to the major radius in an oval hole.

$\boldsymbol{r}$ Major radius of an oval hole.

$\boldsymbol{\alpha_k}$ Hole Orientation, which is the angle the major radius of an oval hole makes with the *x-axis. k* represents the hole number and is an integer between *1* and *4* in design concept 2, and neglected in design concept 1, as just one hole exists.

$\boldsymbol{\theta}$ Fibre direction, which is the angle the shell's fibres make with the *x-axis.*

$\boldsymbol{h}$ The centres distance of the holes in a row or a column. *h* is just valid for design concept 2, which holes sit in a *2* by *2* matrix's cells.

$\boldsymbol{P}$ The parameters vector, which contains the design variables of the interest.

$\boldsymbol{P_{opt}}$ Optimum *P* which it's elements' values are the values of the corresponding variables at optimum design, where $\varepsilon_R = \varepsilon_{R,opt}$.

1- CHAPTER ONE: INTRODUCTION

1.1 Campaniform Sensillum

Campaniform sensillum (CS), (pl. =Sensilla), is a mechanical receptor in the external skeleton of insects. This is a sensory mechanism which contains a micro hole extruded into the cuticle. A CS in the middle link of an American cockroach is shown in Fig. 1 (this image was taken with Olympus GX41 Inverted microscope with a Moticam 2500 5.0 MP camera mounted on. 200 X magnification).

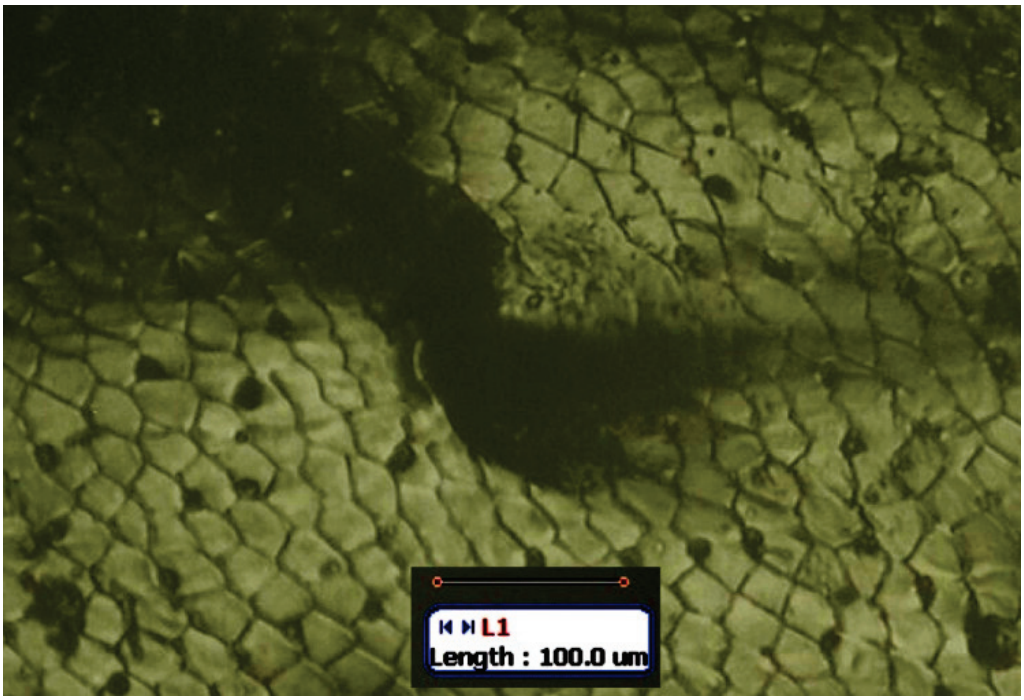

Fig. 1 A campaniform sensillum in the middle link of an American cockroach leg. (Taken with Olympus GX41 Inverted Microscope with a Moticam 2500 5.0 MP camera mounted on. 200X magnification is used)

The CS hole has either circular or oval shape [1]. The cuticle is a multi-layered hard structure outside the epidermis of many invertebrates, which covers and protects the internal organs, and forms the external skeleton. Cuticle is a composite of chitin fibres in a matrix of cross linked protein [2]. The protein fills the gap between chitin fibres. In other words, chitin and the protein, respectively, play the role of fibres and matrix in composite materials, except the protein flexibility in cuticle is changed by the amount of moisture it accumulates [2, 3]. CS is used in nature to mechanically amplify the strain applied to the external cuticle. This amplification appears in the hole's radius deformation [3]. The amplification effect of the campaniform sensillum can be qualitatively explained as follows: when strain is applied to the cuticle, the highest stress in the cuticle is

around the CS because of the well-known stress concentration effect of holes [4]. Due to this high stress, deformation around the hole is much higher than in any other part of the cuticle; the CS therefore acts as strain mechanical amplification system.

In nature, the CS's hole is covered with a bell shape cap; any deformation in the hole's radius causes the cap to buckle up or down. The cap is connected to a transducer organ under the cuticle with a small stick which transfers the cap movement (see Fig. 2). In this thesis, focus is on the mechanical amplification effect of campaniform sensilla – the transducer, consisting of the cap and sensing organ, is not investigated in this work.

Topologically, CS is categorized into three classes: 1) Single Sensillum, 2) Sensilla in group, 3) Sensilla in field [1]. A single campaniform sensillum is shown in Fig. 1 and four campaniform sensilla in arrays of two, which are categorized as group sensilla, are shown in Fig. 3.

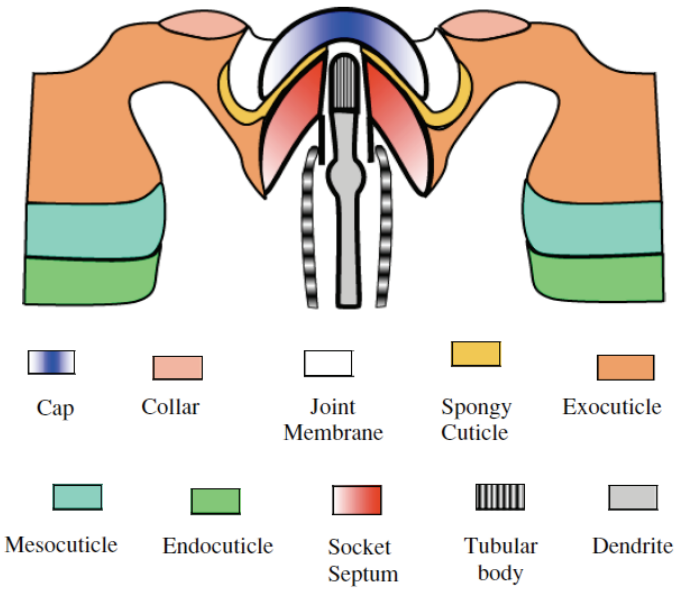

Fig. 2 Cross section illustration of the campaniform sensillum found in the blowfly, Calliphora Vicina (Taken from [5]**. It's an adapted figure from** [6]**).**

CS as a strain sensor has been of interest in engineering science [4, 7]. Campaniform sensillum was modelled in a shell in the previous studies [8, 9]. Strain amplification characteristic of one and group of oval hole(s) in its major and minor radii were studied. These studies were limited to a unidirectional fibre reinforced lamina shell with specific alignment sets of fibre direction and direction of applied strain to the shell, including parallel, normal, and perpendicular. This micro hole reflects the deformation in the structure by changes in its radius size [8, 9]. It was shown that this sensory hole has the capability to amplify the local deformation in the structure. This hole has relatively small size in comparison to the structure.

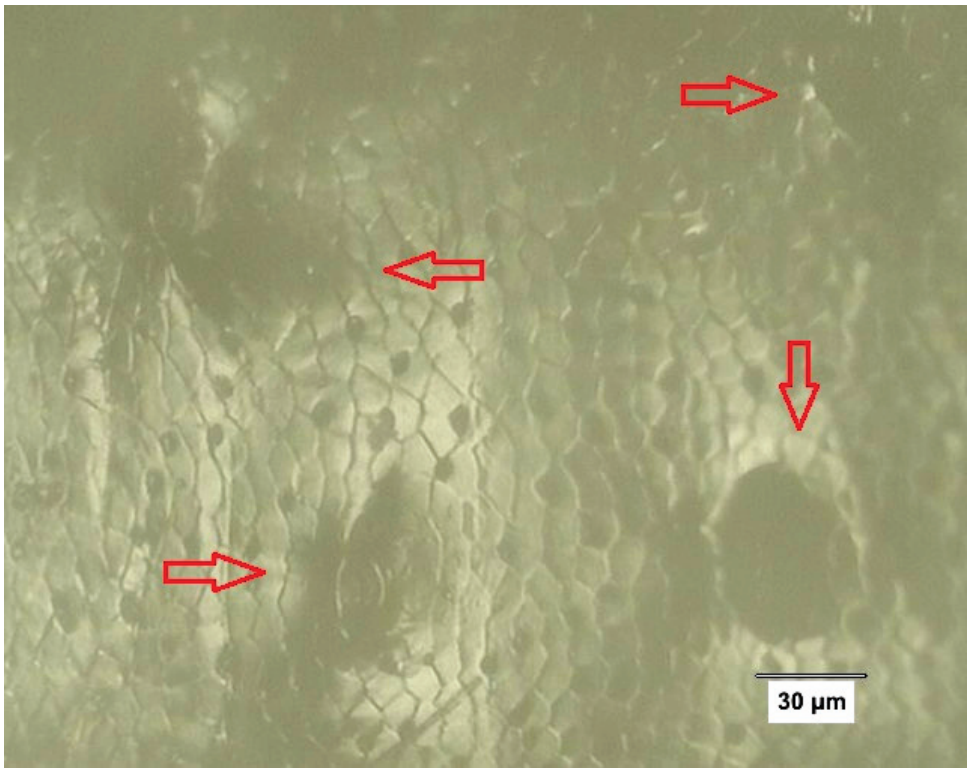

Fig. 3 A group of four campaniform sensilla in the middle link of American cockroach leg. Holes are indicated with red arrows. (Taken with Olympus GX41 Inverted Microscope with a Moticam 2500 5.0 MP camera mounted on. 200X magnification was used)

1.2 Objectives and thesis layout

Objective of this thesis is to investigate how geometrical parameters and material properties affect CS mechanical amplification characteristics. Specifically, the objectives of the thesis are:

Objective 1: Assess which parameters affect amplification features of the holes

Objective 2: Identify an equation representing deformation of the holes as a function of the above mentioned parameters

Objective 3: Obtain an optimal configuration of the holes to maximize strain for a fixed deformation of the substrate, which simulates the cuticle.

By fulfilling these objectives, this thesis will provide background to future work aimed at understanding why CSs have specific geometries in natures. In this work, we consider only two specific CS configurations to focus the scope of this novel research. The two configurations are:

- Design concept 1: A single hole in the middle of a square shell
- Design concept 2: Four holes in arrays of two in the middle of a square shell

Shells in both design concepts are under normal planar strain. The hole(s) are considered to be oval. Since composite material has a similar mechanical structure to cuticle, a unidirectional fibre reinforced lamina, which is an orthotropic material, is employed for the shell.

In order to fulfill the *Objective 1* of the thesis, the finite element method (FEM) is used. Specifically, ANSYS is employed as the primary FEM software. In Chapter two, performance of solid and shell elements are compared. ANSYS results are validated by using another FEM software, COMSOL. In Chapter three, parameters such as geometry and material properties, which affect the strain amplification performance of the hole(s) while the shell is under a constant planar strain, are investigated. These parameters are presented in the FEM simulation as design variables in specific ranges. These ranges define the design space. It should be noted that the presence of several parameters causes a large number of simulation iteration. In order to ease the numerous FEM simulation

iteration attempts, an automatic finite element method (A-FEM) is implemented in this thesis. A-FEM automatically regenerates the design model based on a primary model and covers the entire design space by selective iterations.

In order to fulfill *Objective 2* of the thesis, an artificial neural network (ANN) is employed create a model obtained by fitting data of a database created with A-FEM [10-12]. In order to reduce the dimension of the database, the design parameters that do not sensibly affect or are independent or linearly affect the CS deformation are neglected.

In order to fulfill *Objective 3,* a geometrical optimization is performed in Chapter Five by using the ANN model obtained in Chapter Four. Specifically, two optimization methods, namely the genetic algorithm (GA) and mode perusing sampling (MPS), are used to determine the configuration of the hole(s) orientation(s) and fibre direction which yield the optimum strain [10, 13, 14]. The optimum obtained with GA and MPS using the ANN model is verified by running FEM numerical analysis about the neighborhood of the optimum.

The thesis concludes with Chapter Six, in which conclusions are drawn. Appendix A reviews the mechanical behaviour of unidirectional lamina. The ANSYS template and MATLAB programming files which were used in A-FEM, for design concept 1 are presented in Appendix B. The corresponding weights (weight and bias factors) of the data model of both design concepts are presented in Appendix C.

2- CHAPTER TWO: FEM MODELING

Finite element method (FEM) numerical analysis was implemented for the simulation of both design concepts. The two design concepts investigated in this thesis are illustrated in Fig. 4. The circumference of each hole was divided into *36* segments, each segment subtending an angle equal to 10°, as schematically shown in Fig. 5.These segments identified 36 keypoints on the circumference of each hole and *36* radii, r_i. These radii are equal to each other in the case of an unstretched circular hole. Upon deformation of the shell, the radial strain was computed for each radius r_i as,

$$\boldsymbol{\varepsilon_{r_i}} = \frac{\Delta \boldsymbol{r_i}}{\boldsymbol{r_i}} \tag{1}$$

Subsequently, the maximum radial strain among *36* radii (ε_R) was investigated as,

$$max\ \varepsilon_{r_i} = \varepsilon_R; \qquad i = 1,2,3,\dots,36 \tag{2}$$

Dividing the hole into more segments results in longer simulation time, but more accurate result.

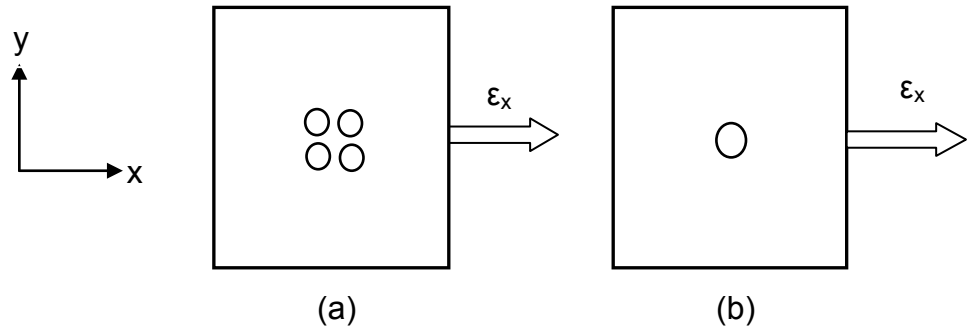

Fig. 4 Two square shells with single hole and four holes in arrays of two in the middle, and the direction of applied planar strain, ε_x.

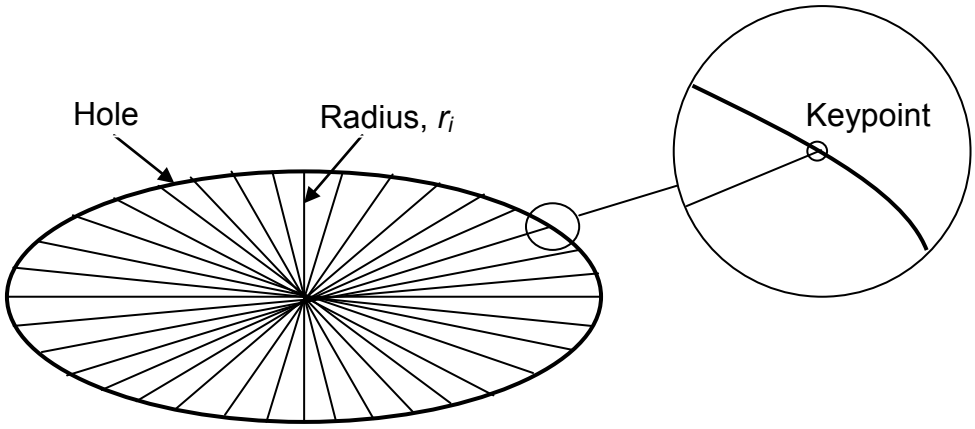

Fig. 5 Oval hole divided into 36 segments. A keypoint is zoomed-in on the right-hand side of the figure.

2.1 FEM Software Selection

ANSYS in batch mode was employed for FEM numerical analysis in this research. ANSYS batch mode obtains an input file and reports the results in an output file. Both input and output are in text format. The input file is generated in ANSYS parametric design language (APDL). Any changes to the design, including geometry, material properties and meshing, could be modified within the input file. The output file consists of the nodal and elemental information. The nodes and elements of interest are selected in the input file to be reported in the output file.

2.2 Meshing and Material Selection

For a better result, a homogeneous meshing around the hole was generated. Fig. 6 and Fig. 7 show examples of solid meshed shells considered for the FEM analysis, respectively for the design concepts 1 and 2. Fig. 8 and Fig. 9 show the homogeneous mesh around the hole in detail, respectively, for design concepts 1 and 2. About 10,000 and 15,000 solid elements were generated correspondingly for design concepts 1 and 2.

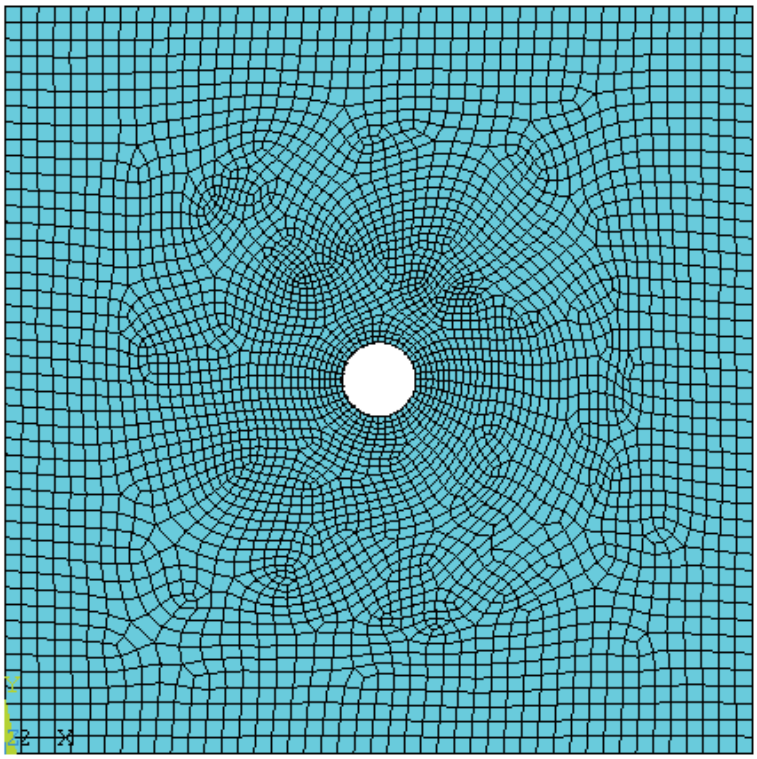

Fig. 6 Solid meshed shell with single hole.

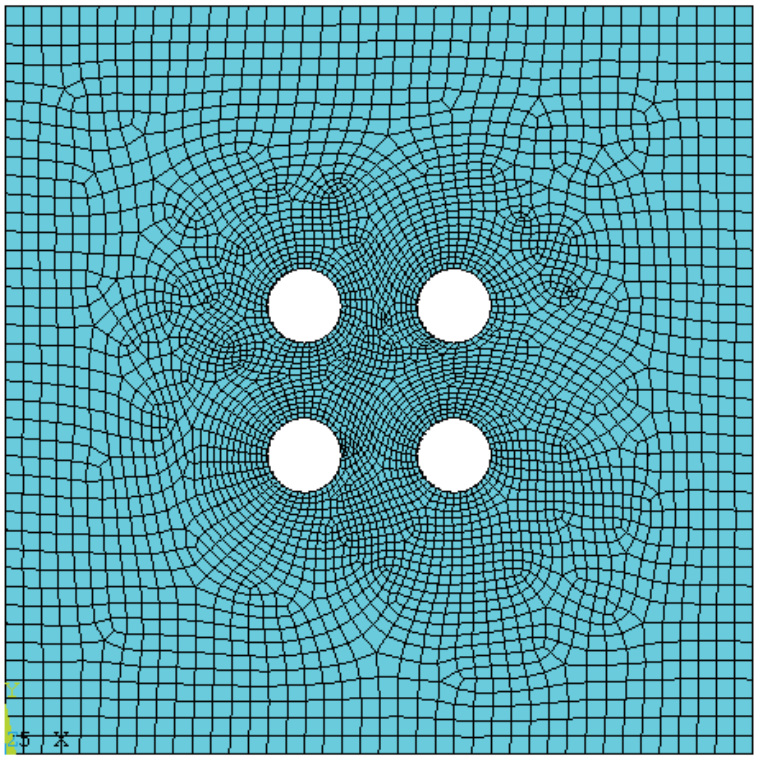

Fig. 7 Solid meshed shell with four holes in arrays of two.

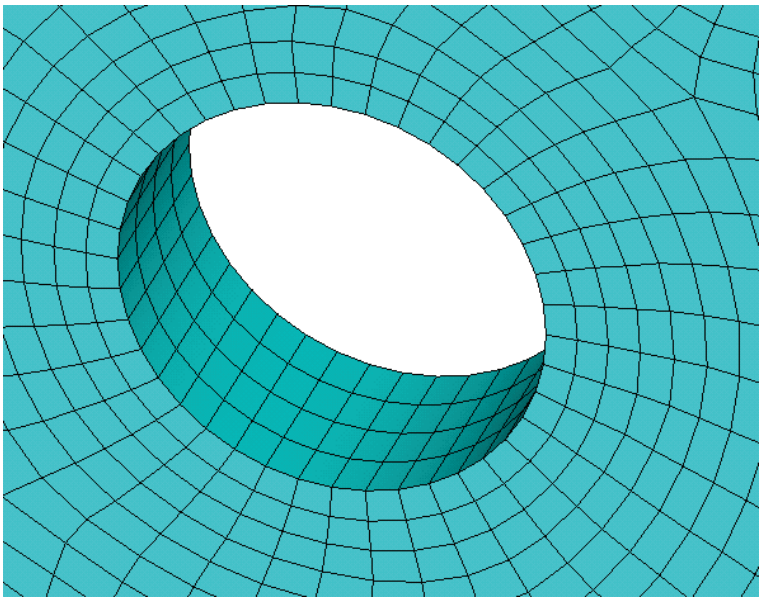

Fig. 8 Zoomed in the solid mesh around the hole in the shell with single hole.

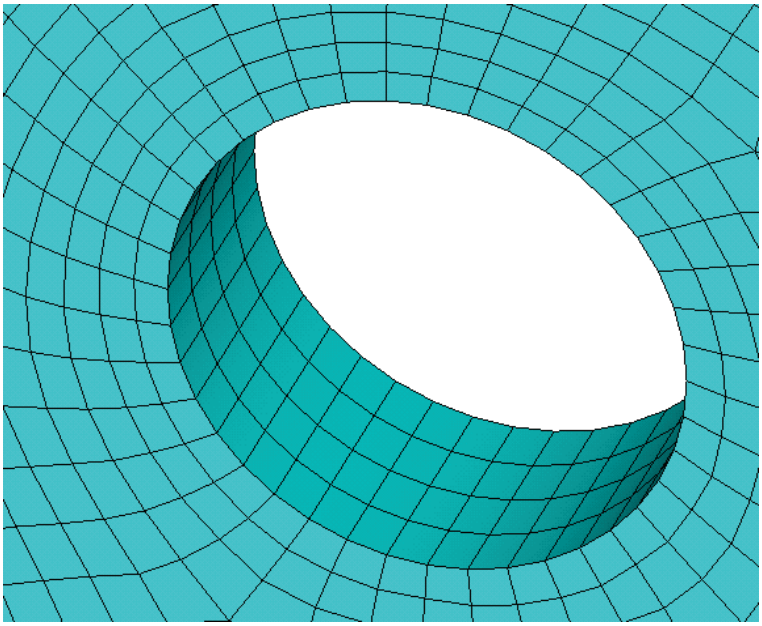

Fig. 9 Zoomed in the solid mesh around one hole in the shell with four holes in arrays of two.

Cuticle has some similarities to composite materials; a unidirectional fibre reinforced lamina was selected for the square shell material. Composite of T300 carbon fibre type and matrix consisting of BSL914C epoxy was selected for both

design concepts to perform the simulations. This selection, which is needed to enable FEM simulations, was arbitrarily chosen and did not restrict the generality of the obtained results. In fact, the analysis was performed for small deformations by assuming linearly elastic materials. The obtained results are therefore scalable for different values of the linear elastic material's properties.

For simulation purpose, material properties proposed in [15] were used; specifically, the Young's Moduli in *x* and *y* directions (see Fig. 3) were respectively $E_x = 138\ GPa$ and $E_y = 11\ GPa$; the Shear Modulus was $G_{xy}=5.5\ GPa$; and the Poisson's ratio was $\nu_{xy}=0.28$. The through thickness, mechanical parameters were calculated as follows:

$$E_z = E_y \tag{3}$$

$$G_{xy} = G_{xz} \tag{4}$$

$$\nu_{xy} = \nu_{xz} \tag{5}$$

$$G_{yz} = E_y/2(1 + \nu_{yz}) \tag{6}$$

Where ν_{yz} was selected to be equal to *0.4*. The thickness of the lamina, *t*, was chosen to be 100μm. The unidirectional fibre reinforced lamina performs as

a transversely isotropic material (see Appendix A for more information about elastic behaviour of unidirectional lamina and transversely isotropic materials).

2.3 Element Selection

Shell elements performance for a plane unidirectional lamina under normal stress in *x* direction was verified. The analytical and theoretical results were consistent. Fig. 10 shows the strain along *x-axis*, ε_x, and *y-axis*, ε_y, when shell is under normal stress along *x-axis,* using *Shell63*. The blue curve represents ε_x and the green curve represents ε_y. The red dots and blue circles were calculated theoretically.

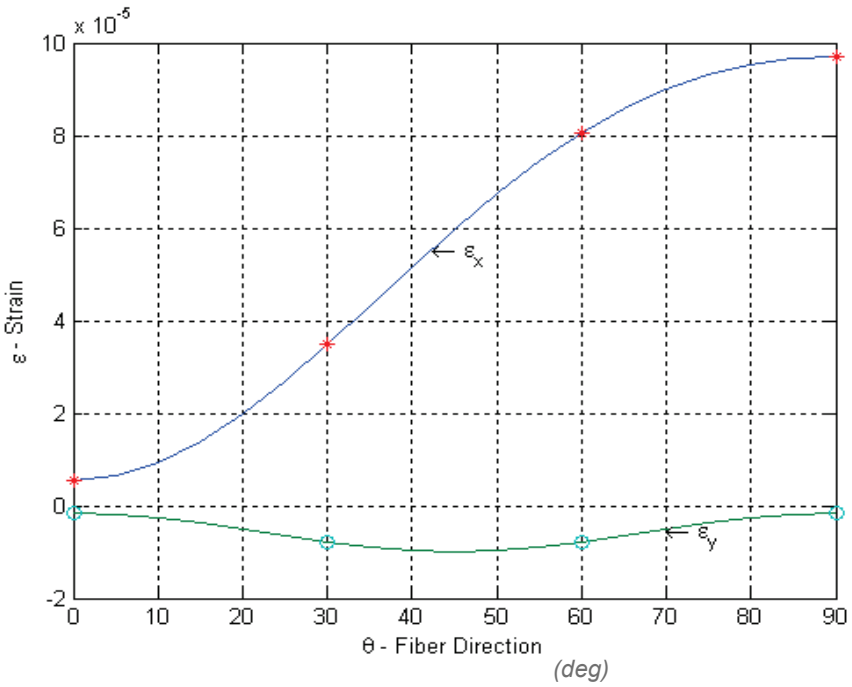

Fig. 10 Strain along *x-axis* (blue line) and y-axis (green line) on a plane unidirectional fibre reinforced lamina using ANSYS *Shell63* elements. The red dots and blue circles illustrate the theoretical strain calculation respectively in *x* and *y* direction at *0˚, 30˚, 60˚* and *90˚*.

However, in the presence of hole(s) in the shell, the simulation result with shell elements was not satisfactory. The deformation contour plots represent scattered results with shell elements. Fig. 11 and Fig. 12 respectively show the displacement of the shell along *x* and *y-axes* with *Shell 63* elements. On the other hand, the simulation results of the deformation contour plot with solid elements, i.e. *Solid185*, *Solid186* and *Solid95*, are fine and symmetrical. Fig. 13 and Fig. 14 respectively show the displacement of the shell along *x* and *y-axes* with *Solid 95* elements, for the same configuration considered in Fig. 11 and Fig. 12. Among solid elements, only *Solid95* can tolerate irregular shapes, like a very oval hole, without much loss of accuracy. Its elements have compatible displacement shapes and are well suited to model curved boundaries. *Solid 95* is

defined by *20* nodes with three degrees of freedom (translations in the nodal *x*, *y*, and *z* directions) at each node. The elements' spatial orientation could be changed by defining a new active coordinate system; it gives the capability to define the fibres' direction in an orthotropic material.

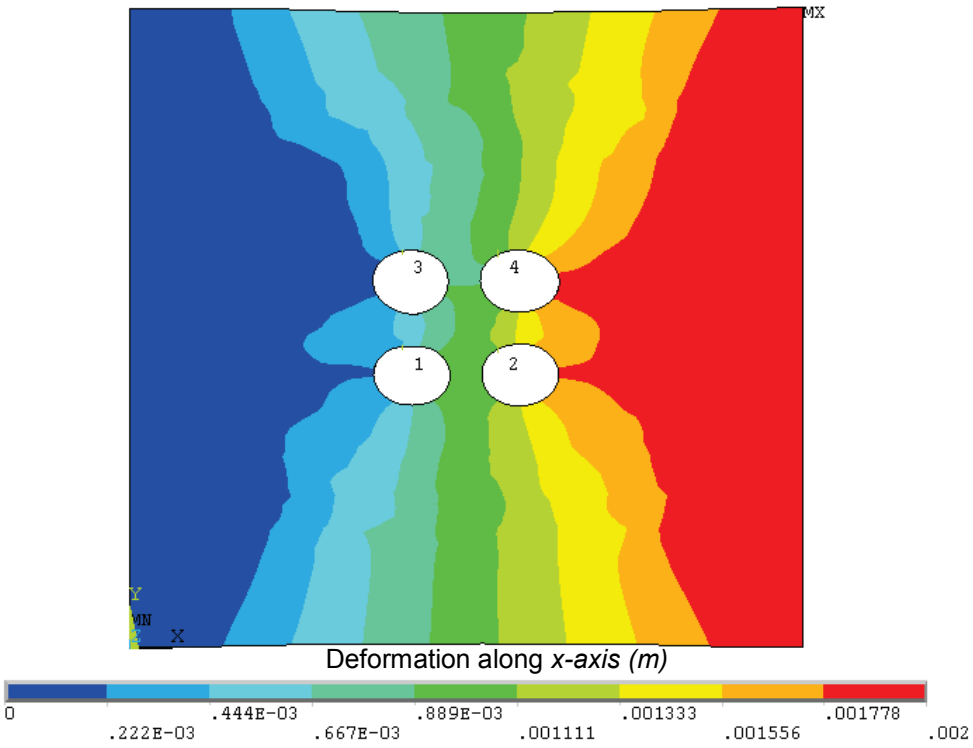

Fig. 11 Deformation contour plot along *x-axis* in the shell (T300/BSL914C unidirectional fibre reinforced lamina composite) with four holes in arrays of two using ANSYS *Shell63* elements (ε_x*=0.1%,* fibre direction=*0˚*, holes orientations=*0˚*, *f=1,* shell size=*2 by 2mm*, shell thickness=*100μm,* hole radius=*100μm*, holes' centres distance=*300μm,* and holes are circular).

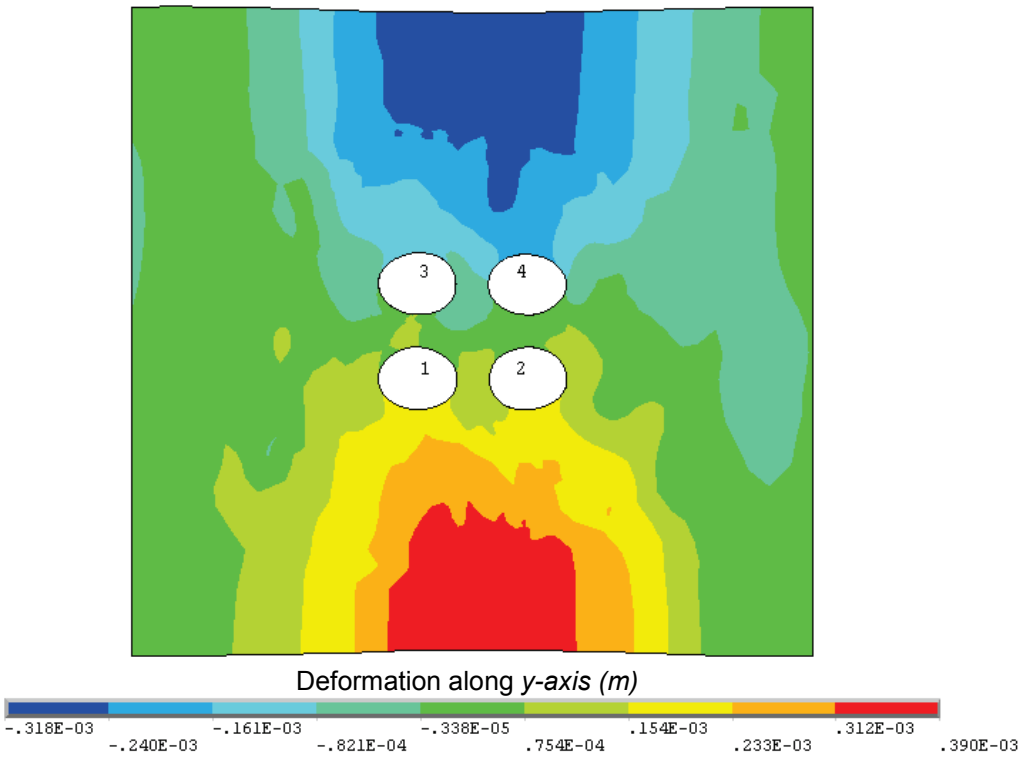

Fig. 12 Deformation contour plot along *y-axis* in the shell (T300/BSL914C unidirectional fibre reinforced lamina composite) with four holes in arrays of two using ANSYS *Shell63* elements (ε_x*=0.1%,* fibre direction=*0˚*, holes orientations=*0˚*, *f=1,* shell size=*2 by 2mm*, shell thickness=*100μm,* hole radius=*100μm*, holes' centres distance=*300μm,* and holes are circular).

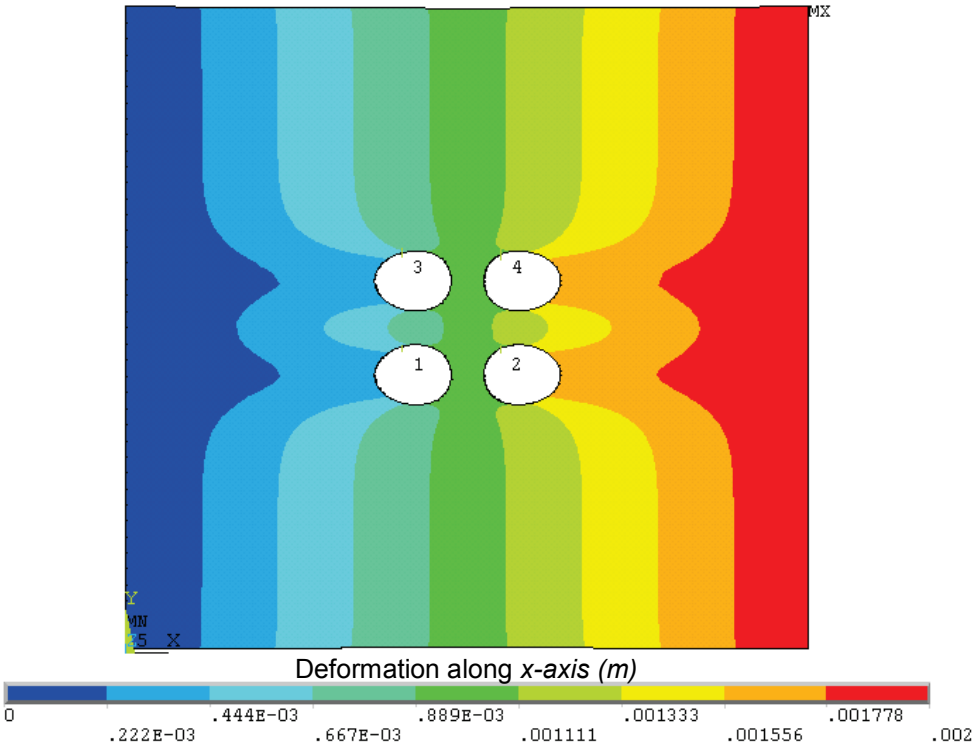

Fig. 13 Deformation contour plot along *x-axis* in the shell (T300/BSL914C unidirectional fibre reinforced lamina composite) with four holes in arrays of two using ANSYS *Solid95* elements (ε_x*=0.1%,* fibre direction*=0˚,* holes orientations*=0˚, f=1,* shell size*=2 by 2mm*, shell thickness*=100μm,* hole radius*=100μm*, holes' centres distance*=300μm,* and holes are circular).

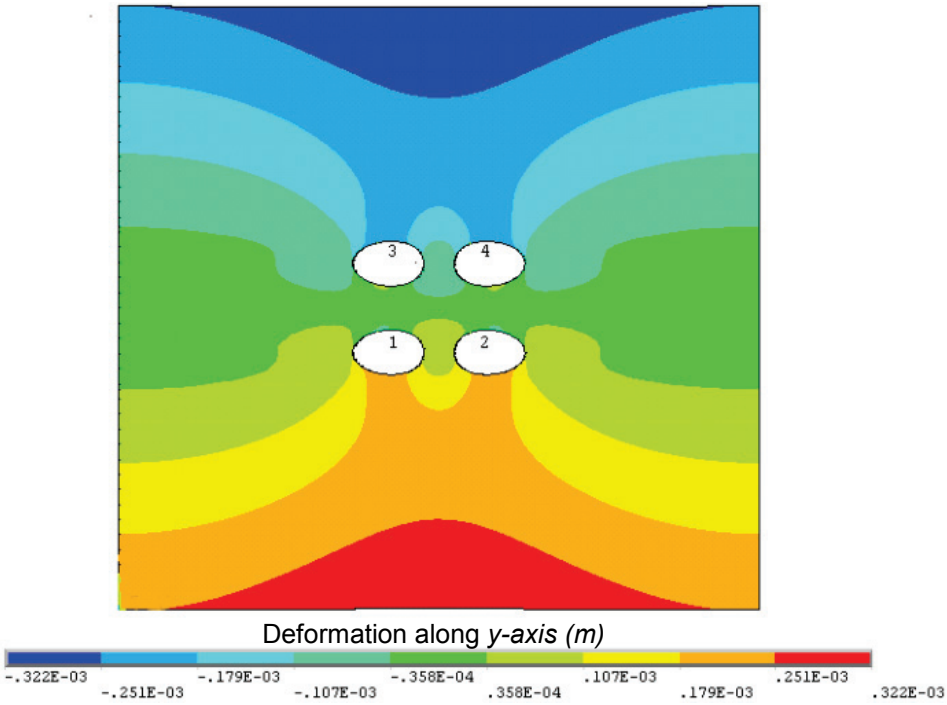

Fig. 14 Deformation contour plot along *y-axis* in the shell (T300/BSL914C unidirectional fibre reinforced lamina composite) with four holes in arrays of two using ANSYS *Solid95* elements (ε_x*=0.1%,* fibre direction=*0˚,* holes orientations=*0˚, f=1,* shell size=*2 by 2mm*, shell thickness=*100μm,* hole radius=*100μm*, holes' centres distance=*300μm,* and holes are circular).

A shell having a side exceeding by an order of magnitude the size of the hole(s) was considered to be suitable for neglecting the border effect of the shell on the A-FEM outputs. Since the stress effect of hole(s) is limited to its/their very close neighbourhood, a *2* by *2mm* square shell (*a=2mm*) was considered for the simulation. Fig. 15 and Fig. 16 illustrate and compare the von Mises stress in two square shells of *a=2mm* and *a=10mm* with four holes in arrays of two. They are both under normal planar strain ε_x*=0.1%*. Fig. 17 is a magnification of Fig. 16.

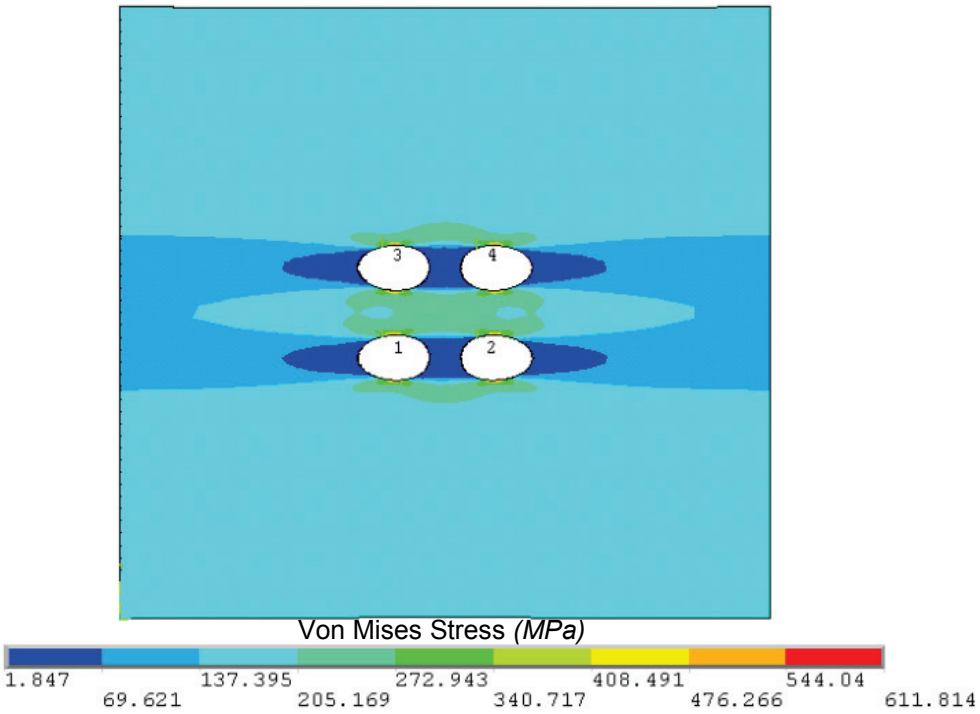

Fig. 15 Von Mises stress contour plot in the shell (T300/BSL914C unidirectional fibre reinforced lamina composite) with four holes in arrays of two using ANSYS *Solid95* elements (ε_x=*0.1%,* fibre direction=*0˚,* holes orientations=*0˚, f=1,* shell size=*2 by 2mm*, shell thickness=*100μm,* hole radius=*100μm*, holes' centres distance=*300μm,* and holes are circular).

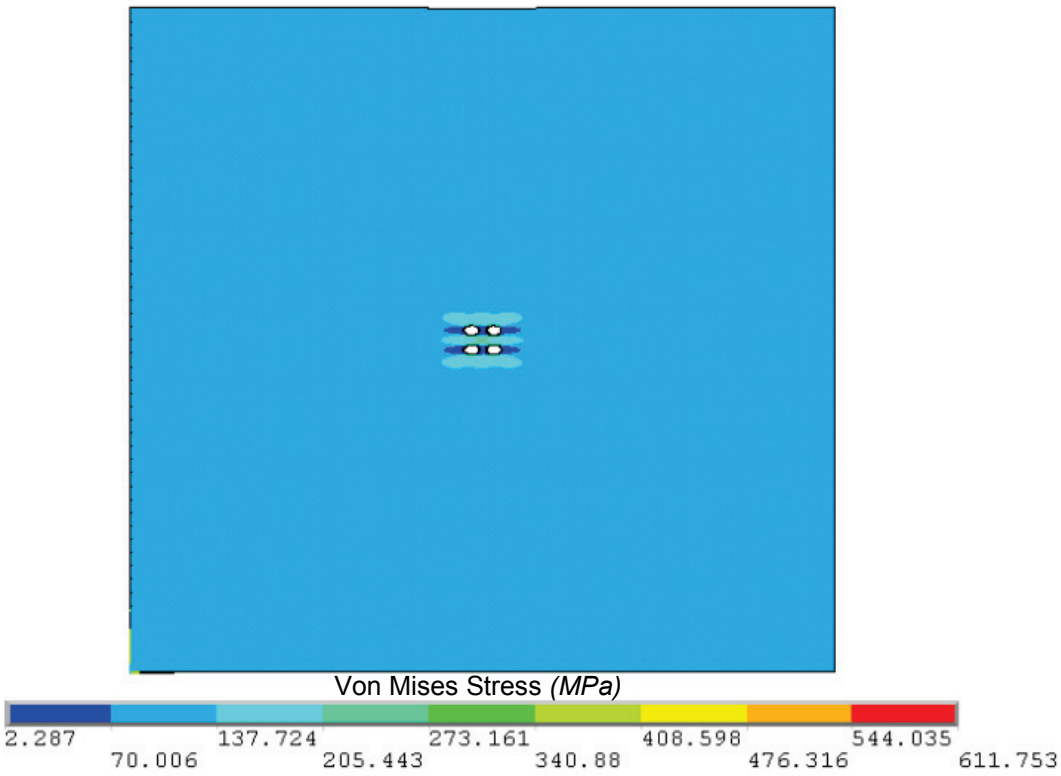

Fig. 16 Von Mises stress contour plot in the shell (T300/BSL914C unidirectional fibre reinforced lamina composite) with four holes in arrays of two using ANSYS *Solid95* elements (ε_x=*0.1%,* fibre direction=*0˚,* holes orientations=*0˚, f=1,* shell size=*10 by 10mm*, shell thickness=*100μm,* hole radius=*100μm*, holes' centres distance=*300μm,* and holes are circular).

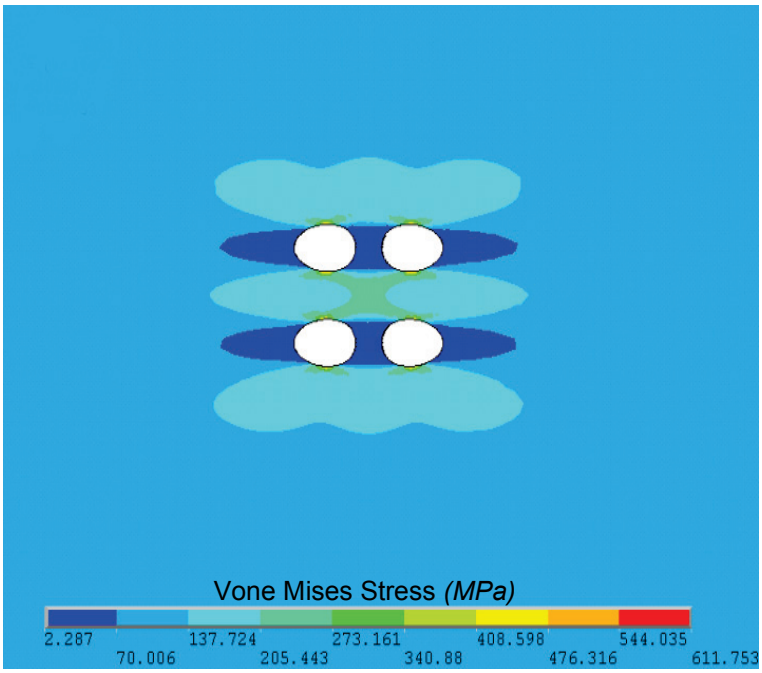

Fig. 17 Zoomed in - von Mises stress contour plot in the shell (T300/BSL914C unidirectional fibre reinforced lamina composite) with four holes in arrays of two using ANSYS *Solid95* elements (ε_x=*0.1%,* fibre direction=*0˚,* holes orientations=*0˚, f=1,* shell size=*10 by 10mm*, shell thickness=*100μm,* hole radius=*100μm*, holes' centres distance=*300μm,* and holes are circular).

In the previous contour plots, (Fig. 11 -Fig. 17) circular holes (*f=1*) were considered for the ANSYS FEM simulation. It should be noted that ANSYS automatically applied a scale factor to all contour plots (Fig. 11 -Fig. 17) in order to visualize the deformation, otherwise they are too small to be noticed.

2.4 Comparison with other FEM Software

The deformation along *x and y-axes* and also von Mises stress contour plot which were computed with ANSYS, and are shown in Fig. 13 - Fig. 15, were compared and verified with another FEM software, COMSOL. Fig. 18, Fig. 19 and Fig. 20, which were simulated with COMSOL, are respectively comparable to

Fig. 13, Fig. 14 and Fig. 15. The maximum deformation along *x and y-axes* and maximum von Mises stress calculated with ANSYS and COMSOL were very similar. Since the maximum error was less than 2%, the results were validated. This comparison confirmed that the ANSYS element Solid 95 was suitable for investigating deformations of CSs.

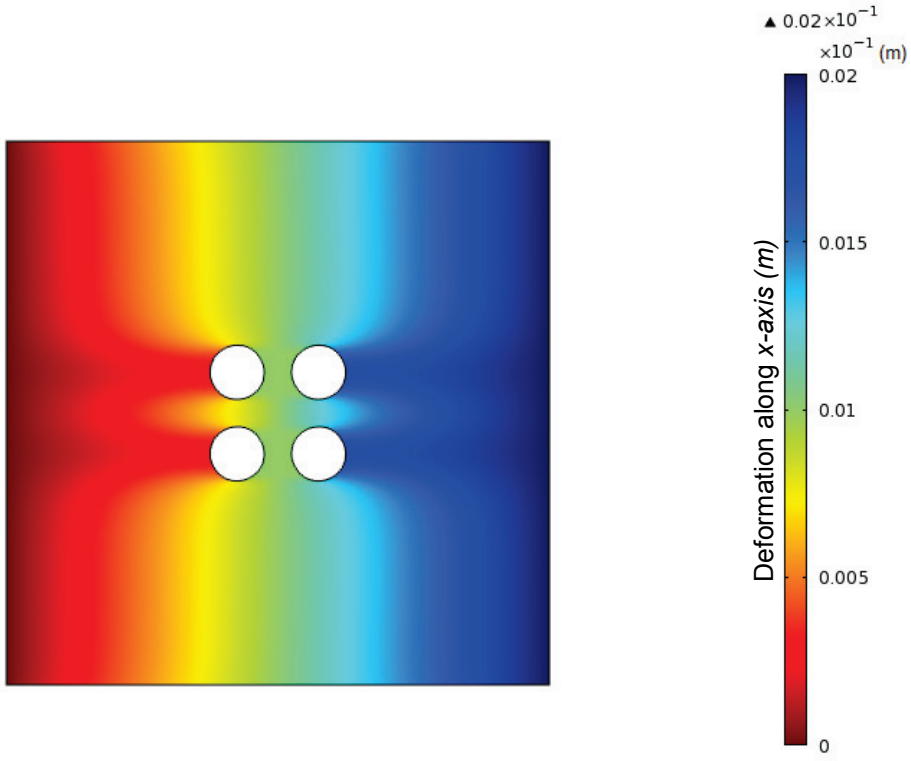

Fig. 18 Deformation contour plot along *x-axis* in the shell (T300/BSL914C unidirectional fibre reinforced lamina composite) with four holes in arrays of two using COMSOL (ε_x=*0.1%,* fibre direction=*0˚,* holes orientations=*0˚, f=1,* shell size=*2 by 2mm*, shell thickness=*100μm,* hole radius=*100μm*, holes' centres distance=*300μm,* and holes are circular).

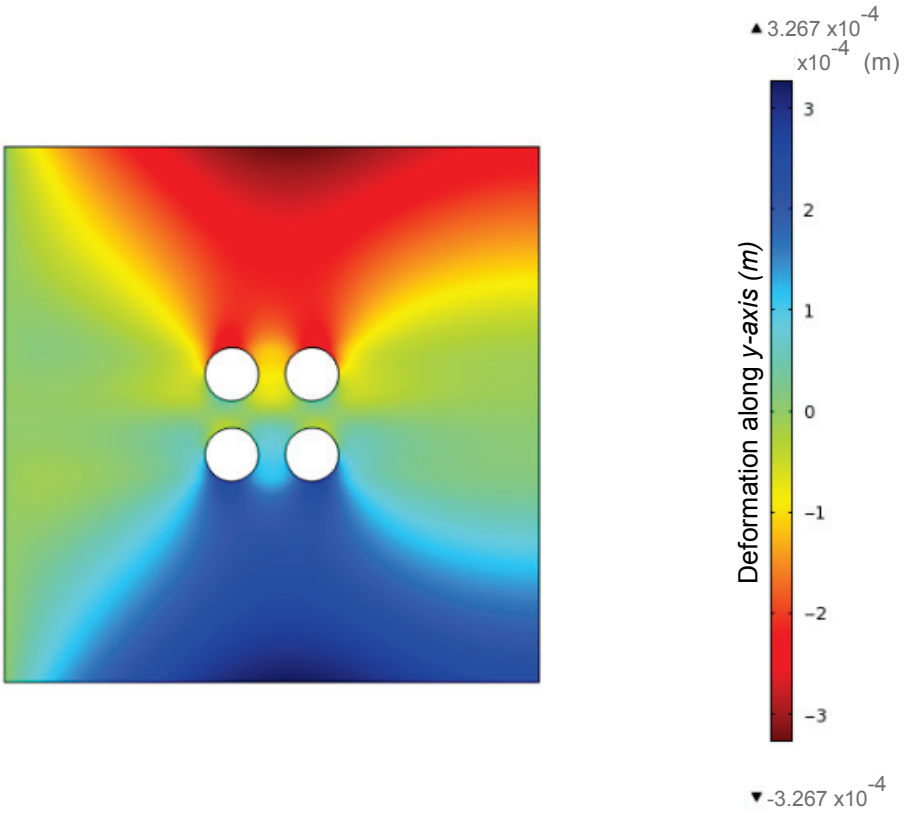

Fig. 19 Deformation contour plot along *y-axis* in the shell (T300/BSL914C unidirectional fibre reinforced lamina composite) with four holes in arrays of two using COMSOL (ε_x=*0.1%,* fibre direction=*0˚,* holes orientations=*0˚, f=1,* shell size=*2 by 2mm*, shell thickness=*100μm,* hole radius=*100μm*, holes' centres distance=*300μm,* and holes are circular).

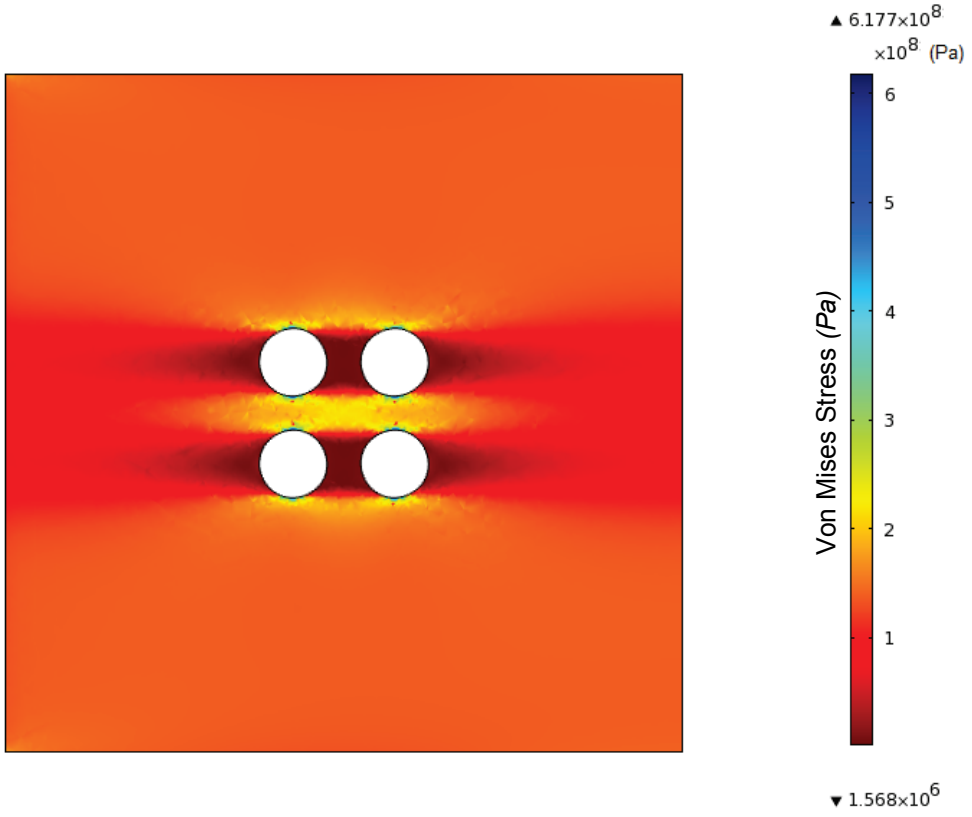

Fig. 20 Von Mises stress contour plot in the shell (T300/BSL914C unidirectional fibre reinforced lamina composite) with four holes in arrays of two using COMSOL (ε_x=*0.1%,* fibre direction=*0˚,* holes orientations=*0˚, f=1,* shell size=*2 by 2mm*, shell thickness=*100μm,* hole radius=*100μm*, holes' centres distance=*300μm,* and holes are circular).

2.5 A-FEM Method Structure and Sequences

In order to run the FEM simulation over the entire design space, a new input file should be generated for each simulation iteration. Due to the large number of variables and steps per variable, numerous iterations were required. In order to make this process autonomous, these modifications were set to be applied automatically with a programming software, such as MATLAB. It is so-called automatic finite element method (A-FEM) analysis, in this research.

In this method, a preliminary template file is created, and then the input file is regenerated from this template file in each simulation iteration attempt. Within MATLAB, the template file is scanned, first. The design variable in the template file is initially undefined. After the values of variables are added at the beginning of the template file, an input file is created. Then by executing the input file in ANSYS, an output file is produced. ANSYS is called via MATLAB in DOS environment and runs in batch mode. Output file contains information which is not entirely useful for calculating the maximum ε_r (ε_R). ε_R is to be found in each simulation iteration. The output file, then, is scanned by MATLAB and the displacements at *36* specified keypoints (see Fig. 4) around the hole(s) are stored as rough-data. This rough-data should be post-processed in order to compute 36 values of ε_r and then ε_R is investigated for each iteration. Consequently, after all iterations are done, a database of ε_R for each possible set of design variable values, with specific iterations over the design space, is generated. The template file and MATLAB programming files are presented in Appendix B.

The computational time for each simulation took about *75 s* and *120 s* respectively for concept design 1, in which only one hole was considered, and concept design 2, in which four holes were considered, with a Core2 Duo 2.33GHz processor and 3.75GB RAM. A-FEM is implemented for the FEM simulations in “section 3.3”.

3- CHAPTER THREE: FEM ANALYSIS

In this chapter, the influences of design variables on ε_R are individually studied, in both design concepts. The variables considered in this work are as follows:

1) The hole(s) orientation(s), α_k, which is defined as the angle between the major radius of the hole *k* and the *x-axis,* where *k* is an integer between *1* and *4* in design concept 2, and neglected in design concept 1, as just one hole exists.

2) The fibre direction, θ, which is defined as the angle between the fibres of the lamina and the *x-axis*;

3) Ellipse shape factor, *f*, which is defined as the ratio of the minor radius to the major radius of the hole(s);

4) Major hole's radius, *r*, of the hole(s);

5) Holes' centres distance, *h* (only applicable in the shell with four holes).

Fig. 20 and Fig. 21 show the geometrical design variables respectively for the concept designs 1 and 2.

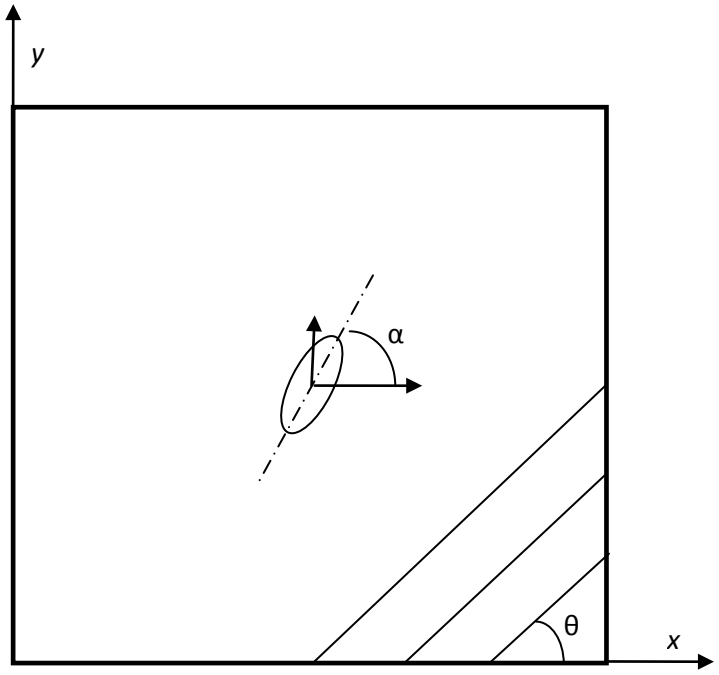

Fig. 21 Fibre direction, θ, and hole orientation, α, are illustrated in a shell with single hole.

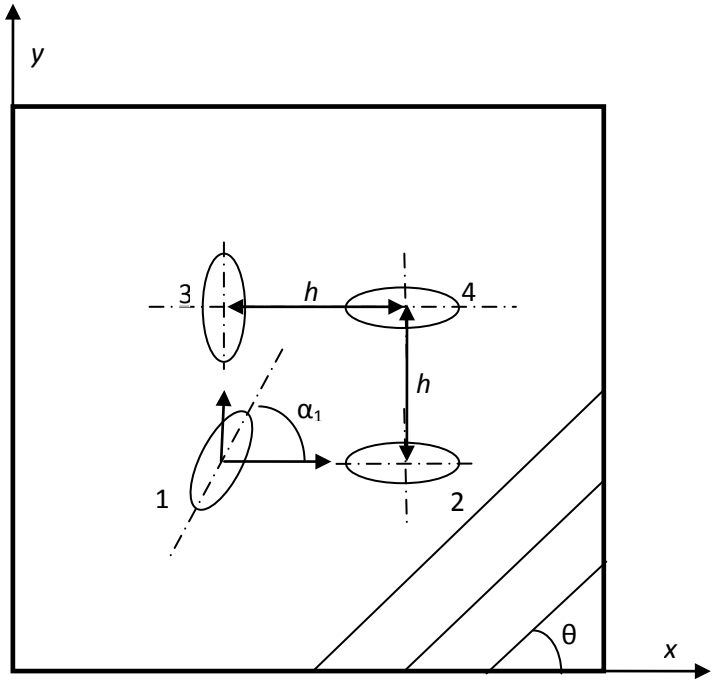

Fig. 22 Fibre direction, θ, hole orientation for hole no. 1, α_1, hole (centre) distances, h, are illustrated in a shell with four holes in array of two.

3.1 Influence of Material Properties

Investigations were performed in order to assess whether some design variables could be approximated through simple very analytical equations. In the following sections, influence of the material properties on ε_R are discussed.

3.1.1 Design Concept 1

Longitudinal elasticity modulus, E_x, vs. ε_R showed a linear characteristic; specifically, ε_R increases when the longitudinal elasticity increases. This variable was a function of neither θ, nor α, and always represented linear positive slope behaviour (see Fig. 23).

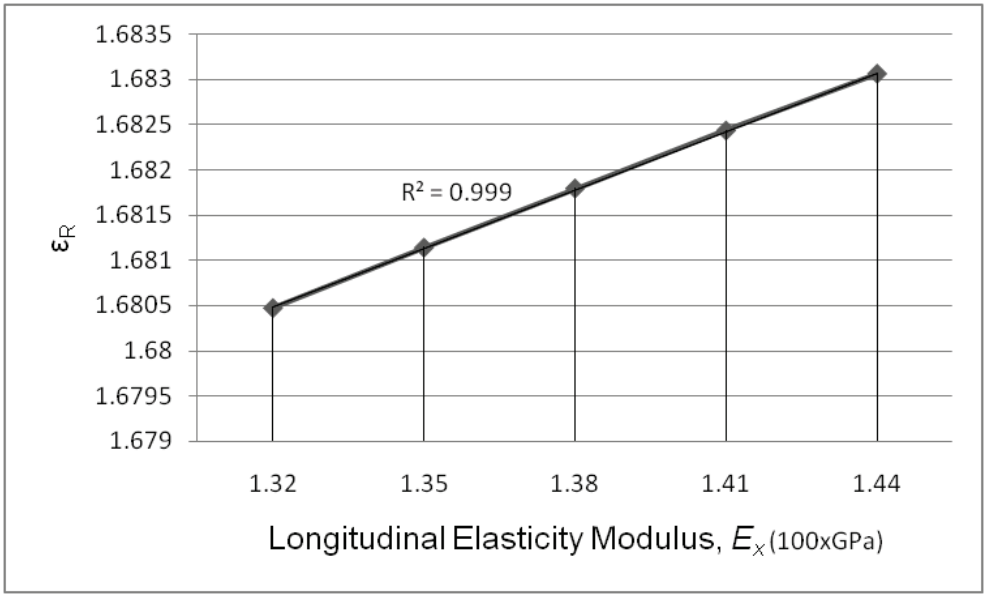

Fig. 23 E_x vs. ε_R while $\theta=0^\circ$, $\alpha=0^\circ$, $r=100\mu m$ and $f=0.8$.

Transverse elasticity modules, E_y, vs. ε_R was linear for all α and θ (see Fig. 24); however for different α, E_y, vs. ε_R has different slope. Specifically the slope was negative for $15^\circ<\alpha<65^\circ$, $115^\circ<\alpha<165^\circ$, $195^\circ<\alpha<245^\circ$ and $295^\circ<\alpha<345^\circ$,

and positive for *-15˚<α<15˚, 65˚<α<115˚, 165˚<α<195˚* and *245˚<α<295˚.* Fig. 25 illustrates the positive and negative E_y, vs. ε_R slope respectively with arrows head up and down while *α* is changing *0˚ to 360˚*.

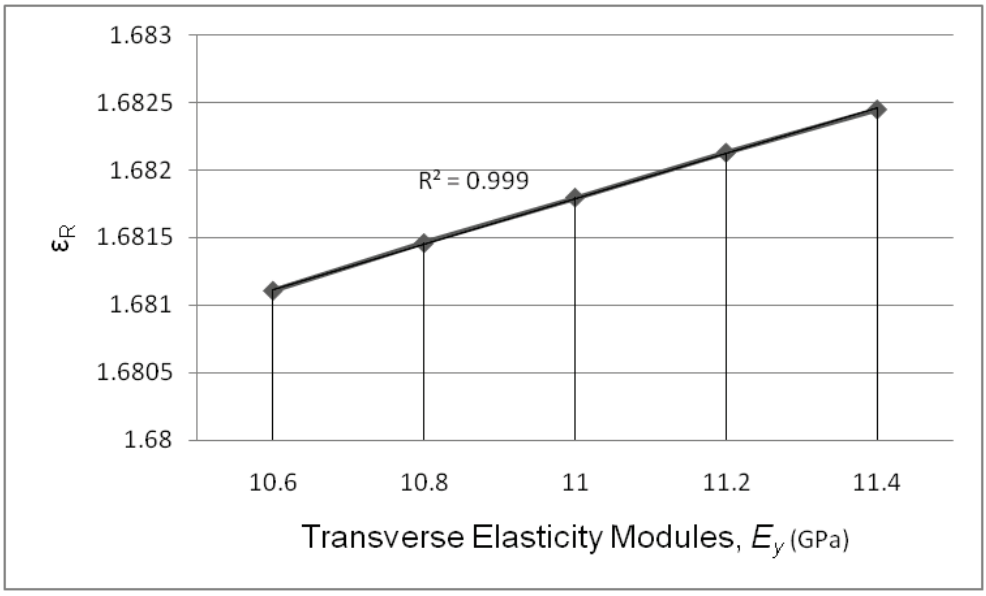

Fig. 24 E_y vs. ε_R while *θ=0˚, α=0˚, r=100μm* and *f=0.8*.

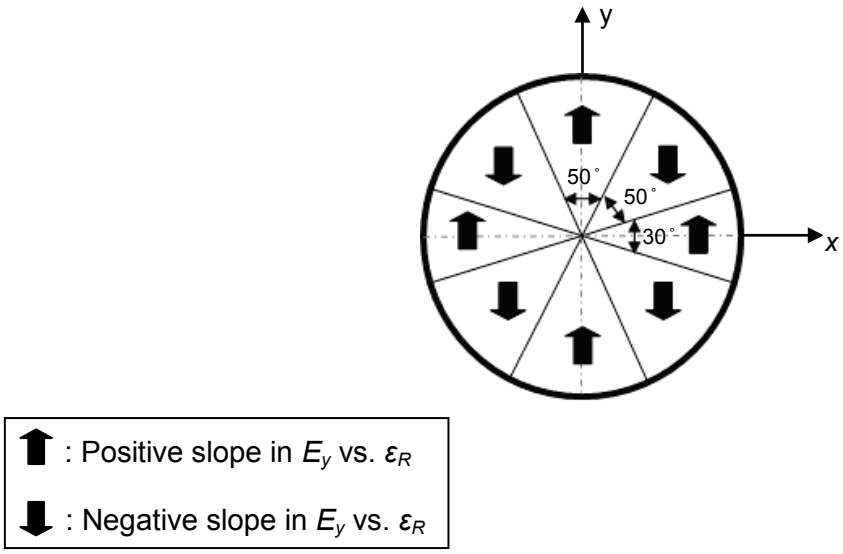

Fig. 25 E_y vs. ε_R linear slope changes for a complete *360˚* rotation of hole, *α*, while *θ=0˚*, *r=100μm* and *f=0.8*. The arrows represent the positive slope and negative slope of the linear trend in specific *α* districts.

Shear modulus, G_{xy}, vs. ε_R also demonstrated linear behaviour (see Fig. 26). Its slope is independent from *α*; whereas, for different *θ*, it shows different linear slope. Specially the slope was positive for *15˚<θ<75˚, 105˚<θ<165˚, 195˚<θ<255˚* and *285˚<θ<345˚*, and negative for *-15˚<θ<15˚, 75˚<θ<105˚, 165˚<θ<195˚* and *255˚<θ<285˚*, for any arbitrary selected *α*. Fig. 27 illustrates the positive and negative G_{xy}, vs. ε_R slope respectively with arrows head up and down while *θ* is changing *0˚ to 360˚*.

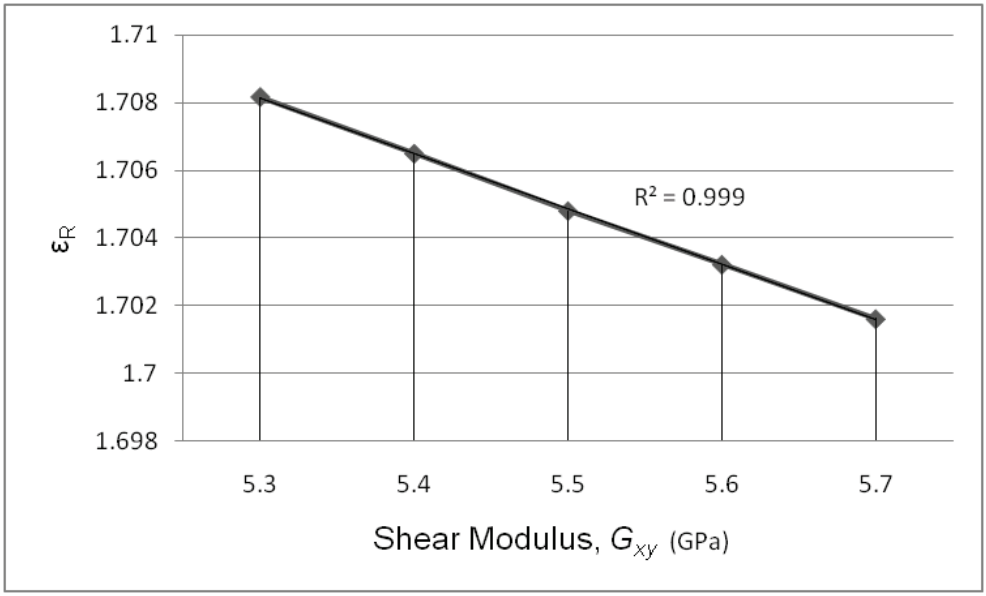

Fig. 26 ***G_{xy} vs.*** **ε_R while** ***θ=0˚, α=0˚, r=100μm*** **and** ***f=0.8.***

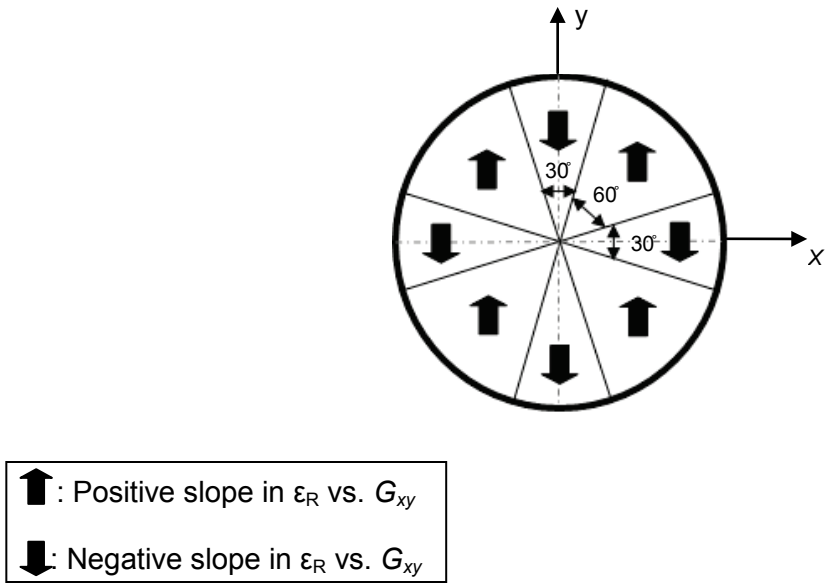

Fig. 27 ***G_{xy}*** **vs.** ***ε_R*** **linear slope changes for a complete** ***360˚*** **rotation of fibres,** ***θ*****, while** ***α =0˚*****,** ***r=100μm*** **and** ***f*****=0.8. The arrows represent the positive slope and negative slope of the linear trend in every region.**

Poisson ratio, ν_{xy}, had the least influence on ε_R among other material properties. The ε_R stays almost constant while ν_{xy} varies from *0.25* to *0.35*, as shown in Fig. 28, but still ν_{xy} vs. ε_R tends to have a negative slope and the variation of ε_R is negligible. ν_{xy} typically is between *0.25* and *0.35* for unidirectional carbon fibre reinforced lamina.

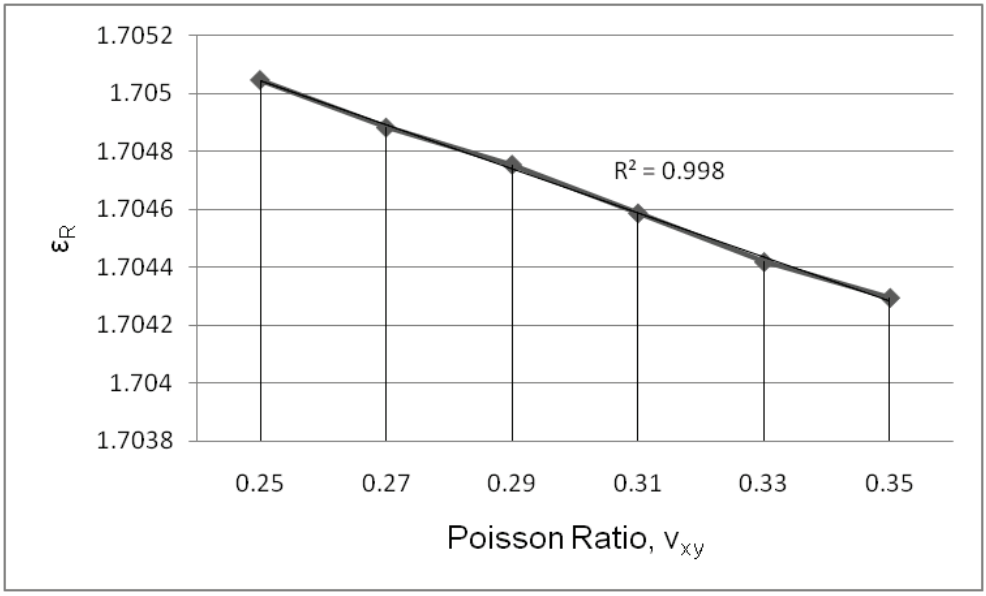

Fig. 28 ν_{xy} vs. ε_R while *θ=0˚, α=0˚, r=100μm* and *f=0.8.*

3.1.2 Design Concept 2

Longitudinal elasticity modulus, E_x vs. ε_R illustrated linear behaviour for all hole orientations and fibre directions, as shown in Fig. 29. Transverse elasticity modulus, E_y vs. ε_R represented linear relation for all holes orientations and fibre directions, as well (see Fig. 30). Fig. 31 shows that ε_R is linearly related to G_{xy}.

E_x, E_y *and* G_{xy} vs. ε_R had linear trend notwithstanding how the holes and fibres were oriented. Poisson ratio, ν_{xy}, variation had a minor influence on ε_R. Fig. 32 shows that ν_{xy} vs. ε_R is almost constant, but still tend to have negative slope.

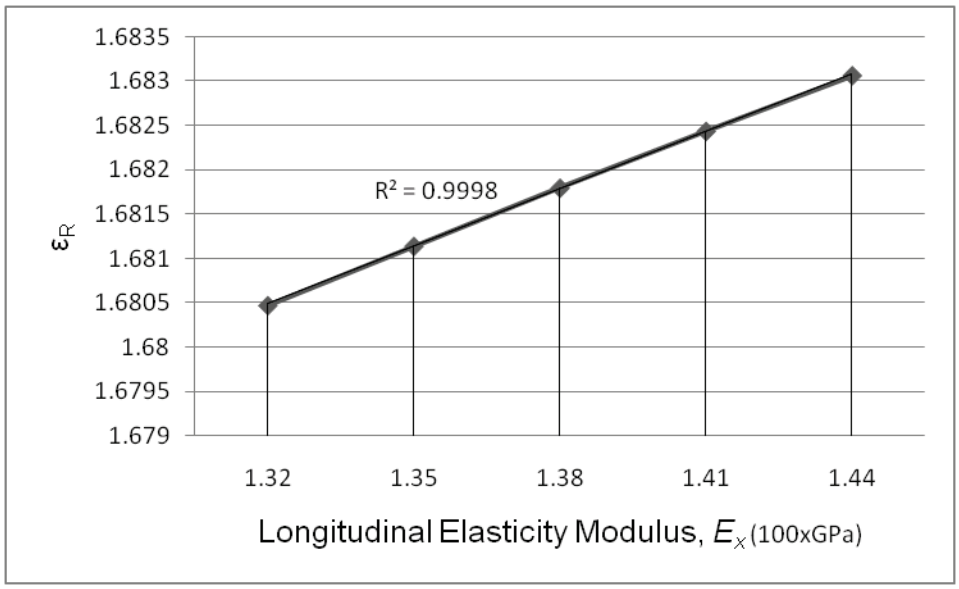

Fig. 29 E_x **vs.** ε_R **while** $\theta=0^\circ$, $\alpha_k=0^\circ$, $r=100\mu m$, $h=300\mu m$ **and** $f=0.8$.

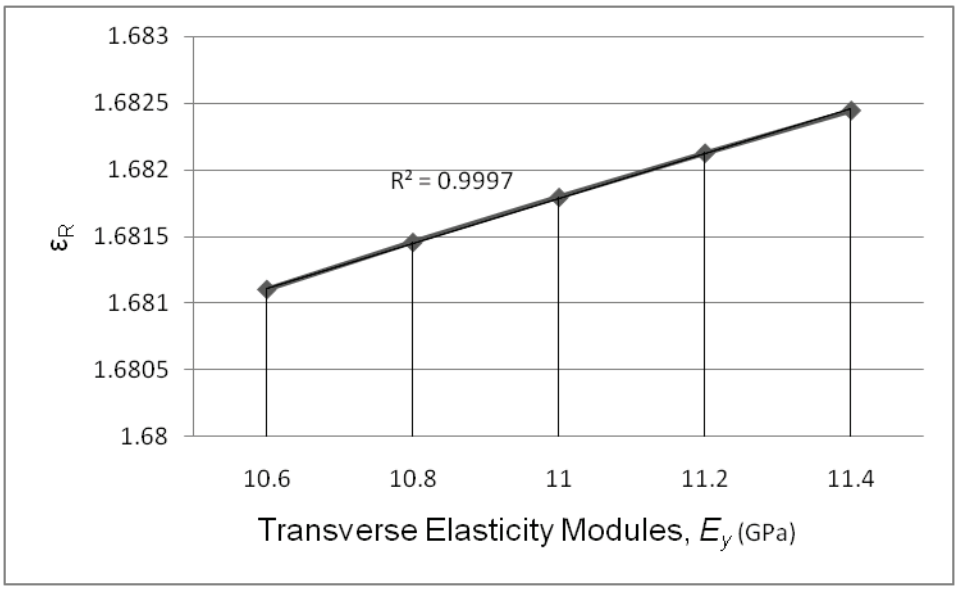

Fig. 30 E_y **vs.** ε_R **while** $\theta=0^\circ$, $\alpha_k=0^\circ$, $r=100\mu m$, $h=300\mu m$ **and** $f=0.8$.

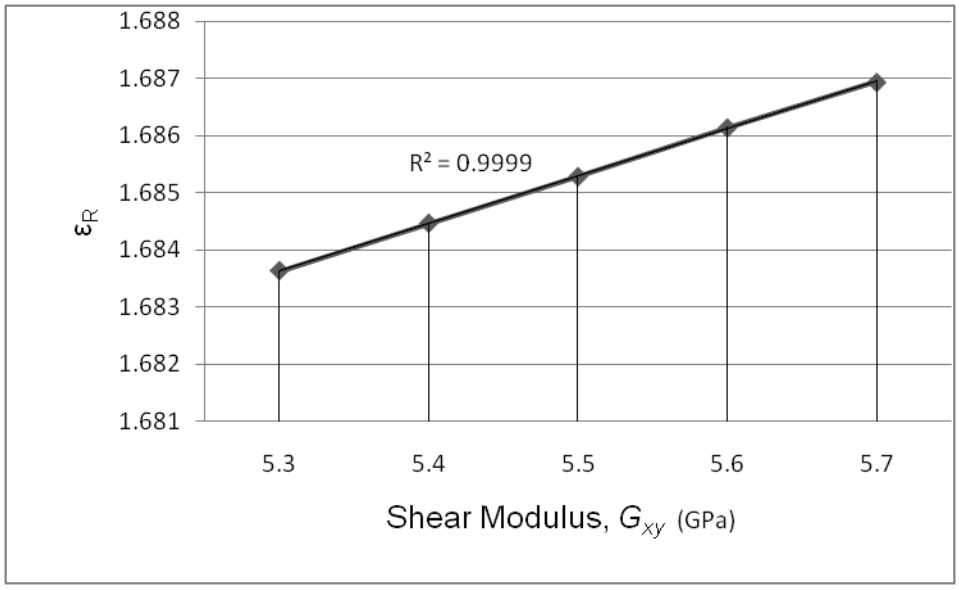

Fig. 31 G_{xy} **vs.** ε_R **while** $\theta=0^\circ$, $\alpha_k=0^\circ$, $r=100\mu m$, $h=300\mu m$ **and** $f=0.8$.

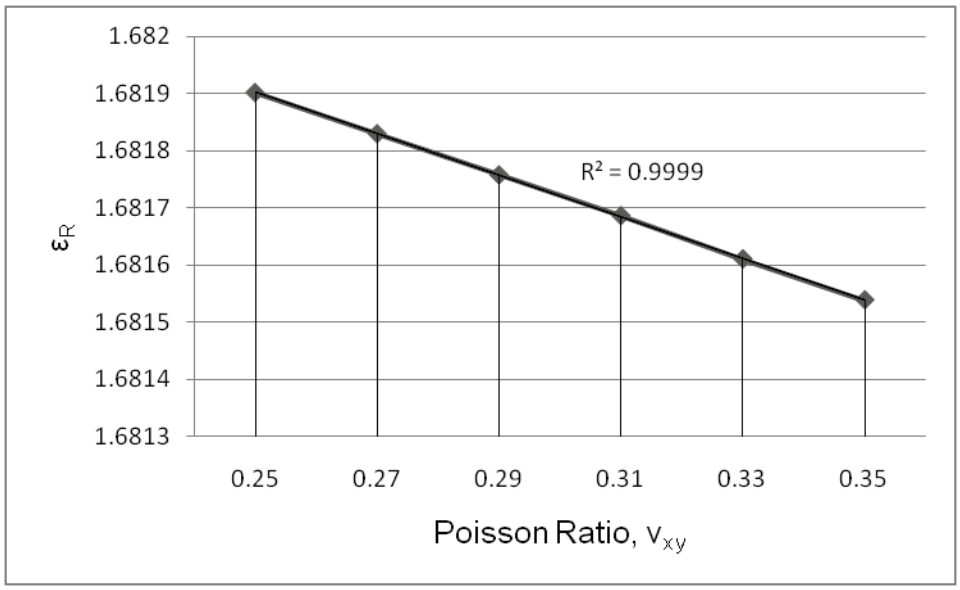

Fig. 32 ν_{xy} vs. ε_R, while $\theta=0^\circ$, $\alpha_k=0^\circ$, $r=100\mu m$, $h=300\mu m$ and $f=0.8$.

From the above-mentioned results, for both design concepts 1 and 2, it can be deduced that the influence of the material properties on ε_R can be either modelled with simple linear functions or neglected. In order to reduce the computational time of A-FEM simulations, these variables were therefore neglected in the subsequent investigations.

3.2 Influence of Parameters *f* and *r*

In this section, a sensitivity analysis is presented. Such an analysis was performed to assess if the ellipse shape factor, *f*, defined as the ratio between the minor and the major radii of an oval hole, and the major hole's radius, *r*, are independent from other parameters.

3.2.1 Design Concept 1

Fig. 33 shows f vs. ε_R for three sets: Set 1) $\theta=40^{\circ}$, $\alpha=40^{\circ}$; Set 2) $\theta=40^{\circ}$, $\alpha=90^{\circ}$; and Set 3) $\theta=90^{\circ}$, $\alpha=140^{\circ}$. It can be seen that ε_R is not linearly related to f; ε_R, in fact, exponentially increases as f decreases, such that when f=0.65, ε_R is *16.5* times larger than when $f=0.95$. It can be therefore deduced that f does not sensibly affect results on a potential optimal search related to either the fibre or hole orientation. Geometrical optimization analyses can therefore be performed for a fixed value of f. The independency of the optimum from f will be verified later in Section 5.4.1.

As far as the influence that the radius r has on the maximum strain, ε_R, Fig. 34 demonstrates that ε_R has a negative linear slope relation with the radius, r. Since the relationship is linear, this variable can be neglected in a geometrical optimization analysis.

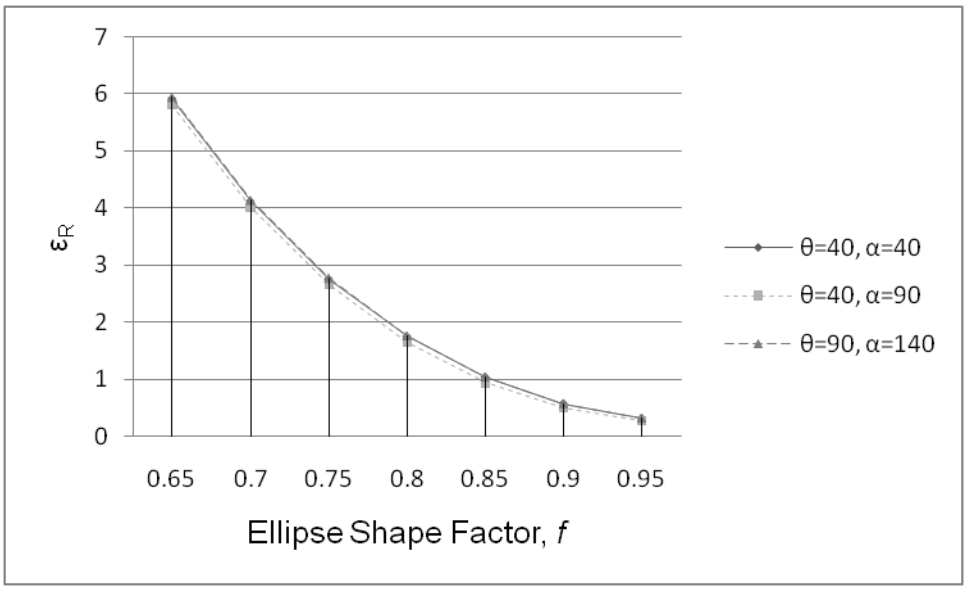

Fig. 33 $\varepsilon_R/\varepsilon_{Rm}$ at different *f* for three different sets of fibre direction, θ, and hole orientation, α (r=100μm).

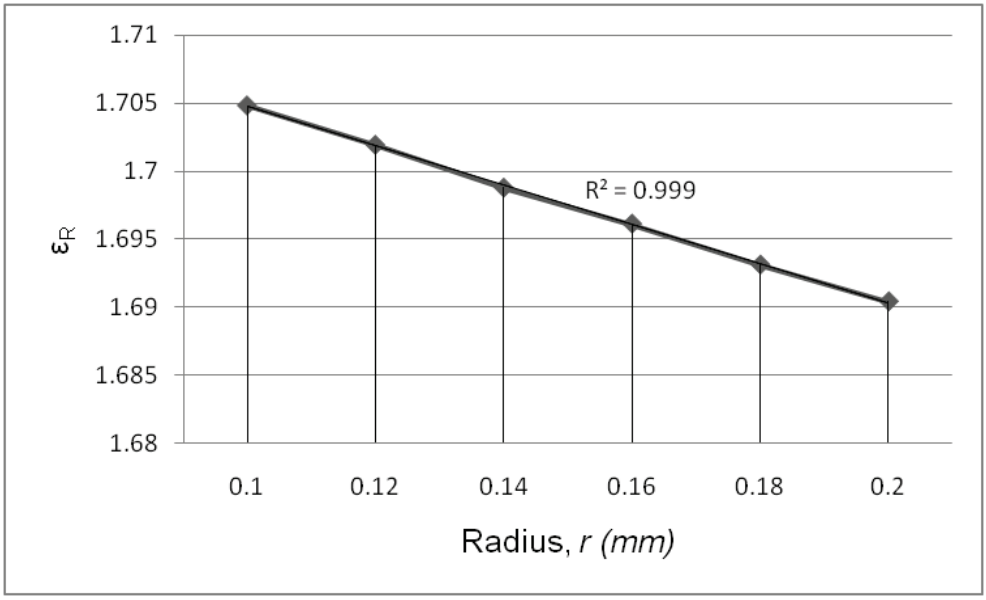

Fig. 34 *r* vs. ε_R in a shell with single hole under planar strain, ε_x=0.1%, while θ=0˚, α=0˚ and *f*=0.8.

3.2.2 Design Concept 2

f was studied for three configurations of θ and α_k: Set 1): $\theta=0^\circ$, $\alpha_k=0^\circ$; Set 2): $\theta=45^\circ$, $\alpha_k=0^\circ$; and Set 3): $\theta=0^\circ$, $\alpha_1=\alpha_4=0^\circ$, $\alpha_2=\alpha_3=45^\circ$. Fig. 35 illustrates *f* vs. ε_R for these three sets. ε_R rises exponentially when *f* decreases from *0.95* to *0.65*. It can therefore be deduced that *f* does not sensibly affect results on the optimal search related to either the fibre direction or holes orientations. Similarly, to the Design concept 1, geometrical optimization analyses can therefore be performed for a fixed value of *f*.

As far as the influence that the radius r has on the maximum strain, ε_R, Fig. 36 shows that ε_R has a negative linear slope relation with the radius, *r*. Similarly, to the Concept design 1, the parameter *r* can, therefore, be neglected during a geometrical optimization. The independency of the optimal from *f* will be verified later in Section 5.4.2.

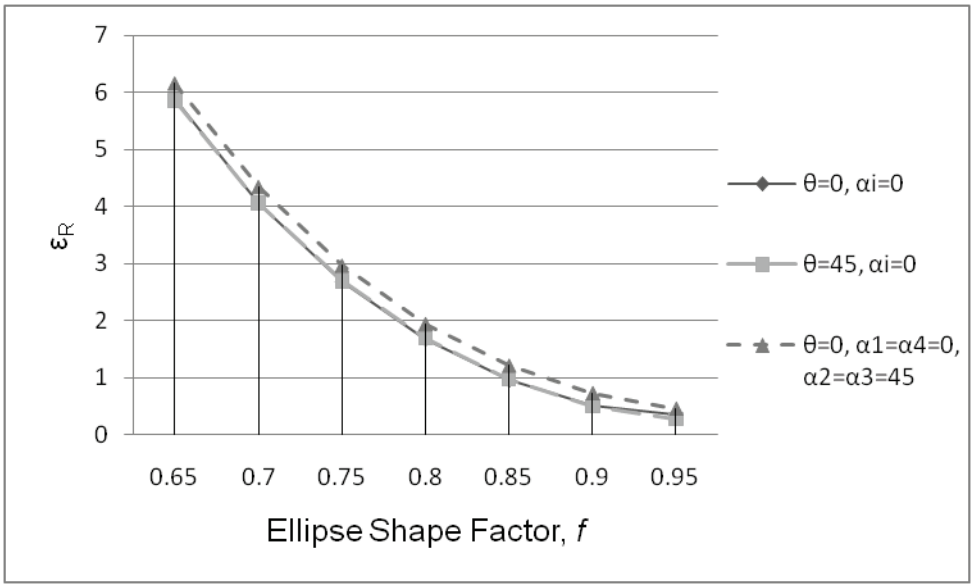

Fig. 35 ***f*** **vs.** ε_R **for three different sets of fibre direction,** θ**, and holes orientations,** α_k **(*r=100μm and h=300μm*).**

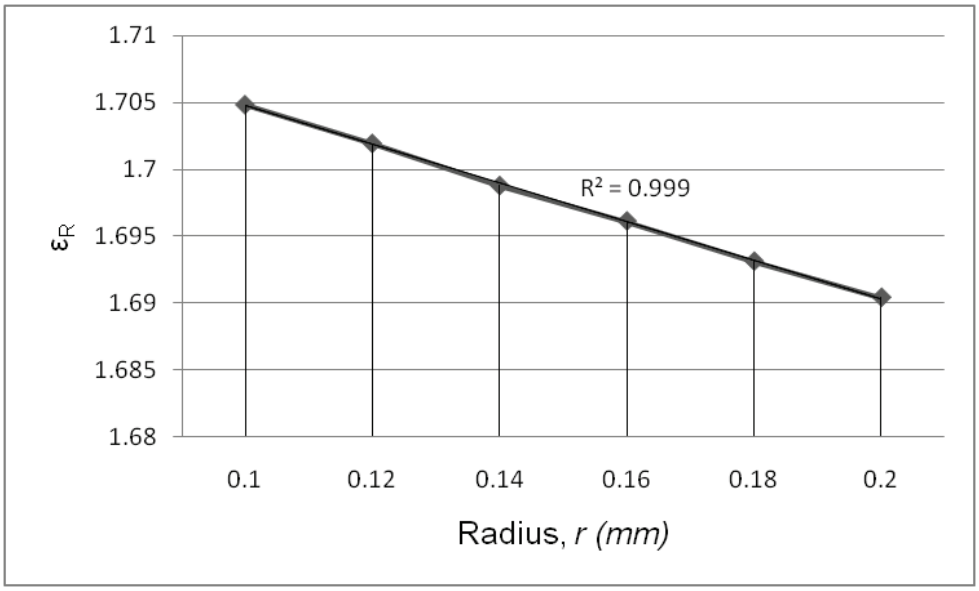

Fig. 36 ***r*** **vs.** ε_R **in a shell with single hole under planar strain,** ε_x***=0.1%*****, while** θ***=0˚,*** α_k***=0˚*****,** ***h=300μm*** **and** ***f=0.8.***

3.3 Influence of Hole(s) Orientation(s) and Fibre direction

In the previous sections, we concluded that material properties could be neglected in first approximation as they are independent from other parameters and/or are linearly related to the CS mechanical amplification effect. In addition, f does not sensibly affect results on the optimal search related to either the fibre direction or holes orientations, and ε_R has a linear relation with the radius, r, and therefore can both be neglected in this analysis. Values $f=0.8$, $r=100\mu m$, $h=300\mu m$ (if applicable) and constant values of material properties were therefore considered in the A-FEM analysis. Hole(s) orientation(s), α_k, and fibre direction, θ, were instead taken into account for A-FEM simulation, data modeling, and optimization. Simulations were performed by assuming a constant strain of the plate of $\varepsilon_x=0.1\%$.

3.3.1 Design Concept 1

An A-FEM database was generated for $0^\circ \le \theta \le 90^\circ$ and $0^\circ \le \alpha < 180^\circ$ by steps of 10° and $0.65 \le f \le 0.95$ by steps of 0.05. As mentioned above only the A-FEM simulation results for $f=0.8$ were considered in design concept 1.

Effect of α on ε_R depends on the direction of the fibres. It means the relation α makes with ε_R is a function of θ; therefore, its behaviour was explored at different direction of fibres. Fig. 37 shows α versus ε_R to its maximum, ε_{Rm}, for three fibre directions $\theta=0^\circ$, 40° and 90°, while $0^\circ \le \alpha < 180^\circ$ by steps of 10°. ε_{Rm} is the maximum ε_R, among the selected values of α and θ. When $\theta=0^\circ$, the maximum is at $\alpha=40^\circ$ and $\alpha=140^\circ$ and minimum occurs at $\alpha=90^\circ$. While θ is increasing from 0° to 45°, both the maximum and minimum start shifting to occur

at smaller values of *α.* When *θ=45˚*, the maximum takes place at *α=20˚* and *α=120˚* and minimum comes about at *α=70˚*. Then again, while *θ* is increasing from *45˚* to *90˚,* the optimums start to shift back to their initial point, where *θ=0˚.* The magnitudes of the maximum and minimum change, as well, while *θ* varies from *0˚* to *90˚*.

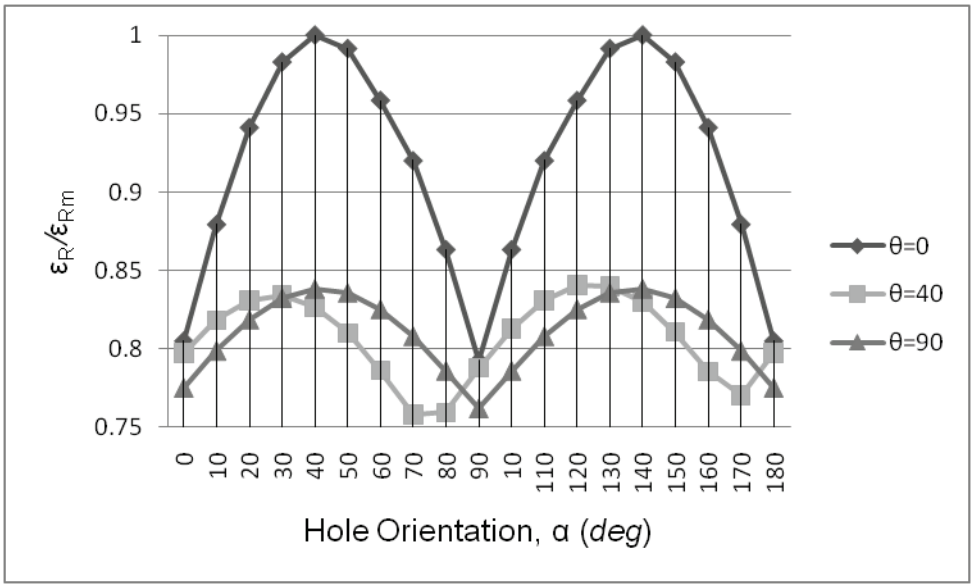

Fig. 37 *α* vs. $\varepsilon_R/\varepsilon_{Rm}$ in a shell with single hole under ε_x=0.1% for three fibre directions *θ=0˚, 40˚* and *90˚* (*f=0.8, r=100μm* and *εRm* is the maximum ε_R, among the selected values of *α* and *θ*).

Fig. 38 shows *θ* vs. $\varepsilon_R/\varepsilon_{Rm}$ for *α=30˚*, *α=40˚*, *α=50˚*, and *α=60˚*. ε_{Rm} is the maximum ε_R for each selected *α,* while *0˚≤θ≤90˚*. *θ* vs. $\varepsilon_R/\varepsilon_{Rm}$ does not represent correlated trend for different *α.* The pick always takes place at *θ=0˚* for all hole orientation.

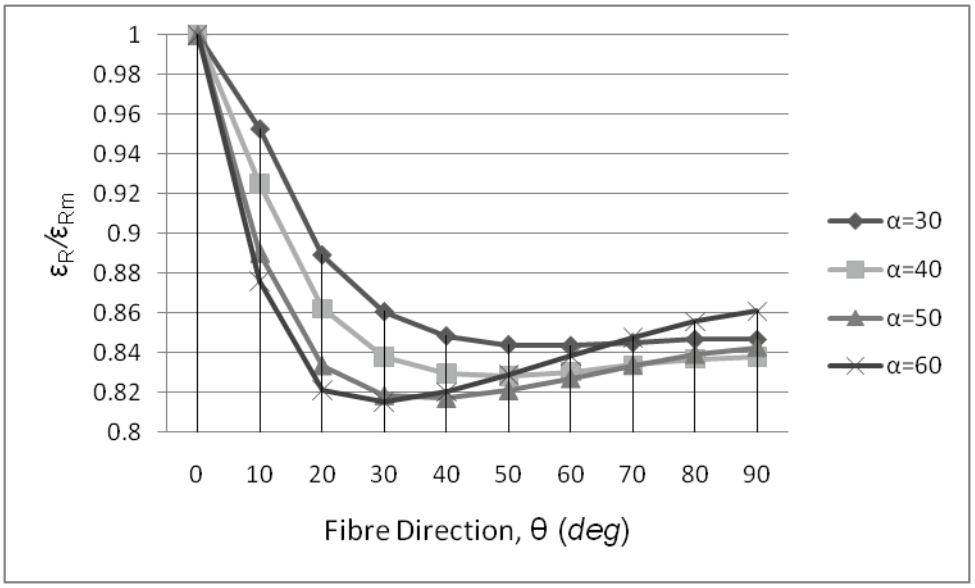

Fig. 38 *θ* vs. $\varepsilon_R/\varepsilon_{Rm}$ vs. in a shell with single hole under planar strain, ε_x*=0.1%*, for diffident hole orientations, *α=30˚, 40˚, 50˚* and *60˚* (*f=0.8, r=100μm and* ε_{Rm} is the maximum ε_R for each selected *α,* while *0˚≤θ≤90˚*).

Table 1 shows ε_{Rm} for each *0˚≤θ≤90˚* by steps of *10˚,* where *α* varies from *0˚* to *180˚* by steps of *10˚*. Table 1 was created from the database generated through A-FEM simulation, for *f=0.8*. In this table, it can be seen that for ε_{Rm} at *θ=0˚* and *90˚* two hole orientations are allocated each. This is true since *α =40˚* and *140˚* are two symmetrical hole orientations when fibre direction are horizontal and vertical.

Table 1 ε_{Rm} for different fibre directions from the A-FEM simulation while *r=100μm* and *f=0.8*.

θ (deg)	ε_{Rm}	*α (deg)*
0	*2.1170*	*40, 140*
10	*1.9456*	*40*
20	*1.8871*	*20*
30	*1.8155*	*20*
40	*1.7796*	*20*
50	*1.7678*	*30*
60	*1.7657*	*30*
70	*1.7678*	*30*
80	*1.7720*	*40*
90	*1.7742*	*40,140*

3.3.2 Design Concept 2

Four variables α_1, α_2, α_3 and α_4 were used to define the independent orientations of the holes. In order to reduce the computational time of the simulations, a fixed value of the variable *h* was considered; this implies that the four holes were in a *2 by 2* matrix in which the distances between its cells are equal and change dependently (see Fig. 21).

An A-FEM database was generated for $0^\circ \leq \theta < 180^\circ$ by steps of 15° and $0^\circ \leq \alpha_k < 180^\circ$ by steps of 20°. The symmetrical configurations of holes and fibres were neglected to reduce the number of simulation iterations. Fig. 38 shows all three symmetrical configuration and their original for a particular holes orientations and fibre direction. The symmetrical configurations of an arrangement of fibre direction and holes orientations were identified by rotating the shell once at a time as,

- 180° about its y-axis (Fig. 38(b))

- *180˚* about its *x*-axis (Fig. 38(c))
- *180˚* about its x-axis, and then *180˚* about its *y-axis,* or vice versa (Fig. 38(d))

and looking normal to the shell from the same direction. The observed direction of fibres and orientations of the holes is considered as a symmetrical configuration of the original configuration. Fig. 38(a) is the original configuration of hole orientations and fibre direction.

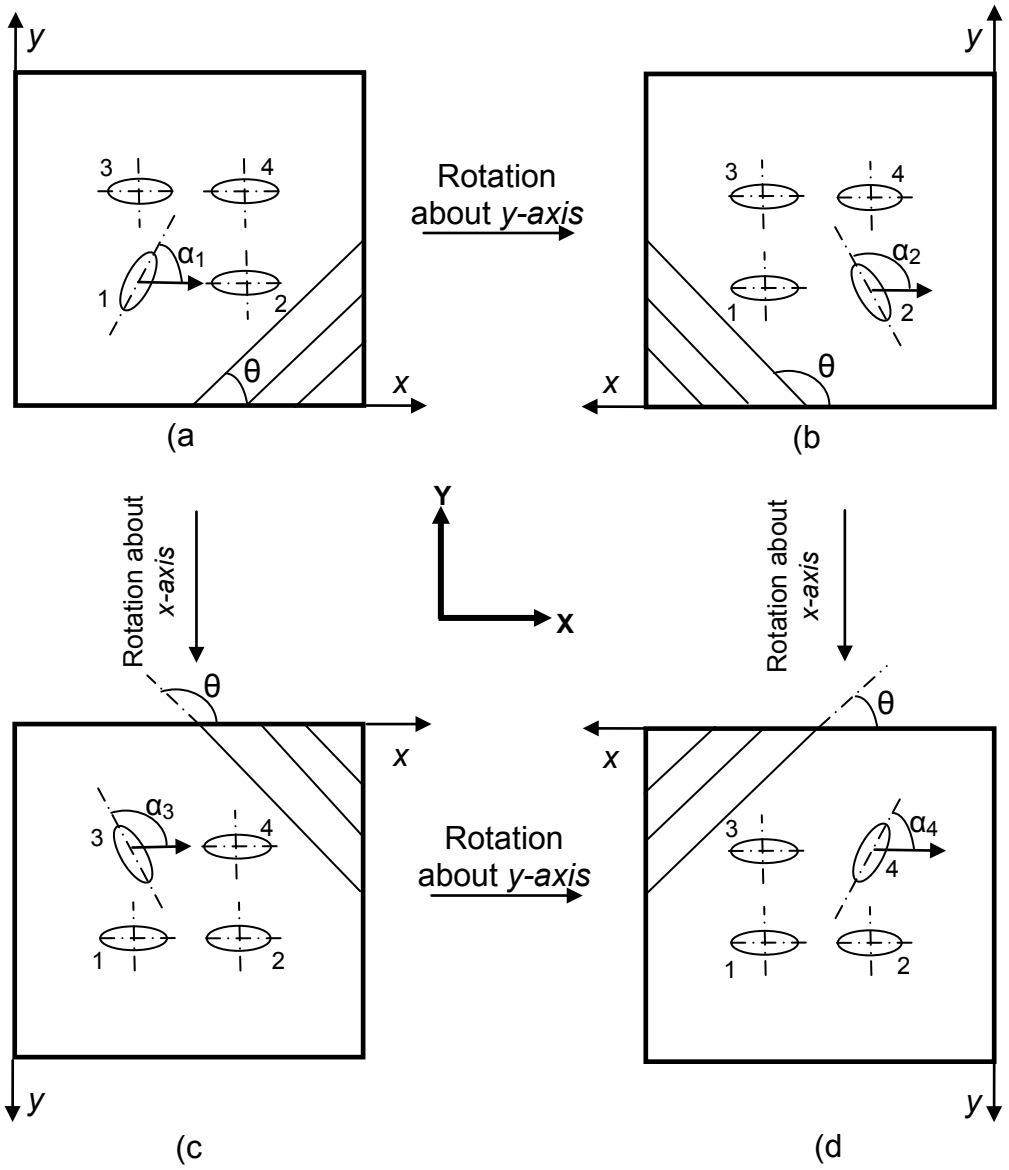

Fig. 39 Symmetrical configurations of holes and fibres in a shell with four holes in arrays of two. (a) is the original configuration and (b), (c) and (d) are the symmetrical configurations. Y and X are the global axes and *x* and *y* are the local axes of the shell.

An explicit relation for the effect of neither fibre direction, θ, nor holes orientations, α_k, with ε_R could be attained. Although the effect of h exemplifies a nonlinear behaviour as shown in Fig. 40, its effect on ε_R is negligible. This variable was therefore not considered in the A-FEM simulations

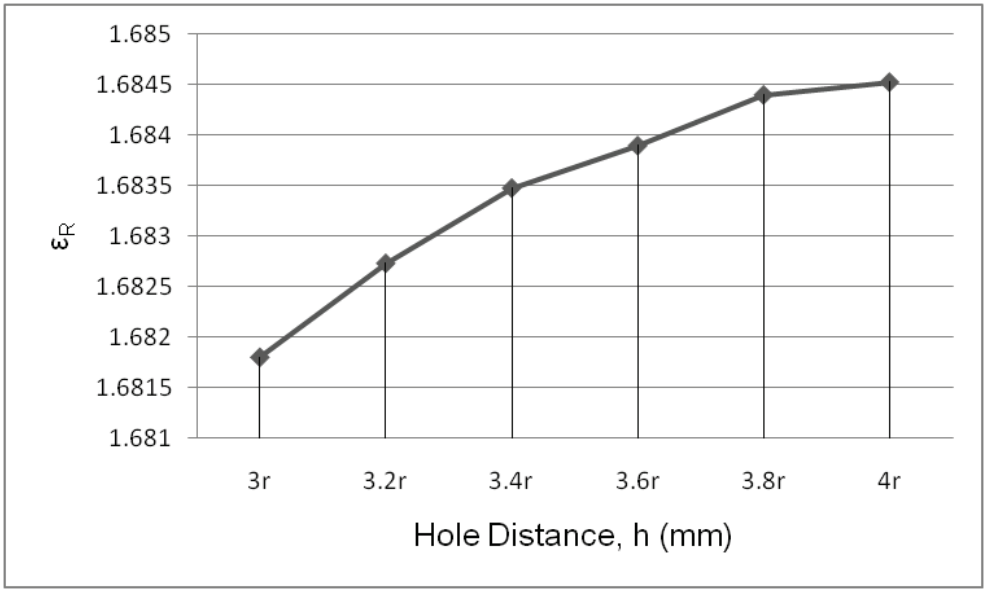

Fig. 40 *h* vs. ε_R while $\theta=0^\circ$, $\alpha_k=0^\circ$, r=100μm and f=0.8.

Based on the generated A-FEM database, Table 2 reports ε_{Rm} for each $0^\circ \leq \theta < 180^\circ$ by steps of 15°, where α_k vary from 0° to 180° by steps of 20°.

Table 2 ε_{Rm} for different fibre directions from A-FEM data, while *r=100μm, h=300μm* and *f=0.8.*

θ (deg)	ε_{Rm}	α_1 (deg)	α_2 (deg)	α_3 (deg)	α_4 (deg)
0	1.9634	0	60	20	20
		20	20	60	0
		120	0	160	160
		160	160	0	120
15	1.9902	0	60	0	40
		40	0	60	0
165		0	140	0	120
		120	0	140	0
30	1.8524	0	60	0	40
		40	0	60	0
150		0	140	0	120
		120	0	140	0
45	1.7856	0	60	160	60
		60	160	60	0
135		20	120	0	120
		120	0	120	20
60	1.7634	20	60	0	40
		40	0	60	20
120		0	140	160	120
		120	160	140	0
75	1.7540	20	60	0	40
		40	0	60	20
105		120	160	140	0
		0	140	160	120
90	1.7569	0	140	140	120
		120	140	140	0
		40	0	60	40
		40	60	0	40

3.4 Comparison between the Two Investigated Design Concepts

The strain amplification performance in design concept 1 was compared with design concept 2. Two different scenarios were considered:

- First, the holes' radii in both concept designs are identical. Fig. 41 gives a picture of this comparison. Fig. 41 also compares the effect of *r*

in concept design 2 for two cases of 1) constant holes' centres distance (*h=450μm*), and 2) holes' centres distance as a function of *r* (*h=3r*).

- Second, the volume of material that was removed from the shell, in both design concepts, to obtain the hole(s) are equal. Since the thicknesses of the shell (*t=100μm*) are the same in both design concepts, then the surface area of deducted holes in both design concepts are equal. Fig. 42 gives a snapshot of the hole(s) deducted area vs. ε_R for design concept 1 and design concept 2 when: 1) *h=180μm,* 2) h=*3.5r, 3) h=4r* and *4) h=4.5r*.

Fig. 43 - Fig. 46 compare the material properties E_x, E_y, G_{xy} *and* ν_{xy} Influence on ε_R in design concept 1 and ε_R in design concept 2. It can be seen that concept design 1 always has a better amplification performance than design concept 2.

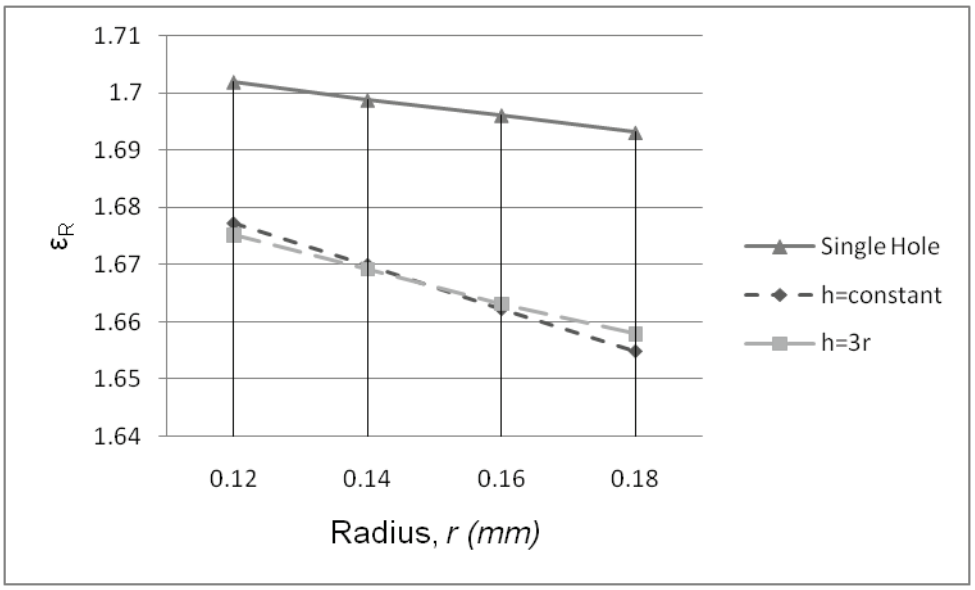

Fig. 41 *r* vs. ε_R in both design concepts while $\theta=0^\circ$, $\alpha=\alpha_k=0^\circ$, and *f=0.8*.

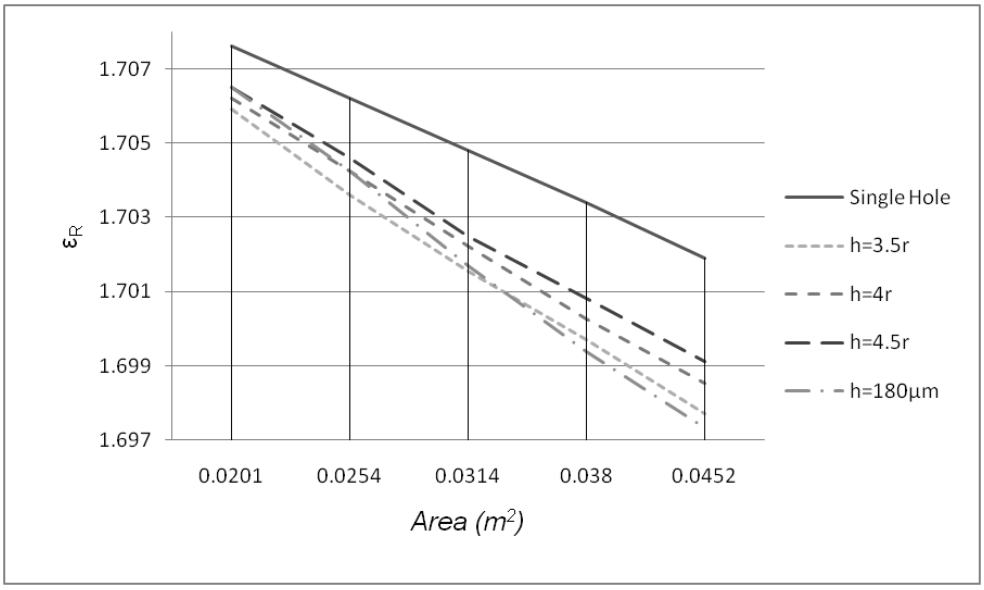

Fig. 42 Area of deducted hole(s) vs. ε_R in design concept 1 and design concept 2 while *h=180μm*, *h=3.5r*, *h=4r* and *h=4.5r*. $\theta=0^\circ$, $\alpha=\alpha_k=0^\circ$, and *f=0.8*.

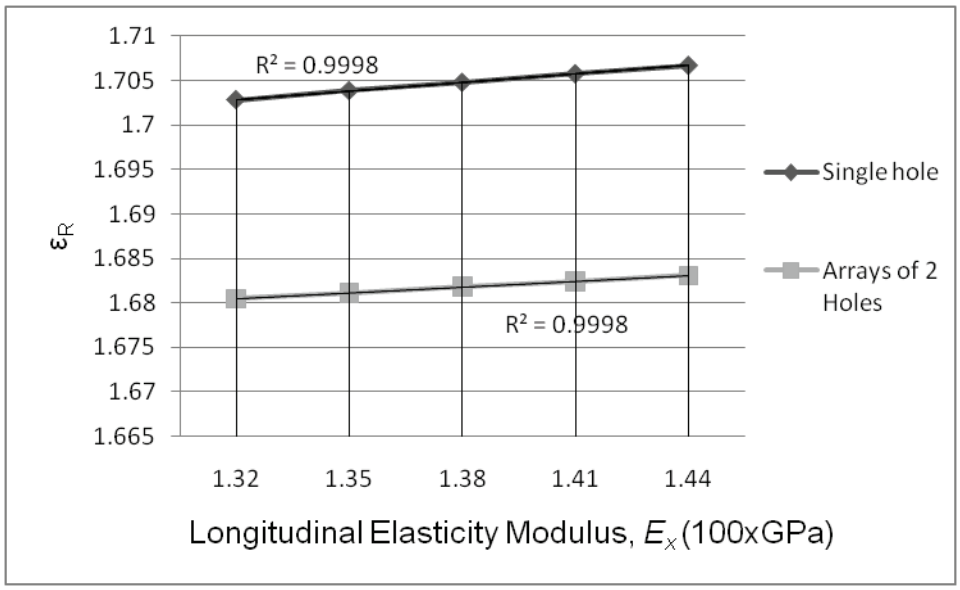

Fig. 43 E_x vs. ε_R while $\theta=0^\circ$, $\alpha=\alpha_k=0^\circ$, $r=100\mu m$, $h=300\mu m$ and $f=0.8$. The black line is for a shell with single holes and the grey line is for a shell with array of two holes.

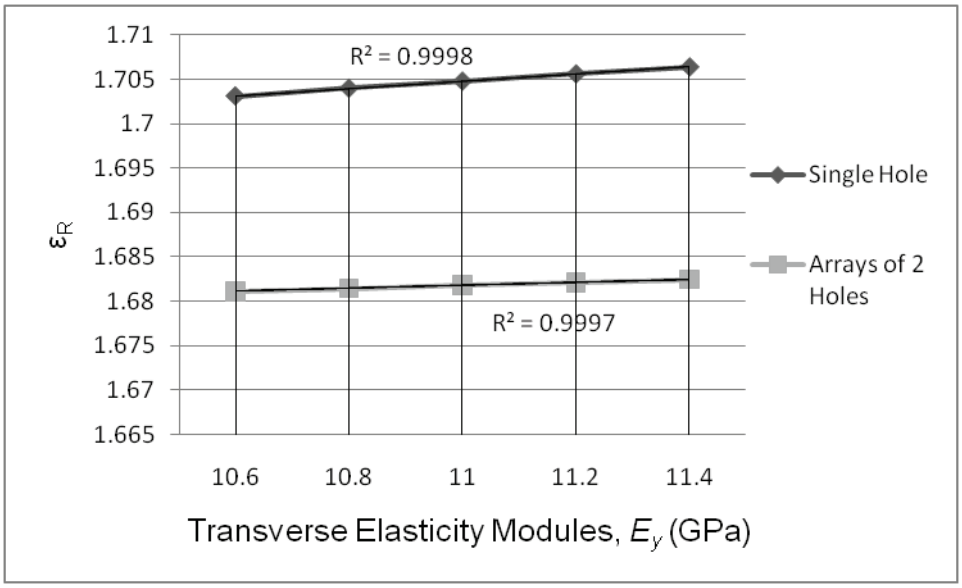

Fig. 44 E_y vs. ε_R while $\theta=0^\circ$, $\alpha=\alpha_k=0^\circ$, $r=100\mu m$, $h=300\mu m$ and $f=0.8$. The black line is for a shell with single holes and the grey line is for a shell with array of two holes.

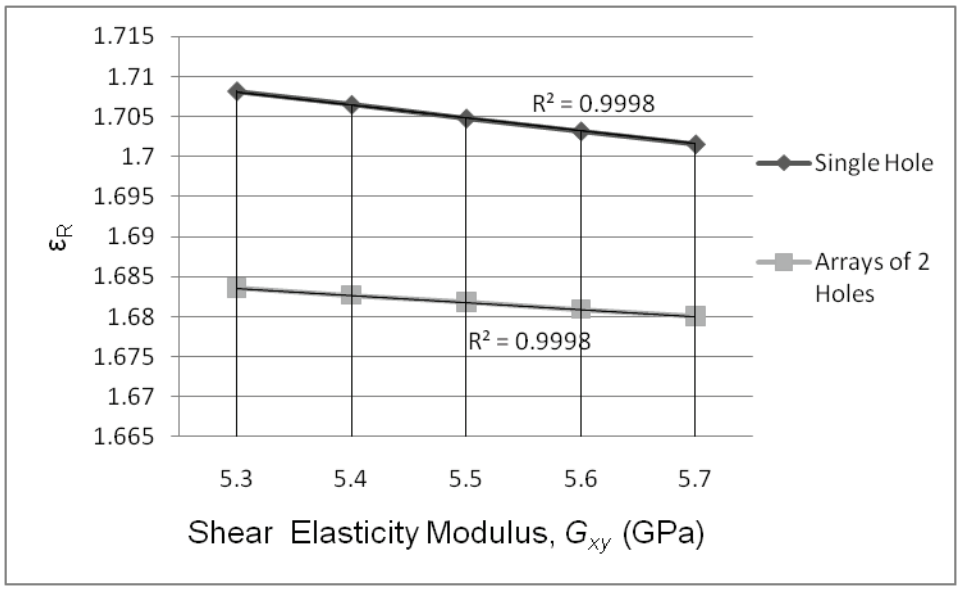

Fig. 45 G_{xy} vs. ε_R while $\theta=0^\circ$, $\alpha=\alpha_k=0^\circ$, $r=100\mu m$, $h=300\mu m$ and $f=0.8$. The black line is for a shell with single holes and the grey line is for a shell with array of two holes.

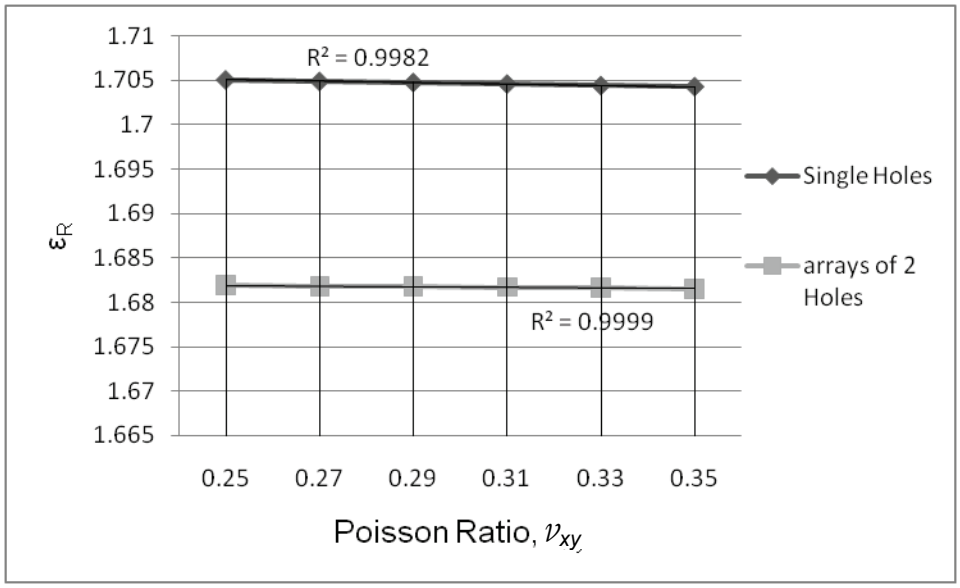

Fig. 46 ν_{xy} vs. ε_R, while $\theta=0^\circ$, $\alpha=\alpha_k=0^\circ$, $r=100\mu m$, $h=300\mu m$ and $f=0.8$. The black line is for a shell with single holes and the grey line is for a shell with array of two holes.

So far, all the comparison and analysis were done considering $\varepsilon_x=0.1\%$. h vs. ε_R is illustrated for $\varepsilon_x=0.1\%$ and $\varepsilon_x=0.095\%$ in Fig. 47. When $\varepsilon_x=0.095\%$, ε_R is 5% less than when $\varepsilon_x=0.1\%$. It was observed that ε_R has linear relation with ε_x. It

should be noted that, although simulations were performed by considering a deformation of the shell ε_x equal to *0.1%,* the obtained results still hold true for different deformations as long as the conditions of small deformations and linear material properties are met. Obtained results also do not change for scaled geometrical configurations. Assuming a fixed value of the strain (e.g. ε_x equal to *0.1%*) for further investigating the problem, was therefore considered to be a suitable choice.

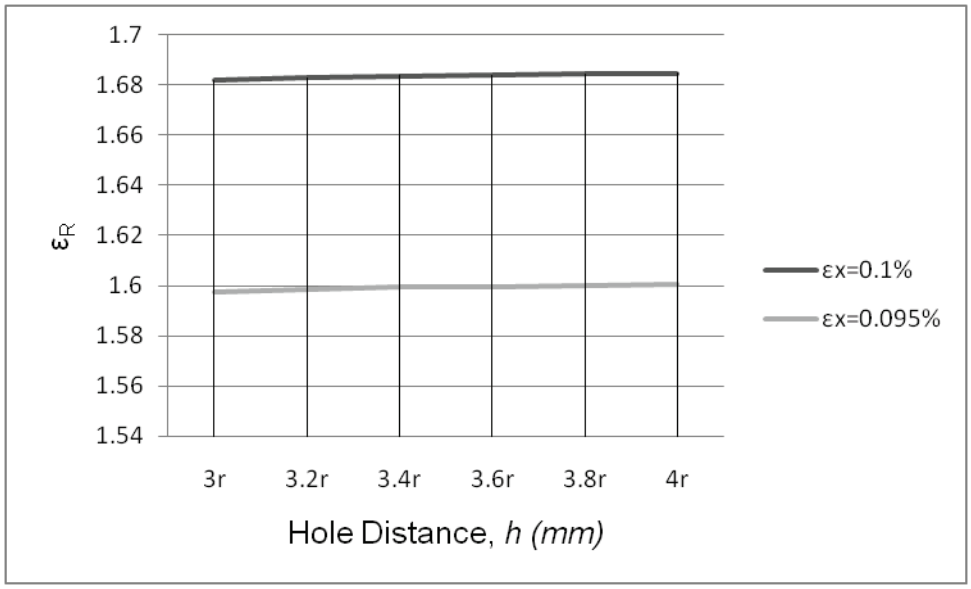

Fig. 47 *h* vs. ε_R while $\theta=0^\circ$, $\alpha_k=0^\circ$, *r=100μm*, and *f=0.8* (ε_x=*0.1*% and 0.095%)

4- CHAPTER FOUR: DATA MODELING WITH ARTIFICIAL NEURAL NETWORKS (ANN)

The first objective of the thesis, namely assessing which parameters affect the most the CS mechanical amplification characteristics, was addressed in the previous chapter. In this Chapter 4, focus is on the second objective of the thesis, namely identifying an equation which represents the strain of the holes as a function of the CS geometrical parameters for a given deformation of the plate in which the CS is. In order to achieve this goal, which enables calculating ε_R for any arbitrary selected design variables' values without running FEM simulations, an ANN model was built. This ANN model was created by using data of the database previously obtained through A-FEM simulations.

ANN approximate a model to the input and output data by using several parallel and serial units called neurons. ANN modeling is a very flexible method for tracing the data and recognizing the relation between the output(s) and input(s) [10].

This model can be also used to identify the optimum design without using FEM analysis, as presented in the following section. Optimization based on FEM analysis is more expensive than optimization based on a mathematical model. Thus, the calculation time diminishes if a precise data model is substituted with FEM analysis.

4.1 Multilayer Perceptron (MLP) Neural Network

One of the most applicable networks for nonlinear function approximation is Multilayer perceptron (MLP) neural network which has numerous nonlinear units in a single layer. The MLP neural network was therefore employed in the ANN data modeling in this work. MLP performs as a universal function estimator [10, 13, 14]. The structure of MLP network is formed with three layers:

- Input layer,
- Hidden layer(s)
- Output layer

These layers are connected serially in this order (see Fig. 47). Each connection has a corresponding weight/bias factor. It means all signals, which go through, get a weigh/bias factor. Based on the problem, the network may have one or more hidden layers. An appropriate learning algorithm should be employed to estimate the weight and bias factors. This algorithm helps to re-assign and adjust the connection weights between the neurons [10].

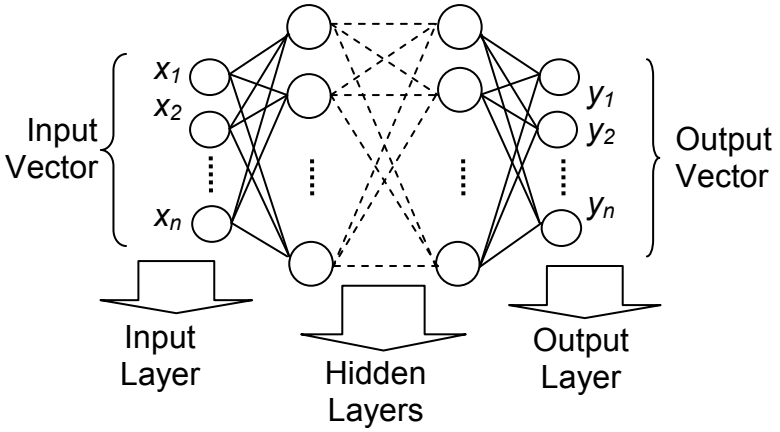

Fig. 48 Schematic representation of the MLP

One of the most effective and fastest learning algorithms is Levenberg–Marquardt algorithm which is a modified version of Gauss-Newton method [10, 16]. Levenberg-Marquardt algorithm was used in order to train the MLP for this study. The following recursive equation expresses the Levenberg–Marquardt update:

$$M(k+1) = M(k) - [J_k^T J_k + \mu_k I]^{-1} J_k^T e(k) \quad (7)$$

In this equation vector $\vec{M}$ comprises two parameters w_{il}^{mn} and b_i^{mn}. *J* represents the Jacobean matrix with elements $j_{il} = \frac{\partial e_i}{\partial m_l}$. w_{il}^{mn} is the *i*-th row and *l*-th column of the *m*-th layer and *n*-th output of the neural network weight matrix. b_i^{mn} is the *i*-th row of basis matrix of m-th layer and n-th output of the

neural network. The error of network's gain and the desired output appears in the equation as e. μ_k is the step length [16].

For this problem, one hidden layer was implemented in the network. Hyperbolic tangent sigmoid transfer function was used in the hidden layer as,

$$tansig(n) = \frac{2}{1+exp(-2.n)} - 1 \quad (8)$$

and linear transfer function was used in the output layer that,

$$purelin(n) = n \quad (9)$$

To increase the performance of the network training process and avoid overfitting, an early stopping method was employed. For this reason, the input vectors and target vectors were randomly divided into three sets, as follows:

Training data set: *60%* of data of the database was used for training network.

Validation data set: *20%* of data of the database was used for network validation so that the network could generalize and stop the training before overfitting occurs.

Test data set: *20%* of data of the database was used to test the network and assess its performance and accuracy.

In the early stopping method, the network is trained by using the *training data*. On the other hand, while training is in the process, with *validation data* the network monitors its performance. At early stages of training, the validation error begins to decrease to some extent. Then eventually the validation error starts to increase again. The network is stopped when the validation error reaches the minimum error. Finally, the *test data* subset is used to evaluate the trained network. For a higher network training performance the input vector should be normalized between [-1 1]. [10]

4.2 Data Model Function Formulation

The parameters, P, which were considered in this investigation, are:

- The hole(s) orientation(s), α_k (k=1, 2, 3 and 4 in design concept 2; k is neglected in design concept 1, as just one hole exists)
- The fibre direction, θ
- Ellipse shape factor, f.

As previously discussed in Chapter Three, ellipse shape factor, f, was independent from the other parameters in both design concepts. However, given the lower number of variables in design concepts 1, f also was considered for the simulation.

Running MLP networks with *P* as the input vector, first the hidden layer transfer function (8) is applied to *P* and next the outcome of hidden layer is imported to the output layer transfer function (9). Therefore, the general form of estimated function, also known as data model in this thesis, is formulated as,

$$\varepsilon_R(P) = W_O \times tansig(W_{\mathrm{H}} \times P + B_{\mathrm{H}}) + B_{\mathrm{O}} \tag{10}$$

Weight and bias factors in the hidden layer are,

$$W_{\mathrm{H}} = \begin{bmatrix} w_{\mathrm{H}}^{11} & \cdots & w_{\mathrm{H}}^{1n} \\ \vdots & \ddots & \vdots \\ w_{\mathrm{H}}^{m1} & \cdots & w_{\mathrm{H}}^{mn} \end{bmatrix}_{m\times n} ;\ B_{\mathrm{H}} = \begin{bmatrix} b_{\mathrm{H}}^{1} \\ \vdots \\ b_{\mathrm{H}}^{m} \end{bmatrix}_{m\times 1} \tag{11}$$

And weight and bias factors in the output layer are,

$$W_{\mathrm{O}} = [w_{\mathrm{O}}^{1} \quad \cdots \quad w_{\mathrm{O}}^{m}]_{1\times m};\ B_{\mathrm{O}} = \overline{b_{\mathrm{O}}} \tag{12}$$

where *n* is input vector size (*n=3* in concept design 1 and *n=5* in concept design 2) and *m* is the number of neurons. W_0 and W_H are the two weight matrices respectively associated to the output and hidden layers. B_0 and B_H are the bias factors respectively for the output and hidden layers, where B_0 is a scalar and B_H is a vector.

The expanded general form of estimated function (10) has the form of,

$$\varepsilon_R(p_1, p_2, \dots, p_n) = \sum_{l=1}^{m} w_{\mathrm{O}}^{l} \left[\frac{2}{1+e^{-2\left(w_{\mathrm{H}}^{1,l} p_1 + w_{\mathrm{H}}^{2,l} p_2 + \cdots + w_{\mathrm{H}}^{n,l} p_n + b_{\mathrm{H}}^{l}\right)}} - 1 \right] + b_{\mathrm{O}} \qquad (13)$$

This data model can be a substitute for the A-FEM numerical simulation, which has high time complexity. This data model is used to find the optimum configuration of design variables that yields maximum ε_R.

4.3 ANN Results Accuracy

ANN with *40* and *60* neurons were employed for, respectively, design concepts 1 and 2, such that two data models were generated. The mean square error (MSE) of these two data models and the FEM numerical simulation were, correspondingly, *1.04e-4.*and *3.20e-4*. The weight and bias factors for both design concepts are presented in Appendix C. The obtained equation fulfills the second objective of the thesis.

5- CHAPTER FIVE: OPTIMIZATION

This Chapter 5 focuses on the third objective of this thesis, namely obtaining an optimal configuration of the holes to maximize strain for a fixed deformation of the substrate.

Equation (10) is continuous and can conveniently be used to compute ε_R for any arbitrary chosen design variables' values and is also suitable for design optimization. Equation (10) was therefore used to fulfill the third objective of this thesis. In this work, the optimum CS configuration is represented by the set of the design variables yielding the optimum ε_R ($\varepsilon_{R,opt}$) in the whole design space. As it was mentioned in Chapter 3, some of the design variables do not sensibly affect the optimum. Thus, the optimizations for design concepts 1 and 2 were done based on the only design variables α_k and θ. The optimum configurations investigated in this chapter for both design concepts are verified with FEM simulations in the neighborhood of the obtained optima.

5.1 Mode Pursuing Sampling (MPS) Optimization Toolbox

Mode Perusing Sampling was used to find the optimum of the data model. MPS is a metamodeling based design optimization method [17]. Its core is based on a computationally simple model which approximates the original expensive model by sampling within the design space and performing model fitting for a

selected model type [17]. The optimization, then, is performed on the fitted model [18]. Both Genetic Algorithm (GA) and MPS were used for optimization purpose for design concept 1. MPS performed better, as the optimum was narrowed down considerably faster with MPS. Besides, the MPS result was almost the same in every rerun, whereas the GA outcome varied for each single run. The best result among the several runs with GA was considered.

In order to approach the optimum faster, MPS statically generates more sample points near the optimum (mode). After each step of sampling, a more accurate function is evaluated. MPS does not fail to keep covering the whole design space. The mode shifts to the newly found optimum and consequently more sample points are generated around the optimum. If this point is close to the global optimum more sample points keep being generated in a small region around that optimum. Reaching a maximum number of function evaluations is the basis to stop sampling. If the objective function becomes relatively flat close to the global optimum then the speed of converging to the global optimum decreases. Therefore, the likelihood of reaching global optimum gets lower. In order to prevent reduction in the speed of convergence, MPS provides an intelligent method based on regression [17]. In the small relatively flat region of the current optimum, which contains the global optimum, a quadratic model is fitted to the sample points. This quadratic function contains the global optimum which can be easily achieved without evaluation of the expensive function [17].

5.2 Results for Design Concept 1

The data model optimum ($\varepsilon_{R,opt}$) was found, with GA, to be $\varepsilon_{R,opt}$ *=2.11683* for θ_{opt}*=0.0128˚* and α_{opt}*=45.0539˚*; ε_R found with FEM simulation for this optimum configuration was *2.11749.* With MPS, the data model optimum was, $\varepsilon_{R,opt}$ *=2.11769* for θ_{opt}*=0.0014˚* and α_{opt}*=45.0006˚*. ε_R found with FEM simulation for this configuration was *2.11751*. Table 1 was regenerated with GA and data model and to form Table 3. Table 1 was also redone with MPS based on data model and illustrated in Table 4; ε_{Rm} in Table 1, which was investigated from the A-FEM database, was substituted with $\varepsilon_{R,opt}$, which is the optimum found through GA and MPS. $\varepsilon_{R,opt}$ was investigated for *0˚≤θ≤90˚* by steps of *10˚,* where *α* varies from *0˚ to 180˚*, continuously.

Table 3 Optimum orientations for different fibre directions based on the data model with using GA (*r=100μm*, and *f=0.8*)

θ (deg)	$\varepsilon_{R,opt}$	*α (deg)*
0	*2.1168*	*45.0502*
10	*1.9967*	*27.7856*
20	*1.8735*	*22.5747*
30	*1.8342*	*21.4687*
40	*1.8612*	*23.8745*
50	*1.7762*	*32.4587*
60	*1.6913*	*34.9474*
70	*1.7732*	*43.4634*
80	*1.7851*	*44.4763*
90	*1.7807*	*44.8221*

Table 4 Optimum orientations for different fibre directions based on the data model with using MPS (*r=100μm*, and *f=0.8*)

θ (deg)	$\varepsilon_{R,opt}$	α (deg)
0	2.1177	45.0000
10	1.9980	28.0332
20	1.8923	22.4112
30	1.8253	21.8386
40	1.7828	24.0989
50	1.7739	32.5749
60	1.7697	34.7000
70	1.7720	43.1220
80	1.7734	44.3146
90	1.7795	44.7946

5.3 Results for Design Concept 2

Using MPS and the data model, the optimum value of ε_R was obtained $\varepsilon_{R,opt} = 2.00020$ and the following optimal parameters P_{opt} were identified: $\theta_{opt}=14.7^{\circ}$, $\alpha_{1,opt}=1.5^{\circ}$, $\alpha_{2,opt}=57.2^{\circ}$, $\alpha_{3,opt}=1.5^{\circ}$, and $\alpha_{4,opt}=46.6^{\circ}$. ε_R found with FEM simulation for this optimum configuration was *2.00102*. Table 3 was regenerated with MPS based on data model and illustrated in Table 5; ε_{Rm} in Table 3, which was investigated from the A-FEM database, was substituted with $\varepsilon_{R,opt}$, which is the optimum found through MPS. $\varepsilon_{R,opt}$ is investigated for each $0^{\circ}\leq\theta<180^{\circ}$ by steps of 15°, where α_k vary from 0° to 180°, continuously.

Table 5 Optimum orientations for different fibre directions base on data model using MPS. (*r*=100μm, *h*=300*μm*, and *f=0.8*)

θ	$\varepsilon_{R,opt}$	α_1	α_2	α_3	α_4
0	*1.9698*	*5.4*	*64.5*	*26.7*	*23.5*
		23.3	*27.1*	*64.0*	*5.1*
		135.2	*175.8*	*157.4*	*153.8*
		152.9	*157.6*	*174.6*	*135.0*
15	*1.9999*	*1.2*	*56.9*	*1.6*	*46.9*
		46.3	*1.4*	*55.5*	*0.9*
30	*1.8534*	*2.0*	*51.4*	*3.9*	*44.3*
		45.0	*3.4*	*51.2*	*1.347*
45	*1.7852*	*0.5*	*66.8*	*161.8*	*57.5*
		58.8	*160.9*	*64.3*	*2.7*
60	*1.7659*	*29.7*	*57.8*	*2.5*	*40.3*
		41.3	*2.8*	*58.3*	*29.7*
75	*1.7548*	*27.2*	*60.0*	*5.1*	*39.1*
		39.4	*5.9*	*60.5*	*27.9*
90	*1.7572*	*178.5*	*143.6*	*147.4*	*127.1*
		126.6	*146.7*	*144.1*	*1.1*
		36.9	*1.3*	*63.4*	*31.8*
		32.2	*61.5*	*0.9*	*37.0*
105	*1.7541*	*4.3*	*141.4*	*153.1*	*10.7*
		120.7	*152.7*	*141.2*	*4.0*
120	*1.7650*	*176.9*	*144.8*	*151.6*	*132.6*
		132.4	*150.8*	*145.0*	*177.2*
135	*1.7847*	*19.7*	*123.8*	*1.0*	*123.4*
		123.3	*0.8*	*123.9*	*20.2*
150	*1.8526*	*178.2*	*132.9*	*177.4*	*122.6*
		125.8	*177.3*	*132.7*	*177.6*
165	*1.9967*	*178.3*	*133.6*	*178.8*	*123.2*
		123.9	*177.7*	*134.2*	*178.5*

5.4 Results Validation with Sensitivity FEM Analysis

The optimal vector P_{opt}, which was identified by using (10) and MPS, was validated by performing additional FEM analyses, whose parameters were in the neighbourhood of P_{opt}.

5.4.1 Design Concept 1

ε_R was recomputed by using ANSYS close to the optimal values α_{opt} which was investigated with GA and MPS. FEM results for the hole orientation variation around its GA and MPS optimum values are illustrated, respectively in Fig. 49 and Fig. 50. A similar FEM validation analysis was also performed to assess if the identified angles θ_{opt} with GA and MPS were the correct optimal direction of the fibres. Fig. 51 and Fig. 52 outline the accuracy of the results which were obtained respectively by MPS and GA. It can be seen that both GA and MPS methods are appropriate to identify both the optimal orientation of the holes and fibre direction. However, the value $\varepsilon_{R,opt}$ identified with MPS is closer to the value computed with FEM in comparison to GA optimum estimation. MPS found the optimum faster than GA. Moreover, we had to run the simulation with GA several times to get to a better result; while, MPS almost every time merged to same value with a negligible error.

A similar FEM analysis was performed to assess the influence of the parameter *f* on α and θ. Fig. 53 and Fig. 54 show that α_{opt} and θ_{opt} do not change for different values of *f* in the range that was investigated, namely between *0.65* and *0.95.*

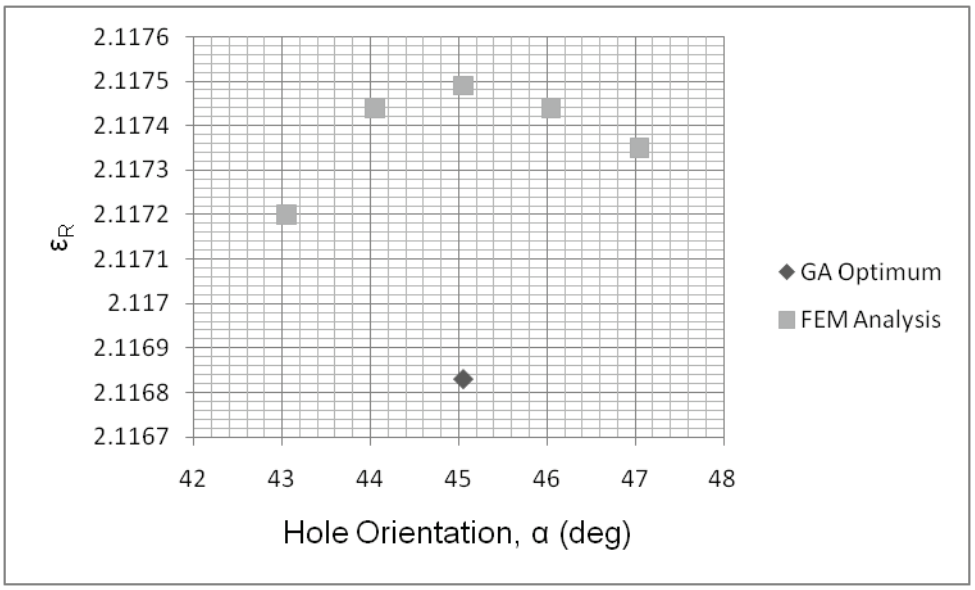

Fig. 49 Results of the FEM validation analysis performed in the neighbourhood of the optimal parameter α_{opt} identified by using GA and data model. *f=0.8* was used for this analysis.

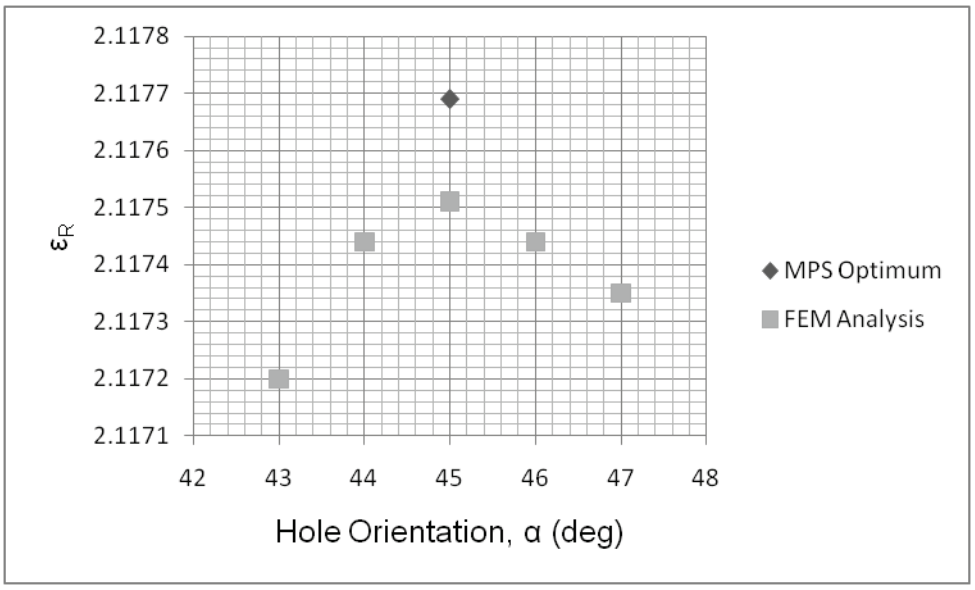

Fig. 50 Results of the FEM validation analysis performed in the neighbourhood of the optimal parameter α_{opt} identified by using MPS and data model. *f=0.8* was used for this analysis.

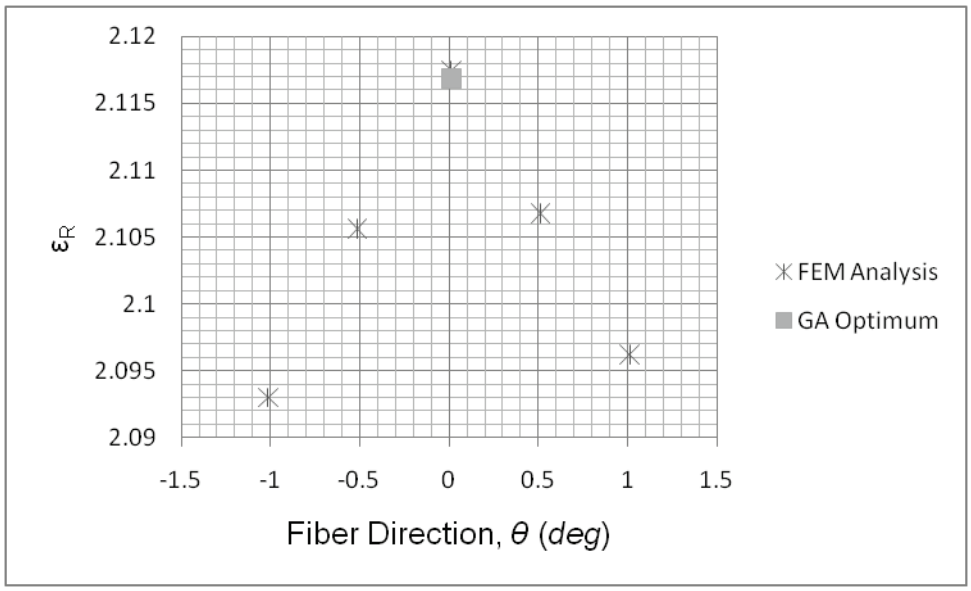

Fig. 51 Results of the FEM validation analysis performed in the neighbourhood of the optimal parameter θ_{opt} identified by using GA and data model. *f=0.8* was used for this analysis.

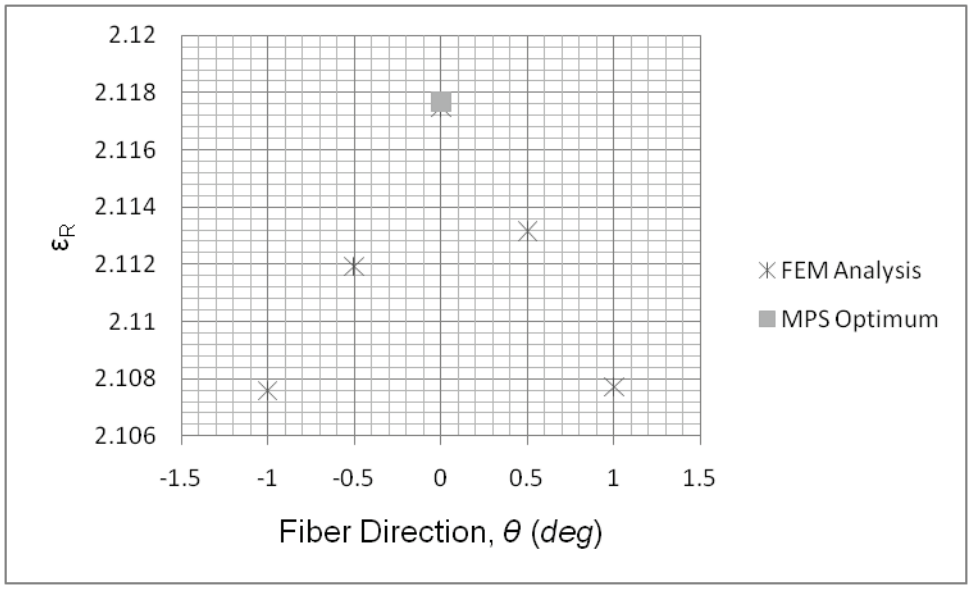

Fig. 52 Results of the FEM validation analysis performed in the neighbourhood of the optimal parameter θ_{opt} identified by using MPS and data model. *f=0.8* was used for this analysis.

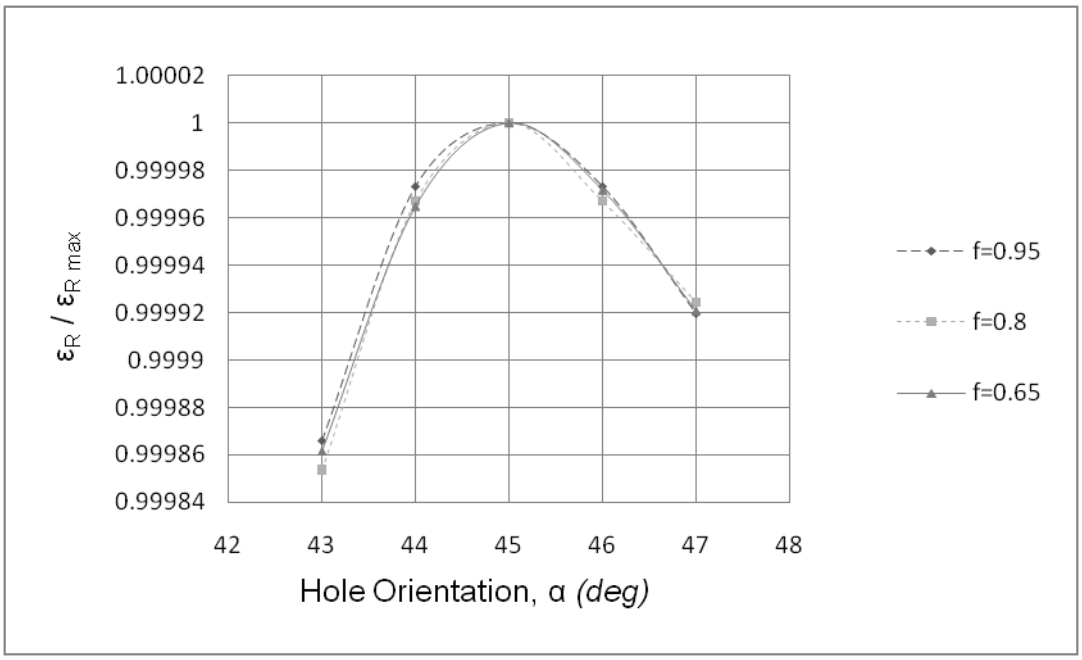

Fig. 53 FEM results in the neighbourhood of the optimal parameter α_{opt} identified by using MPS and data model. *f=0.65, 0.8* and *0.95* were used for this analysis.

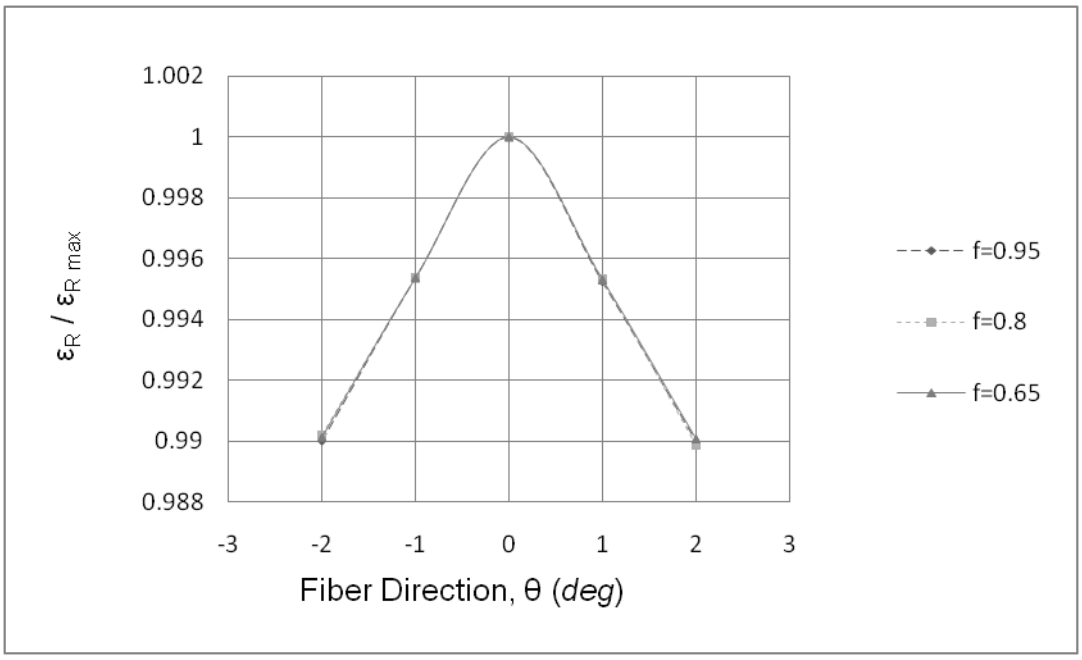

Fig. 54 FEM results in the neighbourhood of the optimal parameter θ_{opt} identified by using MPS and data model. *f=0.65, 0.8* and *0.95* were used for this analysis.

5.4.2 Design Concept 2

For validation reasons, the orientation of each hole was selected to be close to the optimal values $\alpha_{k,opt}$ and ε_R was subsequently recomputed by using ANSYS. Fig. 55 shows the results obtained by varying the orientation of one hole at a time. It can be seen that the method based on the data model and MPS was suitable for identifying the correct optimum orientations of the holes. The value $\varepsilon_{R,opt}$ computed by the FEM was slightly higher than the value which was estimated with MPS and data model. The error was however small, namely less than *0.05%* (see Fig. 55).

A similar FEM validation analysis was also performed to assess if the identified angle θ_{opt} was the correct optimal orientation of the fibres. Fig. 56 confirms the correctness of the results obtained by data model and MPS.

An additional FEM analysis was performed to assess if variations of the parameter *f* would change the identified optimal parameters $\alpha_{k,opt}$. Fig. 57 and Fig. 58 respectively show results obtained for *f=0.95* and *0.65*. These figures confirm that the identified parameters $\alpha_{k,opt}$ were still optimal for the different values of *f*.

A similar FEM analysis was performed to assess the influence of the parameter *f* on θ. Fig. 59 shows that θ_{opt} does not change for different values of *f* in the range that was investigated, namely between *0.65* and *0.95*.

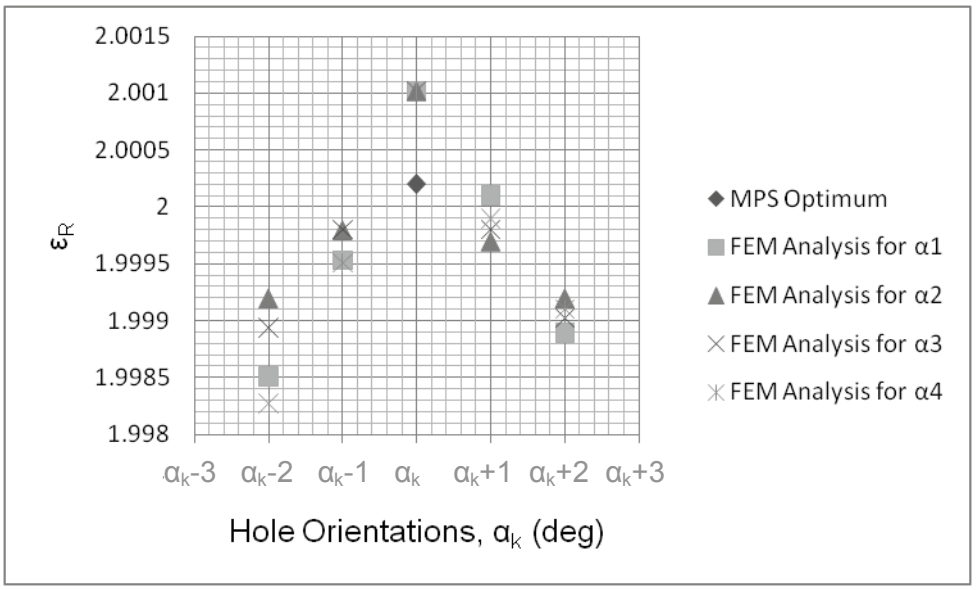

Fig. 55 Results of the FEM validation analysis performed in the neighbourhood of the optimal parameters $\alpha_{k,opt}$ identified by using MPS and data model. *f=0.8* was used for this analysis.

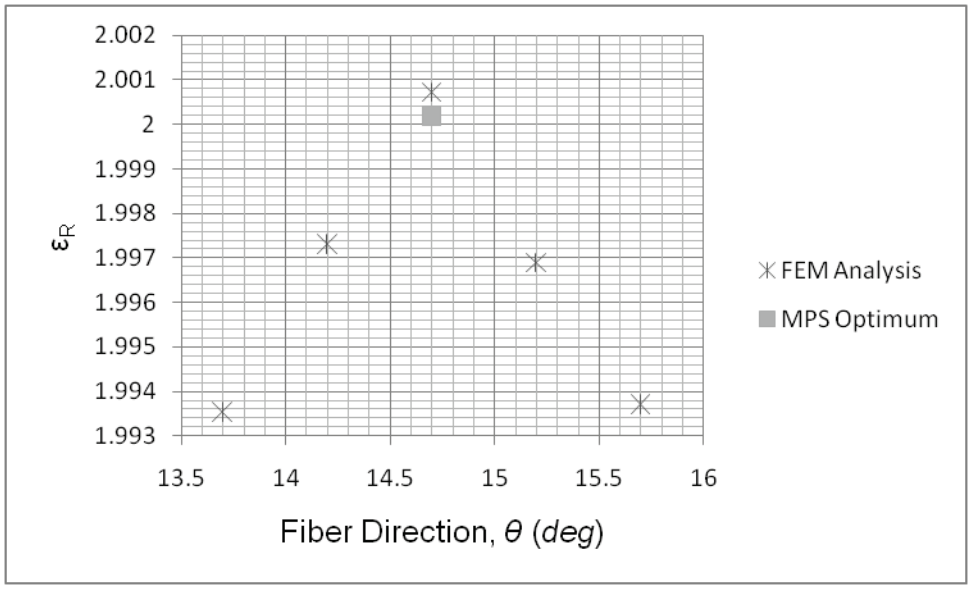

Fig. 56 Results of the FEM validation analysis performed in the neighbourhood of the optimal parameter θ_{opt} identified by using MPS and data model. *f=0.8* was used for this analysis.

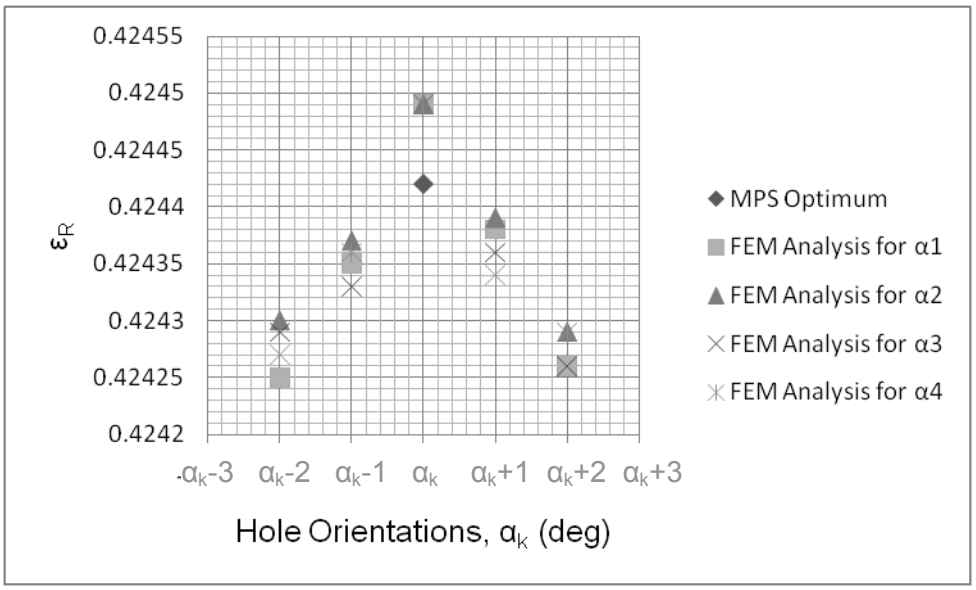

Fig. 57 Results of the FEM validation analysis performed in the neighbourhood of the optimal parameters $\alpha_{k,opt}$ identified by using MPS and data model. *f=0.95* was used for this analysis.

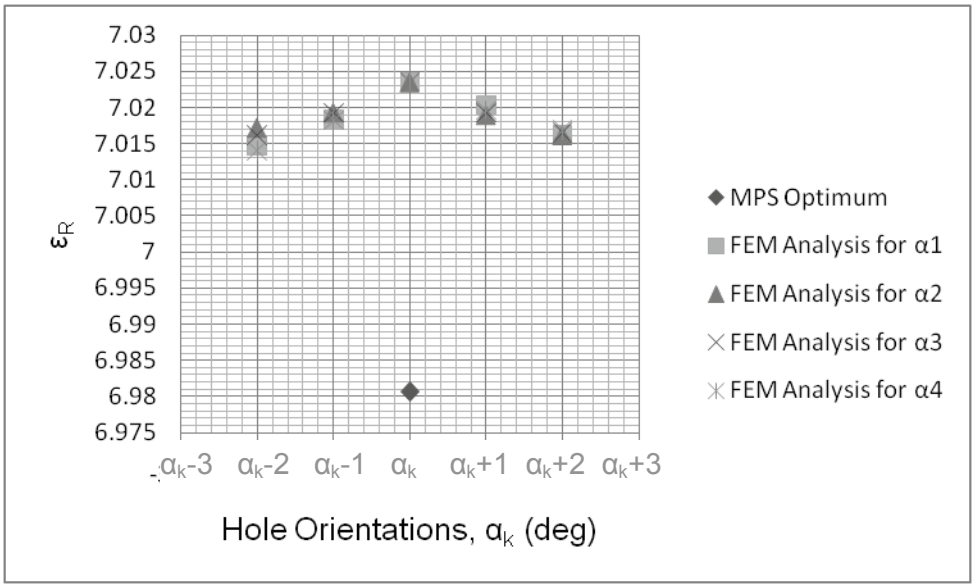

Fig. 58 Results of the FEM validation analysis performed in the neighbourhood of the optimal parameters $\alpha_{k,opt}$ identified by using MPS and data model. *f=0.65* was used for this analysis.

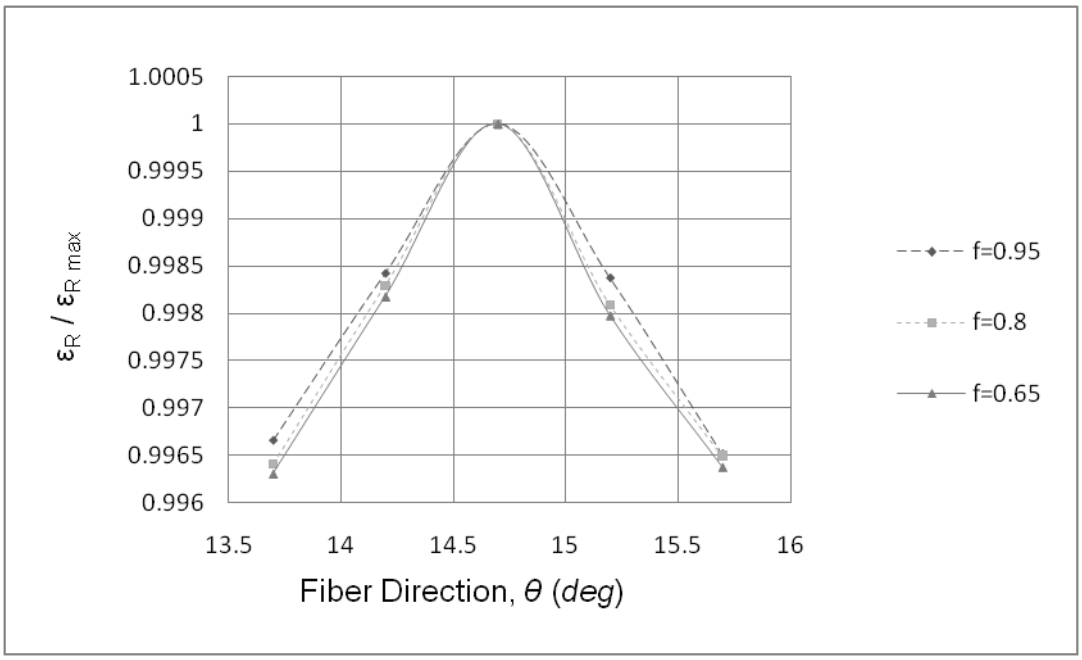

Fig. 59 FEM results in the neighbourhood of the optimal parameter θ_{opt} identified by using MPS and data model. *f=0.65, 0.8* and *0.95* were used for this analysis.

6- CONCLUSIONS

The two design concepts, in which respectively one and four holes in a composite shell (having a single lamina of unidirectional fibres) were axially loaded, were investigated in this work. As far as the first design concept concerns, it was found that the maximum radial strain was obtained when fibres were at *0*˚ with respects to the direction of the load, and the major axis of the hole was at *45.05*˚. For the second design concept, the maximum radial strain was obtained when the fibres were at 14.7˚ and when the major axes of the four holes were respectively at *1.5*˚, *57.2*˚, *1.5*˚, and *56.6*˚. It was assessed that these optimal values did not change for variation of the ellipse shape factor, *f*, in the range between *0.65* and *0.95*. The identified values of the considered parameters are optimal for different deformations applied to the shell, as long as it stays in elasticity region of the shell material, and for scaled geometrical designs of the hole(s). It was also observed that the single hole always yields the highest mechanical amplification. It should be noted that, the method proposed in this work has general applicability and could be implemented for identifying optimal geometrical parameters for cases in which multi-lamina composite structures and multiple holes are present. This work therefore represents a method to be used in future studies to analyze, for instance, if natural campaniform sensilla in array have optimal geometries to maximize radial strain

or to optimally design engineered arrays of strain sensors inspired by campaniform sensilla.

APPENDICES

APPENDIX A: ELASTIC BEHAVIOUR OF UNIDIRECTIONAL LAMINA

Here the mechanical behaviour of unidirectional lamina is reviewed [19]. Mechanical behaviour is presented by the elastic parameters and the mechanical constants or material properties. First, the relations between elastic parameters and mechanical constant are reviewed; then the transformation relations of these mechanical constants are studied. This review will be prepared to give better understanding of composite materials elastic behaviour to the reader.

Stress-Strain Relation

Anisotropic Material – In a general continuum media, the state of stress is defined by nine stress constants. Similarly, the state of strain is defined with nine strain constants. These stress and strain constants are the components on each side of an elemental cube and are represented respectively as, σ_{ij}, and ε_{ij}. *i* shows the perpendicular side of the cube to each axis and *j* show the direction of each component, shown in Fig. 59.

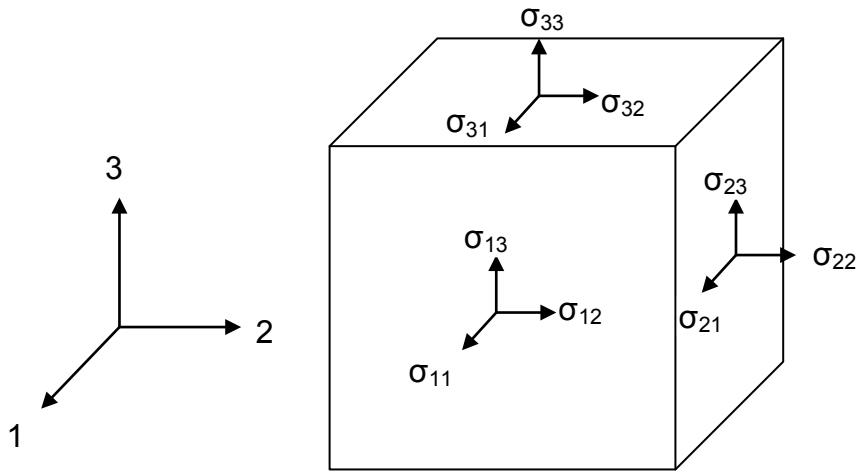

Fig. 60 State of stress on a cubic element of continuum

Hooke's law will be presented in matrix format for most general cases as below:

$$\begin{bmatrix}\sigma_{11}\\ \sigma_{22}\\ \sigma_{33}\\ \sigma_{23}\\ \sigma_{31}\\ \sigma_{12}\\ \sigma_{32}\\ \sigma_{13}\\ \sigma_{21}\end{bmatrix} = \begin{bmatrix} C_{1111} & C_{1122} & C_{1133} & C_{1123} & C_{1131} & C_{1112} & C_{1132} & C_{1113} & C_{1121}\\ C_{2211} & C_{2222} & C_{22233} & C_{2223} & C_{2231} & C_{2212} & C_{2232} & C_{2213} & C_{2221}\\ C_{3311} & C_{3322} & C_{3333} & C_{3323} & C_{3331} & C_{3312} & C_{3332} & C_{3313} & C_{3321}\\ C_{2311} & C_{2322} & C_{2333} & C_{2323} & C_{2331} & C_{2312} & C_{2332} & C_{2313} & C_{2321}\\ C_{3111} & C_{3122} & C_{3133} & C_{3223} & C_{3131} & C_{3112} & C_{3132} & C_{3113} & C_{3121}\\ C_{1211} & C_{1222} & C_{1233} & C_{1223} & C_{1231} & C_{1212} & C_{1232} & C_{1213} & C_{1221}\\ C_{3211} & C_{3222} & C_{3233} & C_{3223} & C_{3231} & C_{3212} & C_{3232} & C_{3213} & C_{3221}\\ C_{1311} & C_{3122} & C_{1333} & C_{1323} & C_{1331} & C_{1312} & C_{3132} & C_{1313} & C_{1321}\\ C_{2111} & C_{2122} & C_{2133} & C_{2123} & C_{2131} & C_{2112} & C_{2132} & C_{2113} & C_{2121}\end{bmatrix}\begin{bmatrix}\varepsilon_{11}\\ \varepsilon_{22}\\ \varepsilon_{33}\\ \varepsilon_{31}\\ \varepsilon_{21}\\ \varepsilon_{12}\\ \varepsilon_{32}\\ \varepsilon_{13}\\ \varepsilon_{21}\end{bmatrix}$$

(14)

And

$$\begin{bmatrix}\varepsilon_{11}\\ \varepsilon_{22}\\ \varepsilon_{33}\\ \varepsilon_{31}\\ \varepsilon_{21}\\ \varepsilon_{12}\\ \varepsilon_{32}\\ \varepsilon_{13}\\ \varepsilon_{21}\end{bmatrix} = \begin{bmatrix} S_{1111} & S_{1122} & S_{1133} & S_{1123} & S_{1131} & S_{1112} & S_{1132} & S_{1113} & S_{1121} \\ S_{2211} & S_{2222} & S_{2233} & S_{2223} & S_{2231} & S_{2212} & S_{2232} & S_{2213} & S_{2221} \\ S_{3311} & S_{3322} & S_{3333} & S_{3323} & S_{3331} & S_{3312} & S_{3332} & S_{3313} & S_{3321} \\ S_{2311} & S_{2322} & S_{2333} & S_{2323} & S_{2331} & S_{2312} & S_{2332} & S_{2313} & S_{2321} \\ S_{3111} & S_{3122} & S_{3133} & S_{3223} & S_{3131} & S_{3112} & S_{3132} & S_{3113} & S_{3121} \\ S_{1211} & S_{1222} & S_{1233} & S_{1223} & S_{1231} & S_{1212} & S_{1232} & S_{1213} & S_{1221} \\ S_{3211} & S_{3222} & S_{3233} & S_{3223} & S_{3231} & S_{3212} & S_{3232} & S_{3213} & S_{3221} \\ S_{1311} & S_{3122} & S_{1333} & S_{1323} & S_{1331} & S_{1312} & S_{3132} & S_{1313} & S_{1321} \\ S_{2111} & S_{2122} & S_{2133} & S_{2123} & S_{2131} & S_{2112} & S_{2132} & S_{2113} & S_{2121} \end{bmatrix} \begin{bmatrix}\sigma_{11}\\ \sigma_{22}\\ \sigma_{33}\\ \sigma_{23}\\ \sigma_{31}\\ \sigma_{12}\\ \sigma_{32}\\ \sigma_{13}\\ \sigma_{21}\end{bmatrix}$$

(15)

81 elastic constants are needed to describe the mechanical behaviour of a material. The two *9 by 9* matrices in (14) and (15) are respectively named stiffness and compliance matrix. By assuming the stress and strain tensor symmetry as,

$$\sigma_{ji} = \sigma_{ij} \tag{16}$$

$$\varepsilon_{ji} = \varepsilon_{ij} \tag{17}$$

The number of elastic constants reduces to 36; therefore, the stress and strain relation could be presented as,

$$\begin{bmatrix}\sigma_1\\ \sigma_2\\ \sigma_3\\ \tau_1\\ \tau_2\\ \tau_3\end{bmatrix} = \begin{bmatrix}C_{11} & C_{12} & C_{13} & C_{14} & C_{15} & C_{16}\\ C_{21} & C_{22} & C_{23} & C_{24} & C_{25} & C_{26}\\ C_{31} & C_{32} & C_{33} & C_{34} & C_{35} & C_{36}\\ C_{41} & C_{42} & C_{43} & C_{44} & C_{45} & C_{46}\\ C_{51} & C_{52} & C_{53} & C_{54} & C_{55} & C_{56}\\ C_{61} & C_{62} & C_{63} & C_{64} & C_{65} & C_{66}\end{bmatrix}\begin{bmatrix}\varepsilon_1\\ \varepsilon_2\\ \varepsilon_3\\ \gamma_1\\ \gamma_2\\ \gamma_3\end{bmatrix} \quad (18)$$

And

$$\begin{bmatrix}\varepsilon_1\\ \varepsilon_2\\ \varepsilon_3\\ \gamma_1\\ \gamma_2\\ \gamma_3\end{bmatrix} = \begin{bmatrix}S_{11} & S_{12} & S_{13} & S_{14} & S_{15} & S_{16}\\ S_{21} & S_{22} & S_{23} & S_{24} & S_{25} & S_{26}\\ S_{31} & S_{32} & S_{33} & S_{34} & S_{35} & S_{36}\\ S_{41} & S_{42} & S_{43} & S_{44} & S_{45} & S_{46}\\ S_{51} & S_{52} & S_{53} & S_{54} & S_{55} & S_{56}\\ S_{61} & S_{62} & S_{63} & S_{64} & S_{65} & S_{66}\end{bmatrix}\begin{bmatrix}\sigma_1\\ \sigma_2\\ \sigma_3\\ \tau_1\\ \tau_2\\ \tau_3\end{bmatrix} \quad (19)$$

By writing the work per unit volume relation as,

$$W = \frac{1}{2} C_{ij}\varepsilon_i\varepsilon_j \quad (20)$$

and differentiating twice we obtain,

$$C_{ij} = \frac{\partial^2 W}{\partial\varepsilon_i \partial\varepsilon_j} \quad (21)$$

It is obvious if we do the differentiation the other way around we have,

$$C_{ji} = \frac{\partial^2 W}{\partial \varepsilon_j \partial \varepsilon_i} \tag{22}$$

Which shows that equation (21) and (22) are identical and the differentiation order of (20) is immaterial, thus,

$$C_{ji} = C_{ij} \tag{23}$$

Then consequently,

$$S_{ji} = S_{ij} \tag{24}$$

Therefore, the stiffness and compliance matrix are expressed with 21 constants as,

$$\begin{bmatrix} C_{11} & C_{12} & C_{13} & C_{14} & C_{15} & C_{16} \\ C_{12} & C_{22} & C_{23} & C_{24} & C_{25} & C_{26} \\ C_{13} & C_{23} & C_{33} & C_{34} & C_{35} & C_{36} \\ C_{14} & C_{24} & C_{34} & C_{44} & C_{45} & C_{46} \\ C_{15} & C_{25} & C_{35} & C_{45} & C_{55} & C_{56} \\ C_{16} & C_{26} & C_{36} & C_{46} & C_{56} & C_{66} \end{bmatrix} \tag{25}$$

And

$$\begin{bmatrix} S_{11} & S_{12} & S_{13} & S_{14} & S_{15} & S_{16} \\ S_{12} & S_{22} & S_{23} & S_{24} & S_{25} & S_{26} \\ S_{13} & S_{23} & S_{33} & S_{34} & S_{35} & S_{36} \\ S_{14} & S_{24} & S_{34} & S_{44} & S_{45} & S_{46} \\ S_{15} & S_{25} & S_{35} & S_{45} & S_{55} & S_{56} \\ S_{16} & S_{26} & S_{36} & S_{46} & S_{56} & S_{66} \end{bmatrix} \tag{26}$$

Orthotropic Materials – An anisotropic material which has at least three mutually perpendicular planes of symmetry is orthotropic. The intersections of these planes define the three mutually perpendicular axes, which are so-called principal axes. In orthotropic materials the elastic constants are reduced to nine as,

$$\begin{bmatrix} \sigma_1 \\ \sigma_2 \\ \sigma_3 \\ \tau_1 \\ \tau_2 \\ \tau_3 \end{bmatrix} = \begin{bmatrix} C_{11} & C_{12} & C_{13} & 0 & 0 & 0 \\ C_{12} & C_{22} & C_{23} & 0 & 0 & 0 \\ C_{13} & C_{23} & C_{33} & 0 & 0 & 0 \\ 0 & 0 & 0 & C_{44} & 0 & 0 \\ 0 & 0 & 0 & 0 & C_{55} & 0 \\ 0 & 0 & 0 & 0 & 0 & C_{66} \end{bmatrix} \begin{bmatrix} \varepsilon_1 \\ \varepsilon_2 \\ \varepsilon_3 \\ \gamma_1 \\ \gamma_2 \\ \gamma_3 \end{bmatrix} \tag{27}$$

And,

$$\begin{bmatrix}\varepsilon_1\\ \varepsilon_2\\ \varepsilon_3\\ \gamma_1\\ \gamma_2\\ \gamma_3\end{bmatrix}=\begin{bmatrix}S_{11} & S_{12} & S_{13} & 0 & 0 & 0\\ S_{21} & S_{22} & S_{23} & 0 & 0 & 0\\ S_{31} & S_{32} & S_{33} & 0 & 0 & 0\\ 0 & 0 & 0 & S_{44} & 0 & 0\\ 0 & 0 & 0 & 0 & S_{55} & 0\\ 0 & 0 & 0 & 0 & 0 & S_{66}\end{bmatrix}\begin{bmatrix}\sigma_1\\ \sigma_2\\ \sigma_3\\ \tau_1\\ \tau_2\\ \tau_3\end{bmatrix} \tag{28}$$

Transversely Isotropic Materials – If in one of the principal planes of an orthotropic material the mechanical properties are the same, then it is transversely isotropic. That plane is called the plane of isotropy. By assuming 2-3 plane as the plane of isotropy, the constants with subscripts of 2 and 3 are interchangeable; thus,

$$C_{i2} = C_{i3} \tag{29}$$

$$S_{i2} = S_{i3} \tag{30}$$

In addition, the constants which are multiplied τ_2 and τ_3 in (27) and (28) are interchangeable as,

$$C_{55} = C_{66} \tag{31}$$

$$S_{55} = S_{66} \tag{32}$$

In Fig. 61 two elements in a plane of isotropy are illustrated. One of them is rotated by 45°. The plane of isotropy is under pure shear stress, τ_o.

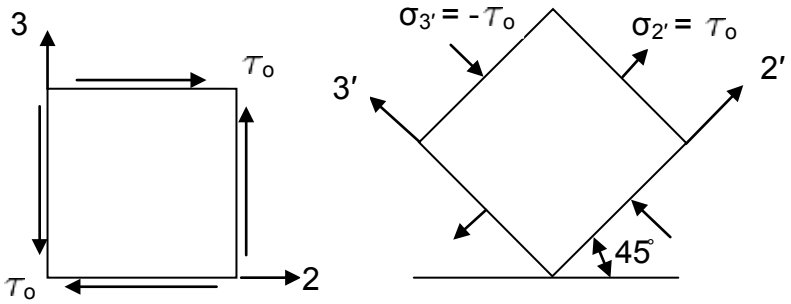

Fig. 61 Stress transformation on a plane of isotropy of a transversely isotropic material

Based on (27) and Fig. 61,

$$\tau_1 = C_{44}\gamma_1 = \tau_0 \tag{33}$$

The normal strain in the *45*°-angled plane would be,

$$\sigma_{2'} = \tau_0 = -\sigma_3 \tag{34}$$

$$\varepsilon_{2'} = -\varepsilon_{3'} = \frac{\gamma_4}{2} \text{ and } \varepsilon_1 = 0 \tag{35}$$

Then from the latest form of stiffness matrix (27),

$$\sigma_{2'} = C_{2'2'}\varepsilon_{2'} + C_{2'3'}\varepsilon_{3'} = C_{22}\varepsilon_{2'} - C_{23}\varepsilon_{2'} \tag{36}$$

Or

$$\sigma_{2'} = \varepsilon_{2'}(C_{22} - C_{23}) = \gamma_4 \frac{(C_{22} - C_{23})}{2} \tag{37}$$

Thus,

$$C_{44} = \frac{(C_{22} - C_{23})}{2} \tag{38}$$

We can see that the stiffness and compliance constant C_{44} and S_{44} are not independent anymore. Therefore, the stiffness and compliance matrix for transversely isotropic material will be reduced to 5 constants, such that,

$$\begin{bmatrix}\sigma_1\\ \sigma_2\\ \sigma_3\\ \tau_1\\ \tau_2\\ \tau_3\end{bmatrix} = \begin{bmatrix} C_{11} & C_{12} & C_{12} & 0 & 0 & 0 \\ C_{12} & C_{22} & C_{23} & 0 & 0 & 0 \\ C_{12} & C_{23} & C_{22} & 0 & 0 & 0 \\ 0 & 0 & 0 & \frac{C_{22}-C_{23}}{2} & 0 & 0 \\ 0 & 0 & 0 & 0 & C_{55} & 0 \\ 0 & 0 & 0 & 0 & 0 & C_{55} \end{bmatrix} \begin{bmatrix}\varepsilon_1\\ \varepsilon_2\\ \varepsilon_3\\ \gamma_1\\ \gamma_2\\ \gamma_3\end{bmatrix} \tag{39}$$

And,

$$\begin{bmatrix}\varepsilon_1\\ \varepsilon_2\\ \varepsilon_3\\ \gamma_1\\ \gamma_2\\ \gamma_3\end{bmatrix} = \begin{bmatrix} S_{11} & S_{12} & S_{12} & 0 & 0 & 0 \\ S_{21} & S_{22} & S_{23} & 0 & 0 & 0 \\ S_{21} & S_{32} & S_{22} & 0 & 0 & 0 \\ 0 & 0 & 0 & \frac{S_{22}-S_{23}}{2} & 0 & 0 \\ 0 & 0 & 0 & 0 & S_{55} & 0 \\ 0 & 0 & 0 & 0 & 0 & S_{55} \end{bmatrix} \begin{bmatrix}\sigma_1\\ \sigma_2\\ \sigma_3\\ \tau_1\\ \tau_2\\ \tau_3\end{bmatrix} \tag{40}$$

Orthotropic Material with Planar Stress – The majority of composite materials with structural application are made in thin layers which can tolerate the load in the plane of the layers. Thus, when an orthotropic material is under planar stress all the stress components in the out-of-plane direction are assigned a value of zero, then,

$$\begin{bmatrix}\sigma_1\\ \sigma_2\\ 0\\ 0\\ 0\\ \tau_3\end{bmatrix}=\begin{bmatrix}C_{11} & C_{12} & C_{12} & 0 & 0 & 0\\ C_{12} & C_{22} & C_{23} & 0 & 0 & 0\\ C_{12} & C_{23} & C_{22} & 0 & 0 & 0\\ 0 & 0 & 0 & C_{44} & 0 & 0\\ 0 & 0 & 0 & 0 & C_{55} & 0\\ 0 & 0 & 0 & 0 & 0 & C_{66}\end{bmatrix}\begin{bmatrix}\varepsilon_1\\ \varepsilon_2\\ \varepsilon_3\\ \gamma_1\\ \gamma_2\\ \gamma_3\end{bmatrix} \tag{41}$$

We observe that,

$$\gamma_2=\gamma_3=0 \tag{42}$$

$\varepsilon_3$is also eliminated by substituting its value, which results from the third row multiplication in (41). After all, the stiffness relation will be shortened to,

$$\begin{bmatrix}\sigma_1\\ \sigma_2\\ \tau_3\end{bmatrix}=\begin{bmatrix}Q_{11} & Q_{12} & 0\\ Q_{12} & Q_{22} & 0\\ 0 & 0 & Q_{33}\end{bmatrix}\begin{bmatrix}\varepsilon_1\\ \varepsilon_2\\ \gamma_3\end{bmatrix} \tag{43}$$

And the compliance relation to,

$$\begin{bmatrix}\varepsilon_1\\ \varepsilon_2\\ \gamma_3\end{bmatrix}=\begin{bmatrix}S_{11} & S_{12} & 0\\ S_{12} & S_{22} & 0\\ 0 & 0 & S_{33}\end{bmatrix}\begin{bmatrix}\sigma_1\\ \sigma_2\\ \tau_3\end{bmatrix} \tag{44}$$

Stress-Strain Relation with Material Constants

Anisotropic materials, anisotropic material with symmetric stress and strain tensors, anisotropic materials considering the elastic energy, orthotropic materials, transversely isotropic material and isotropic materials, in order, have 81, 36, 21, 9, 5 and 2 independent elastic constants.

Regarding to the elastic constants for an orthotropic material element under an uni-axial longitudinal tension, σ_1,

$$\varepsilon_1 = \frac{\sigma_1}{E_1} \tag{45}$$

$$\varepsilon_2 = -\frac{\nu_{12}}{E_1}\,\sigma_1 \tag{46}$$

$$\varepsilon_3 = -\frac{\nu_{13}}{E_1}\sigma_1 \tag{47}$$

$$\gamma_1 = \gamma_2 = \gamma_3 = 0 \tag{48}$$

If just uni-axial in-plane transverse tension, σ_2, is applied, then,

$$\varepsilon_1 = -\frac{\nu_{21}}{E_2}\,\sigma_2 \tag{49}$$

$$\varepsilon_2 = \frac{\sigma_2}{E_2} \tag{50}$$

$$\varepsilon_3 = -\frac{\nu_{23}}{E_2}\sigma_2 \tag{51}$$

$$\gamma_1 = \gamma_2 = \gamma_3 = 0 \tag{52}$$

Replacing the previously applied load with uni-axial out-of-plane transverse tension, σ_3, yields,

$$\varepsilon_1 = -\frac{\nu_{31}}{E_3}\,\sigma_3 \tag{53}$$

$$\varepsilon_2 = -\frac{\nu_{32}}{E_3}\sigma_3 \tag{54}$$

$$\varepsilon_3 = \frac{\sigma_3}{E_3} \tag{55}$$

Applying in-plane shear load,τ_3,

$$\varepsilon_1 = \varepsilon_1 = \varepsilon_3 = \gamma_1 = \gamma_2 = 0 \tag{56}$$

$$\gamma_3 = \frac{\tau_3}{G_{12}} \tag{57}$$

Again, applying out-of-plane shear load in 2-3 plane, τ_1, yields,

$$\varepsilon_1 = \varepsilon_1 = \varepsilon_3 = \gamma_2 = \gamma_3 = 0 \tag{58}$$

$$\gamma_1 = \frac{\tau_1}{G_{23}} \tag{59}$$

Finally, applying out-of-plane shear load in 1-3 plane, yields,

$$\varepsilon_1 = \varepsilon_1 = \varepsilon_3 = \gamma_1 = \gamma_3 = 0 \tag{60}$$

$$\gamma_2 = \frac{\tau_2}{G_{13}} \tag{61}$$

From (45-61) and (28), the stress-strain relation is stated as follow,

$$\begin{bmatrix} \varepsilon_1 \\ \varepsilon_2 \\ \varepsilon_3 \\ \gamma_1 \\ \gamma_2 \\ \gamma_3 \end{bmatrix} = \begin{bmatrix} \frac{\sigma_1}{E_1} & -\frac{\nu_{21}}{E_2} & -\frac{\nu_{31}}{E_3} & 0 & 0 & 0 \\ -\frac{\nu_{12}}{E_1} & \frac{\sigma_2}{E_2} & -\frac{\nu_{32}}{E_3} & 0 & 0 & 0 \\ -\frac{\nu_{13}}{E_1} & -\frac{\nu_{23}}{E_2} & \frac{\sigma_3}{E_3} & 0 & 0 & 0 \\ 0 & 0 & 0 & \frac{1}{G_{23}} & 0 & 0 \\ 0 & 0 & 0 & 0 & \frac{1}{G_{13}} & 0 \\ 0 & 0 & 0 & 0 & 0 & \frac{1}{G_{12}} \end{bmatrix} \begin{bmatrix} \sigma_1 \\ \sigma_2 \\ \sigma_3 \\ \tau_1 \\ \tau_2 \\ \tau_3 \end{bmatrix} \tag{62}$$

It is obvious that the compliance matrix in (62) is symmetric as,

$$\frac{\nu_{ij}}{E_i} = \frac{\nu_{ji}}{E_j} \tag{63}$$

APPENDIX B: A-FEM PROGRAMMING

Here the A-FEM template and MATLAB programming files for design concept 1 are presented. File “Main.m” is the body of the A-FEM. It includes the functions that ensure the entire A-FEM process is completed. First, the material properties are read in from “material.m”. The “AnsysInputCreat.m” is executed, afterward. Within “AnsysInputCreat.m” the template file is called and by adding the material properties and other variables value, an input file is created. After that, ANSYS is called and the input file is imported to ANSYS. It should be noted that ANSYS is run in batch mode. After ANSYS is done with solving the input file, it generates an output file. The output file`s data, such as the keypoints around the hole before and after imposing the strain, which is needed for mathematical post-processing, are scanned and saved. “EllipseRadiuses.m” calculates the hole radii at the keypoints for specific major radius, *r*, and ellipse shape factor, *f*. “FindMjrMnrAxis.m” computes ε_R with the data which was gathered and calculated, so far. Template file, “Main.m”, “material.m”, “AnsysInputCreat.m”, “EllipseRadiuses.m”, and “FindMjrMnrAxis.m” are presented, in order, as follows,

Template File

```
!!!!!Version It.1H.3.1Template!!!!
!***********This code units are all in mm scale***********!
!!!!!!!!!!!!!!!!!!Defining Variables!!!!!!!!!!!!!!!!!!!!!
*SET,a,2          !Shell Size
*SET,dx,a/1000                    !Applied Strain to the shell
*SET,thk,0.1              I Thickness of the shell
!!!!!!!!!!!!!!!!!!!**Initialization**!!!!!!!!!!!!!!!!!
/PREP7
!!!!!!!!!!!!!!!!!!!!!!!!!!!Element Type!!!!!!!!!!!!!!!!!!!!!!!!!!!
ET,1,SHELL63
!!!!!!!!!!!!!!!!!!!!!!!!!!!!!Modeling!!!!!!!!!!!!!!!!!!!!!!!!!!!!
BLC4,0,0,a,a          !Creating the Shell

!Creating The hole
CSYS,WP           !Tracking Coordinate System
LOCAL,11,1,a/2,a/2,0,alpha, , ,f,1,         !Defining a Local System
K,101:140,r,0:360:9                 !Defining Keypoints on a hole

!Connecting the keypoints to make the hoe circumferences
*DO,i,1,39,1
L,100+i,100+i+1
*ENDDO
L,100+40,100+1

!Dividing Shell by lines to Make hole's Areas
FLST,3,40,4,ORDE,2
FITEM,3,5
FITEM,3,-44
ASBL,      1,P51X
```

```
ADELE,2                          !Deleting the hole
CSYS,0                     !Back to the original coordinate
!!!!!!!!!!!!!!!!!!!!!!!!!!!!!!Meshing!!!!!!!!!!!!!!!!!!!!!!!!!!!!!!
!Mesh Size
FLST,5,40,4,ORDE,2
FITEM,5,5
FITEM,5,-44
CM,_Y,LINE
LSEL, , , ,P51X
CM,_Y1,LINE
CMSEL,,_Y
LESIZE,_Y1, , ,1, , , , ,1

FLST,5,4,4,ORDE,2
FITEM,5,1
FITEM,5,-4
CM,_Y,LINE
LSEL, , , ,P51X
CM,_Y1,LINE
CMSEL,,_Y
LESIZE,_Y1, , ,20, , , , ,1

!Meshing
MSHKEY,0
CM,_Y,AREA
ASEL, , , ,      3
CM,_Y1,AREA
CHKMSH,'AREA'
CMSEL,S,_Y
AMESH,_Y1
CMDELE,_Y
```

```
CMDELE,_Y1
CMDELE,_Y2

!!Keypoints coordinate are stored in kepoints number order!!
*DO,i,1,36,1
KSEL,s,kp,,100+i,,,0        !Select the first KP and so on
NSLK,S                !Select the Nodes on the Selected KPs
nlist,all,,,coord          !List Initial Coordinates of Nodes on the KPs
*ENDDO

!Save, Clear, Restore the cash
PARSAV,ALL, , ,
FINISH
/CLEAR,NOSTART
PARRES,NEW, , ,
!!!!!!!!!!!!!!!!!!!!!!!!!!!!!!!!!!!!!!!!!!!!!!!!!!!!!!!!!!!!!!!!!!!!!!!!!!
!!!!!!!!!!!!!!!!!!!!!!!!!!**Main**!!!!!!!!!!!!!!!!!!!!!!!!!!!!!!!!
/PREP7
!!!!!!!!!!!!!!!!!!!!!!!!!!!Element Type!!!!!!!!!!!!!!!!!!!!!!!!!!!!
ET,1,SOLID95
!!!!!!!!!!!!!!!!!!!!!!!!!!Material Properties!!!!!!!!!!!!!!!!!!!!!!!!!
MPTEMP,,,,,,,,
MPTEMP,1,0
MPDATA,EX,1,,E1
MPDATA,EY,1,,E2
MPDATA,EZ,1,,E3
MPDATA,PRXY,1,,PR12
MPDATA,PRYZ,1,,PR23
MPDATA,PRXZ,1,,PR13
MPDATA,GXY,1,,G12
MPDATA,GYZ,1,,G23
```

```
MPDATA,GXZ,1,,G13
!!!!!!!!!!!!!!!!!!!!!!Fibre Orientation!!!!!!!!!!!!!!!!!!!!!!
LOCAL,12,0,0,0,0,theta,0,0, , ,
!!!!!!!!!!!!!!!!!!!!!!Modeling!!!!!!!!!!!!!!!!!!!!!!
BLC4,0,0,a,a   !Creating the Shell

!Creating the hole
CSYS,WP    !Tracking Coordinate System
LOCAL,11,1,a/2,a/2,0,alpha, , ,f,1,    !Defining a Local System

!Defining Keypoints on the hole
K,101:140,r,0:360:9
*DO,i,1,39,1
L,100+i,100+i+1
*ENDDO
L,100+40,100+1

!Dividing Shell by lines to Make Hole Area
FLST,3,40,4,ORDE,2
FITEM,3,5
FITEM,3,-44
ASBL,      1,P51X

!Deleting the hole
ADELE,2

!Extrude the shell by thickness create volume
VOFFST,3,-thk, ,

CSYS,0            !back to the original coordinate
```

```
!!!!!!!!!!!!!!!!!!!!!!!!!!!!!Meshing!!!!!!!!!!!!!!!!!!!!!!!!!!!!!!
!Mesh Attributes
TYPE,   1
MAT,    1
REAL,
ESYS,    12
SECNUM,

!!!!!!!!!!!!!!!!!!!!!!!Defining the Mesh Size!!!!!!!!!!!!!!!!!!!!!!
!Number of mesh on each 36 line which created the hole circumferences
FLST,5,40,4,ORDE,2
FITEM,5,5
FITEM,5,-44
CM,_Y,LINE
LSEL, , , ,P51X
CM,_Y1,LINE
CMSEL,,_Y
LESIZE,_Y1, , ,1, , , , ,1

!Number of Mesh on each edge of the shell
FLST,5,8,4,ORDE,4
FITEM,5,1
FITEM,5,-4
FITEM,5,45
FITEM,5,-48
CM,_Y,LINE
LSEL, , , ,P51X
CM,_Y1,LINE
CMSEL,,_Y
LESIZE,_Y1, , ,40, , , , ,1
```

```
!Number of mesh along the thickness
FLST,5,4,4,ORDE,2
FITEM,5,89
FITEM,5,-92
CM,_Y,LINE
LSEL, , , ,P51X
CM,_Y1,LINE
CMSEL,,_Y
LESIZE,_Y1, , ,4, , , , ,1

!Meshing
CM,_Y,VOLU
VSEL, , , ,      1
CM,_Y1,VOLU
CHKMSH,'VOLU'
CMSEL,S,_Y
VSWEEP,_Y1
CMDELE,_Y
CMDELE,_Y1
CMDELE,_Y2

!!!!!!!!!!!!!!!!Defining Loads and Constants!!!!!!!!!!!!!!!!!!
! Constrain the left egde dx1=0
FLST,2,1,5,ORDE,1
FITEM,2,6
!*
/GO
DA,P51X,UX,

! Constrain the 3 Nodes in the Middle of left area dy=0
NSEL,S,LOC,X,
```

```
NSEL,R,LOC,Y,1
D,ALL, , , , , ,UY, , , , ,

!Constrain the Node in the Middle of left area dz=0
NSEL,R,LOC,Z,-(thk/2)
D,ALL, , , , , ,UZ, , , , ,

NSEL,ALL                !Select all the nodes

!Applying displacement
FLST,2,1,5,ORDE,1
FITEM,2,4
/GO
DA,P51X,UX,dx

!!!!!!!!!!!!!!!!!!Solve and list result!!!!!!!!!!!!!!!!!!!
!Solve
/SOL
/STATUS,SOLU
SOLVE

!Select Nodes to be presented in output file
*DO,j,1,40,1
KSEL,s,kp,,100+j,,,0        !Select a KP from first hole and the coresponding KPs on the other Holes
NSLK,S              !Select the Nodes on the Selected KPs

!List the selected nodes results
/POST1
PRNSOL,U,COMP           !List Displacement of Nodes
*ENDDO
```

!!!!!!!!!!!!!!!!!!Save, Clear, Restore the cash!!!!!!!!!!!!!!!!!!!!!

PARSAV,ALL, , ,

FINISH

/CLEAR,NOSTART

PARRES,NEW, , ,

main.m

```
function [x]=main()
e=material();
r=.1;
i=1;
for f=.65:.05:.95
   for alpha=0:10:170
      for theta=0:10:90
         AnsysInputCreat(alpha,theta,r,f,e);
         dos('"c:\Program Files\Ansys Inc\V110\ANSYS\bin\intel\ansys110" -b -i
ansysin.txt -o ansysout.out');
         numf=ReadFile2();
         nums=ReadFile();
         [rElps,DirctR]=EllipseRadiuses(r,f);
         x(i,1)=alpha;
         x(i,2)=theta;
         x(i,3)=f;
         x(i,4)=r;
         x(i,5)=FindMjrMnrAxis(rElps,DirctR,nums,numf);
         i=i+1;
      end
   end
end
save all
```

material.m

```
function[mat]=material()
mat=[138e3 11e3 11e3 .28 .4 .28 5.5e3 3.9e3 5.5e3];
%mat=[294000 12400;294000 1000;39000 12400;39000 1000];
```

AnsysInputCreat.m

```
function[]=AnsysInputCreat(alpha,theta,r,f,e)
%read the template ANSYS intput file
fid=fopen('Template3D.txt','r');
temp=fscanf(fid,'%c');
fclose(fid);
 %%
%creating ANSYS input file
fid=fopen('ansysin.txt','wt');
fprintf(fid,'*SET,alpha,%4.1f \n',alpha);
fprintf(fid,'*SET,theta,%4.1f \n',theta);
fprintf(fid,'*SET,f,%4.2f \n',f);
fprintf(fid,'*SET,r,%4.2f \n',r);
fprintf(fid,'*SET,E1,%8.1f \n',e(1,1));
fprintf(fid,'*SET,E2,%8.1f \n',e(1,2));
fprintf(fid,'*SET,E3,%8.1f \n',e(1,3));
fprintf(fid,'*SET,PR12,%4.2f \n',e(1,4));
fprintf(fid,'*SET,PR23,%4.2f \n',e(1,5));
fprintf(fid,'*SET,PR13,%4.2f \n',e(1,6));
fprintf(fid,'*SET,G12,%8.1f \n',e(1,7));
fprintf(fid,'*SET,G23,%8.1f \n',e(1,8));
fprintf(fid,'*SET,G13,%8.1f \n',e(1,9));
fprintf(fid,'%s',temp);
fclose(fid);
```

EllipseRadiuses.m

```
function[rElps,DirctR]=EllipseRadiuses2Arr(a,f)
format long
b=a*f;
n=90;                %Number of Breaks on Each Quarter of Hole
crcmf=pi*(a+b)*(1+[3*((a-b)/(a+b))^2]/[10+(4-3*((a-b)/(a+b))^2)^.5]);
%Circumference of Ellipise
brk=crcmf/(4*n);        %Each Break is 1/90 of a Quarter
theta(1,1)=(brk/a)*(180/pi);
theta(90,1)=(brk/b)*(180/pi);
m=(theta(90,1)-theta(1:1))/90;              %Slope of theta Function
for i=2:89
   theta(i,1)=m*i+theta(1:1);
end
if ne(sum(theta), 90)
   mEr=90/sum(theta);                %that Function Slope's Error
   theta(:,1)=mEr*theta(:,1);          %Correcting the Function
end
for i=1:11
   ksi(i,1)=sum(theta(1:9*(i-1),1));
end
for i=1:10
rQrtElps(i,1)=[(a^2*(1+(tand(ksi(i,1)))^2))/(1+(a*tand(ksi(i,1))/b)^2)]^.5;
end
  %%%%%%%%%%%%%%%%%%%%%%%%%%%%%%%%%%%%%%%%%%%%%%%%%%%%%%%%%%%%%%%%%%%%%%%
%rElps is the radius of the hole at each node(KP) regardless of having ellipse or circle at
initial shape
rElps(1:10,1)=rQrtElps(1:10,1);
rElps(11,1)=b;
rElps(12:20,1)=rQrtElps(10:-1:2,1);
rElps(21:40,1)=rElps(1:20,1);
```

```
%DirctR is the Direction of Radius of the hole at each node(KP) regardless of having
ellipse or circle at initial shape

DirctR(1:11,1)=ksi(1:11,1);

DirctR(12:20,1)=180-ksi(10:-1:2,1);

DirctR(21:40,1)=180+DirctR(1:20,1);
```

FindMjrMnrAxis.m

```
function[MaxRatioDifR,DirctMaxR]=FindMjrMnrAxis(rElps,DirctR,nums,numf)
format long
cntrx=sum(nums(1:40,2))/40+1;
cntry=sum(nums(1:40,3))/40+1;

dNodex(1:40,1)=nums(1:40,2);
dNodey(1:40,1)=nums(1:40,3);
nodex(1:40,1)=numf(1:40,2)+dNodex(1:40,1);
nodey(1:40,1)=numf(1:40,3)+dNodey(1:40,1);
%Deformed Radiuses
DfrmRx(1:40,1)=nodex(1:40,1)-cntrx;
DfrmRy(1:40,1)=nodey(1:40,1)-cntry;
DfrmR(1:40,1)=((DfrmRx(1:40,1)).^2+(DfrmRy(1:40,1)).^2).^.5;
%Differntial of Radiuses
DifR(1:40,1)=DfrmR(1:40,1)-rElps(1:40,1,1);
%Ratio of Radius Differental
RatioDifR(1:40,1)=DifR(1:40,1)./rElps(1:40,1,1)*100;
%Maximum and Minimum of Radius Differntial
    MaxDifR=max(DifR(1:40,1));
    MinDifR=min(DifR(1:40,1));
    indMaxDifR=find(DifR(1:40,1)==MaxDifR);
    indMinDifR=find(DifR(1:40,1)==MinDifR);
%Maximum and Minimum of Radius Differential Ratio
    MaxRatioDifR=max(RatioDifR(1:40,1));
    MinRatioDifR=min(RatioDifR(1:40,1));
    indMaxRatioDifR=find(RatioDifR(1:40,1)==MaxRatioDifR);
    indMinRatioDifR=find(RatioDifR(1:40,1)==MinRatioDifR);
%Direction of Maximum and Minimum of Radius Differential Ratio
    DirctMaxR=DirctR(indMaxDifR,1);
    DirctMinR=DirctR(indMinDifR,1);
```

APPENDIX C: ANN RESULTS (WEIGHTS AND BIASES)

The weight and bias factors which were generated for both design concepts with ANN are presented here.

Design Concept 1:

Table 6 – Hidden layer weight factor, W_h, hidden layer bias factor, B_h, and output layer weight factor, W_o, with 40 neurons for concept design 1.

Neuron #	W_h			B_h	W_o
	x_1	x_2	x_3		
1	-0.05843	0.255905	-1.65599	-2.39099	5.020994
2	1.492185	-0.07839	0.906483	-0.89623	-1.25378
3	-4.55751	2.978096	0.320489	4.72533	0.184965
4	-1.9948	-9.22643	12.11357	13.74041	0.000441
5	-4.10281	11.42898	-0.02373	11.3846	-6.16531
6	5.232732	-2.59268	3.176183	-3.58464	-0.00831
7	3.233019	-0.48902	0.237047	-0.31614	-2.65504
8	0.005011	0.217791	-1.85362	1.784922	-0.50557
9	2.89604	-0.41973	0.226895	-0.19893	4.382751
10	4.173389	-12.175	-0.01701	-11.8905	-11.7909
11	0.380232	-2.21082	2.670507	1.048996	0.028744
12	-1.72422	0.150307	-1.13266	0.951826	-0.81271
13	6.121166	-10.1646	-0.38614	-9.89097	-1.31165
14	1.857545	0.560533	-0.94881	-0.23778	-1.46883
15	1.692239	3.532686	-5.79839	-0.2195	0.002778
16	4.417822	-13.269	-0.06544	-12.7371	5.633577
17	-5.6518	-1.49042	0.065825	-0.26061	0.0972
18	3.82543	0.363711	-0.27651	0.491754	3.291966
19	1.078558	-5.40284	0.571896	-3.18165	-0.01127
20	-6.39299	10.67766	0.391676	10.30529	-1.23464
21	3.780485	0.297509	-0.3074	0.510766	-3.25165
22	0.829654	1.165539	0.618347	-0.17465	-0.14478
23	12.73502	-1.66907	0.035368	2.056587	-0.04669
24	1.612149	1.958374	0.516277	1.044532	-2.55493

25	*-3.49556*	*2.27504*	*0.244723*	*3.91659*	*-0.3341*
26	*1.798213*	*0.50936*	*-0.90829*	*-0.20186*	*1.698173*
27	*-0.21714*	*1.327227*	*-1.69739*	*1.390017*	*0.087609*
28	*-0.31855*	*1.356763*	*-1.73446*	*-1.72863*	*-0.14982*
29	*-1.64019*	*-1.91017*	*-0.49452*	*-1.0641*	*-2.61514*
30	*1.700319*	*3.485357*	*-0.5121*	*4.134858*	*-1.82229*
31	*2.571171*	*0.171032*	*-1.24467*	*2.569771*	*0.178724*
32	*-0.01945*	*0.145396*	*-1.01939*	*-0.80522*	*3.71114*
33	*-1.73417*	*-3.2479*	*0.558945*	*-4.06408*	*-1.95202*
34	*-2.4138*	*0.32599*	*-0.2215*	*-0.11523*	*1.586078*
35	*-6.0046*	*3.652128*	*0.167275*	*-4.40634*	*-0.00907*
36	*0.13783*	*-0.58369*	*1.305734*	*2.27835*	*2.768268*
37	*2.899113*	*3.958095*	*2.069008*	*7.346437*	*-0.15489*
38	*-5.31462*	*-6.27156*	*-7.74702*	*-7.29682*	*-0.00246*
39	*-0.69404*	*-1.5524*	*-0.45019*	*-2.65584*	*5.129868*
40	*1.136584*	*1.932158*	*0.59459*	*3.410239*	*3.946577*

Bias factor in the output layer is 7.152303.

.

Design Concept 2:

Table 7 - Hidden layer weight factor, W_h, hidden layer bias factor, B_h, and output layer weight factor, W_o, with 60 neurons for concept design 2.

Neuron #	W_h					B_h	W_o
	x_1	x_2	x_3	x_4	x_5		
1	0.25868	4.495225	-0.64378	-0.62711	-0.21292	6.329219	-0.21145
2	-0.08468	2.201918	-2.35634	-0.00224	-2.49727	-2.62517	0.02478
3	0.023813	-0.0369	0.017344	0.042343	-1.48939	3.029651	-3.33459
4	0.616042	0.930024	-4.49422	-0.65843	-0.07688	-5.11635	-0.08354
5	0.001292	0.76166	1.203391	-0.01864	0.18567	-1.66987	5.166334
6	-0.49121	0.035971	0.030249	0.036398	-0.08637	0.953662	-11.3972
7	-1.5869	1.700954	2.158155	-1.75474	0.182411	3.043703	0.037928
8	-2.22237	0.046562	0.027648	-0.82307	0.077919	-0.33662	0.069694
9	1.924976	7.901746	-1.9989	2.259687	-0.34715	7.886185	-0.02847
10	0.038841	-0.34341	-1.48205	-0.00251	0.060117	-0.32741	6.227852
11	0.014663	0.718776	1.267788	-0.03709	-0.048	-0.67067	1.762963
12	6.084089	3.710031	4.795214	-7.22535	-0.80558	-3.79579	0.00599
13	-0.02407	-0.04764	-0.02671	-0.01376	2.413009	2.863875	-4.83458
14	-2.07528	0.044721	-0.00738	2.006297	-2.06553	1.317743	0.022828
15	-0.65085	-1.005	-1.51625	0.579078	0.100894	0.836657	0.081624
16	0.805815	-0.02053	-0.01745	-0.04351	0.124045	-1.18154	-5.6461
17	-0.11005	1.761666	1.566696	-0.13119	-7.87382	-8.38008	-0.0482
18	1.725814	0.078945	0.086155	1.717233	-1.35814	-0.99972	0.054663
19	-1.33108	0.007177	-0.03998	-1.55216	-2.28056	1.397425	-0.04842
20	4.494586	-3.15444	-2.81519	-4.0213	0.884235	-0.77297	0.007365
21	-0.05804	2.710683	0.225389	0.131698	-0.90846	0.689581	-0.03607
22	-1.58191	-0.03474	-0.04748	1.629155	1.578306	0.38964	0.043831
23	0.740187	0.072793	0.068352	0.820864	0.828618	0.297983	0.941002
24	-0.03073	0.371177	1.322974	-0.00415	-0.04446	0.337119	10.98254
25	0.00133	0.716072	1.255112	-0.01979	0.246895	-1.65998	-3.70813
26	7.166222	-0.08887	0.055606	-7.15175	0.010958	-1.70722	0.013211
27	-0.29078	-1.30479	1.13444	0.281915	1.4056	-0.67726	0.588969
28	0.033471	-3.56723	3.097638	-0.33847	4.36576	-1.01299	0.00479
29	0.241691	-0.50542	-2.33341	2.041945	0.022907	0.442812	-0.01078
30	0.432762	0.06427	0.058401	0.46581	0.426164	0.359765	-3.97897
31	0.104523	0.037886	-0.05024	2.31111	-1.52895	0.708966	-0.03634
32	15.05369	3.904677	2.947722	-3.4623	-0.07114	7.518041	-0.00578
33	-0.87027	-0.0058	-0.02989	0.544087	0.675649	-0.04724	-0.23182
34	-0.16002	-0.49054	0.300125	0.13464	0.048015	-0.66357	1.485293
35	0.023255	1.021446	0.89334	-0.0077	0.959897	-0.04678	-1.51829

36	*1.094249*	*-1.56434*	*-1.31551*	*-0.92894*	*0.467867*	*-0.34025*	*-0.03503*
37	*0.516928*	*-0.08935*	*-0.05412*	*1.303099*	*0.042424*	*-0.53292*	*0.253479*
38	*-0.0635*	*-0.2833*	*0.596633*	*0.058048*	*-0.00098*	*0.527548*	*3.005083*
39	*-0.23107*	*-3.7372*	*3.437177*	*-0.21652*	*-3.38149*	*-1.20105*	*-0.01119*
40	*8.303865*	*-8.76401*	*1.401408*	*19.28737*	*-0.13756*	*-3.41103*	*-0.004*
41	*-2.17281*	*-2.34548*	*-2.42662*	*-2.16865*	*-4.70782*	*-2.42421*	*-0.01502*
42	*1.651489*	*13.96555*	*-3.28792*	*2.4588*	*-0.31082*	*11.80893*	*0.020713*
43	*-0.52089*	*-1.57015*	*-1.13979*	*0.738487*	*0.437418*	*-0.24216*	*-0.03658*
44	*0.009194*	*-0.1596*	*-0.58171*	*0.00759*	*0.010669*	*-0.44387*	*20.57195*
45	*-0.32199*	*-0.27955*	*-0.28329*	*-0.33549*	*-0.99954*	*0.31917*	*-0.3971*
46	*-2.01578*	*1.916749*	*1.817976*	*-1.74075*	*-0.00119*	*-1.01578*	*0.033769*
47	*-0.00231*	*-0.02159*	*-0.0114*	*0.003317*	*2.201886*	*3.264305*	*12.17395*
48	*-1.59038*	*-1.91014*	*-2.0292*	*-1.60243*	*0.949039*	*-1.95384*	*-0.03942*
49	*-3.762*	*-1.06518*	*0.578686*	*2.12254*	*0.063683*	*-2.81704*	*3.189246*
50	*0.562974*	*0.113999*	*0.117376*	*0.599896*	*1.120242*	*1.142566*	*0.76211*
51	*-3.68152*	*-1.10204*	*0.593249*	*2.009381*	*0.067812*	*-2.76128*	*-1.59864*
52	*-0.78866*	*1.298281*	*-0.78837*	*1.17495*	*-2.82676*	*-2.9256*	*-0.01151*
53	*-2.38656*	*0.065027*	*0.002145*	*0.106987*	*1.814299*	*-0.64499*	*0.031091*
54	*-0.01597*	*0.489755*	*0.930005*	*-0.01805*	*-0.02452*	*1.315395*	*7.806976*
55	*-3.85822*	*-1.032*	*0.566082*	*2.247889*	*0.058777*	*-2.88534*	*-1.60001*
56	*-0.25553*	*-1.25659*	*1.096571*	*0.243349*	*1.341762*	*-0.65392*	*-0.69281*
57	*-1.11534*	*-0.01652*	*-0.02877*	*0.300196*	*-0.02279*	*0.025595*	*0.436375*
58	*1.586614*	*1.794661*	*1.790304*	*1.556826*	*-1.97969*	*-1.54892*	*0.029885*
59	*-0.01825*	*-1.04909*	*-0.90837*	*0.012701*	*-0.88029*	*0.027265*	*-1.6581*
60	*-0.55531*	*0.014162*	*0.034709*	*-1.05047*	*0.047418*	*-1.14205*	*-0.62334*

Bias factor in the output layer is 3.701879.

References

[1] Werner Gnatzy, Ulrike Grünert, and Manfred Bender, 1987, "Campaniform Sensilla of Calliphora Vicina (Insecta, Diptera)," 106(5) pp. 312.

[2] Page, A. P. and Johnstone, I. J., 2007, "The Cuticle,"The C. elegans Research Community, .

[3] Vincent, J. F. V., and Wegst, U. G. K., 2004, "Design and Mechanical Properties of Insect Cuticle," Arthropod Structure & Development, 33(3) pp. 187-199.

[4] Skordos, A., Chan, P. H., Vincent, J. F. V., 2002, "A Novel Strain Sensor Based on the Campaniform Sensillum of Insects," Philosophical Transactions: Mathematical, Physical and Engineering Sciences, 360(1791, Biomimetics: Technology Transfer from Biology to Engineering) pp. 239-253.

[5] D. H. B. Wicaksono, J. F. V. Vincent, G. Pandraud, 2005, "Biomimetic Strain-Sensing Microstructure for Improved Strain Sensor: Fabrication Results Andoptical Characterization," J. Micromech. Microeng., 15(1) pp. 72.

[6] Ulrike Grünert, W. G., 1987, "Campaniform Sensilla of Calliphora Vicina (Insecta, Diptera)II," 106(5) pp. 320.

[7] Menon, C., Carpi, F., and De Rossi, D., 2009, "Concept Design of Novel Bio-Inspired Distributed Actuators for Space Applications," Acta Astronautica, 65(5-6) pp. 825-833.

[8] Menon, C., Brodie, R., Clift, S., 2009, "Concept Design of Strain Sensors Inspired by Campaniform Sensilla," Acta Astronautica, 64(2-3) pp. 176-182.

[9] Vincent, J. F. V., Clift, S. E., and Menon, C., 2007, "Biomimetics of Campaniform Sensilla: Measuring Strain from the Deformation of Holes," Journal of Bionic Engineering, 4(2) pp. 63-76.

[10] Mahmoudabadi, H., Izadi, M., and Menhaj, M. B., 2009, "A Hybrid Method for Grade Estimation using Genetic Algorithm and Neural Networks," 13(1) pp. 91-101.

[11] Abouhamze, M., and Shakeri, M., 2007, "Multi-Objective Stacking Sequence Optimization of Laminated Cylindrical Panels using a Genetic Algorithm and Neural Networks," Composite Structures, 81(2) pp. 253-263.

[12] Ruijter, W., Spallino, R., Warnet, L., 2003, "Computational Fluid and Solid Mechanics 2003,"Elsevier Science Ltd, Oxford, pp. 2359-2363.

[13] Hornik, K., Stinchcombe, M., and White, H., 1990, "Universal Approximation of an Unknown Mapping and its Derivatives using Multilayer Feedforward Networks," Neural Networks, 3(5) pp. 551-560.

[14] Hornik, K., Stinchcombe, M., and White, H., 1989, "Multilayer Feedforward Networks are Universal Approximators," Neural Networks, 2(5) pp. 359-366.

[15] Soden, P. D., Hinton, M. J., and Kaddour, A. S., 1998, "Lamina Properties, Lay-Up Configurations and Loading Conditions for a Range of Fibre-Reinforced Composite Laminates," Composites Science and Technology, 58(7) pp. 1011-1022.

[16] Hagan, M.T., Menhaj, M., 1994, "Training Feedforward Networks with the Marquardt Algorithm." 5(6) pp. 989-993.

[17] Duan, X., Wang, G. G., Kang, X., 2010, "Performance Study of Mode-Pursuing Sampling Method," 41(1) pp. 1.

[18] Wang, L., Shan, S., and Wang, G. G., 2004, "Mode-Pursuing Sampling Method for Global Optimization on Expensive Black-Box Functions," 36(4) pp. 419.

[19] I. M. Daniel, O. Ishai, 1994, "Engineering Mechanics of Composite Materials,"Oxford University Press, New York, pp. 37-84, Chap. 3.